Ferdowsi University of Mashhad

Journal of Agricultural Machinery

Iranian Society of Mechanical Engineers (ISME)

Vol. 13 No. 1

2023

ISSN: 2228-6829

Contents

Journal of Agricultural Machinery

Vol. 13 **No. 1** **2023**

Published by: Ferdowsi University of Mashhad, (College of Agriculture), Iran

Publisher: Ferdowsi University of Mashhad

Address: College of Agriculture, Ferdowsi University of Mashhad, Iran

P.O. BOX: 91775-1163

Fax: +98-05138787430

E-Mail: jame@um.ac.ir

Web Site: http://jame.um.ac.ir

Contents

Research Articles

Journal of Agricultural Machinery

Homepage: https://jame.um.ac.ir

Research Article
Vol. 13, No. 1, 2023, p. 1-13

Mathematical Analysis for Prediction Performance Rate of Wheel Type Trenching Machine

M. I. Ghonimy[1, 2*], M. A. Morcos[1], A. E. Badr[1]

1- Agricultural Engineering Department, Faculty of Agriculture, Cairo University, Giza, Egypt
2- Department of Plant Production and Protection, College of Agriculture and Veterinary Medicine, Qassim University, Buraydah, Saudi Arabia
(*- Corresponding Author Email: mohamed.ghonimy@agr.cu.edu.eg)
https://doi.org/10.22067/jam.2021.71081.1049

Received: 31 March 2021
Revised: 03 July 2021
Accepted: 28 July 2021
Available Online: 28 July 2021

How to cite this article:
Ghonimy, M. I., Morcos, M. A., & Badr, A. E. (2023). Mathematical Analysis for Prediction Performance Rate of Wheel Type Trenching Machine. *Journal of Agricultural Machinery*, *13*(1): 1-13. https://doi.org/10.22067/jam.2021.71081.1049

Abstract

In this study a mathematical analysis for estimating the performance rate "*RP*" of wheel type trenching machine was studied. The mathematical analysis quantifies the analysis and resulted in an equation. This mathematical equation was checked under different operating conditions. The practical study of the performance rate showed that the deviation of the theoretical performance rate from the actual performance rate ranged from 5 to 7% for the 60.4 and 90.5 cm trench depth, respectively. The machine field efficiency also ranged between 43 and 50.1% for 90.5 cm and 60.4 cm trench depth respectively.

Keywords: Modeling, Tile drainage, Trencher performance

Introduction

Drainage in agriculture means removing free water from soil which is in excess to the soil field capacity in the region of the root zone of the plants, in order to reach the best soil moisture-air balance that suits the growing crop. The functions of trenching machines are to mechanically perform the digging off the trenches, placing the tiles at the bottom of the trenches and back filling the soil in the trenches. There are mainly three types of trenching machines different in their construction and performance. These three types are chain type trenching machines, wheel type trenching machine and plow type trenching machines. Day (1973) defined the productivity of trenching machines as the rate the excavator can move along the trench line. He mentioned that the rate of excavation for a continuous trenching machine is its controlled productivity. It will vary with the width and depth of trench, the toughness of the material to be excavated and the power available or selected by the operator. Peurifoy (1970) studied the productivity in trenching operations. He found many factors affecting the production rate of trenching machine. These include the class of soil, depth and width of trench, extent of shoring required, topography, climatic condition, extent of vegetation such a trees, stumps and roots, and physical obstruction, such as buried pipes, sidewalks, paved streets, building etc.

In case of laying a pipeline, the speed with which the pipe can be placed in the trench, also affect the production rate of the machine. Sitorus, Ko, & Kwon (2016) reported that the digging machine forward speed, cutting depth, uniaxial compressive strength, and trench width are the most sensitive parameters affecting the power and angular speed. Design optimization using the information drawn from this parameter study can be preceded by focusing on the selection of traverse speed,

uniaxial compressive strength, trench width, carrier weight, nose radius, bar length, and pivot point location. Ghonimy (2021) reported that the theoretical performance rate of the chain-type trenching machine was lower than the actual performance rate by 3.4% and 2% at the trench depth 120.7 cm and 150.7 cm, respectively. Spencer, Machin, & Jackson (2007) described the principle features of the upgraded trencher and methods of calculating predicted trenching performance and they found that the target performance rate for wheel type trenching machine ranged from 80 to 400 m h^{-1} according to soil type. Schwap, Frevert, Edminster, & Barnes (1966) studied the productivity in trenching operations. They found many factors affecting it such as; soil moisture, soil characteristics as hardness and stickiness, stones, and submerged stumps, depth of trench, conditions of the trenching machine, the ski1l of the operator, and the delays due to interruptions during operation. They found that an extremely wet soil may stop machine operation. Soil with a low moisture content may not affect the digging rate to any extent, but soil that stick to the buckets of the machine, sandy soils that fall apart easily, and deep cuts reduce digging speed. They also found that increasing the depth from 90 to 150 cm decreased the digging speed by 56 percent under Iowa and Minnesota conditions. Ghonimy *et al.* (2022) concluded that the theoretical excavation force calculated by the mathematical model was lower than the actual excavating force by 4.0 kN and 3.5 kN for the 1.2 m and 1.5 m trench depths, respectively, for a chain type trenching equipment, and at trench depths of 1.2 m and 1.5 m, respectively, the theoretical excavation power was lower than the actual excavating power by 3.8% and 2.8%. Du, Dorneich, & Steward (2016) found that the human operator control inputs to execute a work cycle of an excavator trenching operation. The simulation results in a work cycle that is generated by executing a series of tasks in the way a human operator would perceiving the state of the machine, deciding when to transition from one task to the next, and controlling the machine to move the bucket through the tasks. The virtual operator model appropriately adapted to different operator control strategies, machine parameters changes (i.e. pump speed) and a change in work site goals (trench depth, pile location). The model-generated outputs based on human-like perception, decision-making, and action selection. Atangana Njock, Zheng, Zhang, & Xu (2020) found that the success of jet trenching operations is closely related to some key factors including the soil conditions, trencher specifications, and characteristics of pipelines or cables. Three case histories are presented to demonstrate the importance of these key factors and their interrelationships. They also found that the performance of the jet trenchers on product burial is greatly dependent on the operation depth, soil conditions, the machine, and products specificities. When operating at a very large depth, most available models can achieve a maximum burial of 3 m within soils ranging from sand to stiff clays. The success of jet trenching operations also depends on the ability to accurately characterize the seabed sediments. Reddy & Shailesh (2018) mentioned that, in order to increase the life of backhoe excavator bucket tooth other two materials i.e. HSS and HCHCr has been analyzed for the similar force and boundary conditions. A 3D model was prepared in solid works and software in FEM domain was utilized for analyzing the model or excavator bucket tooth behavior. Computational approach will give the results more close to practical values through simulation. Computer-Aided Engineering (CAE) can drastically reduce the costs associated with the product lifecycle.

Whatever the type of the trenching machine is, it has the advantage of quite high rate of performance, since it simultaneously digs the trench, lays down the tiles or the pipes and, in some types, it also refills the ditches with the soil. This means fulfilling its complete function in a short period within the same day. It is characterized with the high accuracy in laying the pipes or the tiles at the required depth and slope. Besides, these types of

trenching machines suppress the manual way of digging and laying drainage pipes by its lower costs of operation.

The purpose of this work was to find out the main factors affecting wheel type trenching machine performance rate, and to relate these affecting factors in mathematical relationships. These mathematical relationships were used to predict the performance rate of wheel type trenching machine.

Materials and Methods

Mathematical analysis approach

The wheel type trenching machine (Fig. 1) has its specific effective mechanism which performs its required functions, the mathematical analysis had to be preceded with the two main steps which were; to state the theory, the construction the specifications and the dimensions of the applied mechanism for wheel type trenching machine and to state the expected affecting factors on the performance of the applied mechanism, the nature and the magnitude of their effects. The performance rate of the trenching machine depends, by a great extent, to the forward speed of the machine. This forward speed in return, is related to both the size of the power source of the trenching machine and the magnitude of the consumed power during the performance of the machine. Therefore, the mathematical analysis depended on expressing the magnitude of any required power of the trenching machine as a function of machine forward speed. By equating the size of the power source with the summation of the required powers during machine performance (equation 1), the magnetite of the maximum machine forward speed can be estimated, and hence, the rate of performance of the machine can be determined.

$$P_b = P_c + P_r + P_i + P_s + P_t + P_e \pm P_a + P_n \quad (1)$$

Where:

P_b = brake power of the engine of the machine, kW;

P_c = pulling power needed for cutting, kW;

P_r = pulling power to overcome rolling resistance, kW;

P_i = pulling power to overcome slope resistance, kW;

P_s = power lost in slop resistance, kW;

P_t = power 1ost in transmission systems, kW;

P_e = power required to lift the cut soil, kW;

P_a = power required to overcome air resistance, kW;

P_n = power required to accelerate the machine to the operating speed due to its inertia, kW.

Both P_a and P_n could be neglected since the operating forward speeds of the trenching machine are very limited compared with any other moving truck. Therefore, equation (2) can be simplified as shown in the following equation (2).

$$P_b = P_c + P_r + P_i + P_s + P_t + P_e \quad (2)$$

The theory, construction, and specifications of the mechanisms of wheel type trenching machine

The excavating unit of wheel type trenching machine (Fig. 2), consists of a rotating wheel equipped with buckets on its periphery. The cutting edge of the bucket may be equipped with some teeth. The radius (r) of the buckets cutting edges is circular pathway from the wheel center to bucket cutting edges. The wheel rotates at (n) rps and d is the depth of the digged trench. The performance theory of wheel type trenching machine is that, while the machine moves horizontally at a speed (V_m), the wheel rotating speed (n) rps, and the cutting edges of the buckets move in curved paths almost following the ellipse equation (3). The cutting edges cut the soil in thin curved layers, and elevate it upwards. The direction and the speed of bucket cutting edge can be mathematically determined, with enough accuracy, using the ellipse equation.

To prove that, the pathway of the cutting edge of the bucket follows a curve close to that generated from the ellipse equation, Fig. 3 shows the consecutive locations (X_i) and (Y_i) of bucket cutting edge. When bucket cutting edge just passes the vertical line through wheel center of rotation:

$X_o = 0$ $Y_0 = r$

At the consecutive different locations:

$X_1 = r \sin \mu + V_m . t$ $\quad Y_1 = r \cos \mu$

$X_2 = r \sin 2\mu + V_m .2t$ $\quad Y_2 = r \cos 2\mu$

$X_i = r \sin i\mu + V_m . it$ $\quad Y_i = r \cos i\mu$

When bucket cutting edge just passes the horizontal line through wheel center of rotation:

$$X_{n^*} = r + V_m \times n^* t \quad , \qquad Y_{n^*} = 0$$

Where n is wheel rotating speed , rps, t. rev is the Time of one revolution, s^{-1} = 1/n, n^* is the number of divisions within an angle = $\pi/2 = 90^o$, μ is the central angle of each division = $\pi/2n^*$, t= Time needed for rotating an angle equal μ, $t = \frac{1}{n} \times \frac{\mu}{2\pi} = \frac{1}{n} \times \frac{\pi}{2n^* \times 2\pi} = \frac{1}{4n \times n^*}$ sec, and $n^* t = \frac{1}{4n}$ sec

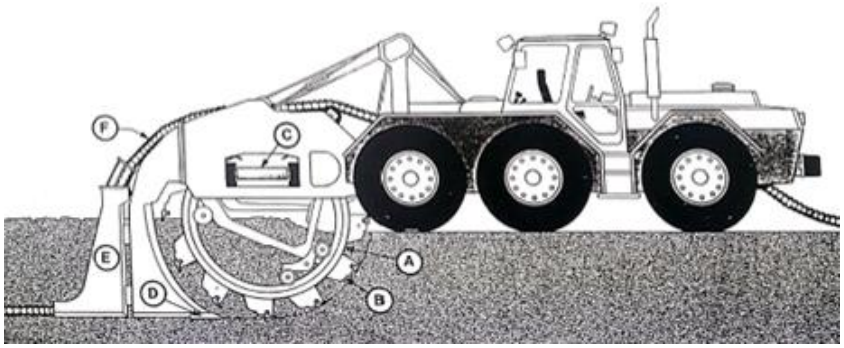

A) Rotating wheel
B) Digging buckets attached to wheel
C) Cross conveyor for excavated earth
D) Shoe to smooth trench bottom
E) Tubing (tile) shute
F) Corrugated drainage tubing

Fig. 1. Wheel type trenching machine

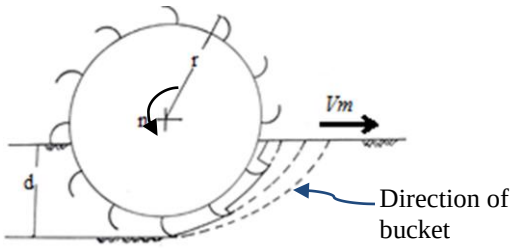

Fig. 2. The mechanism of wheel type trenching machine.

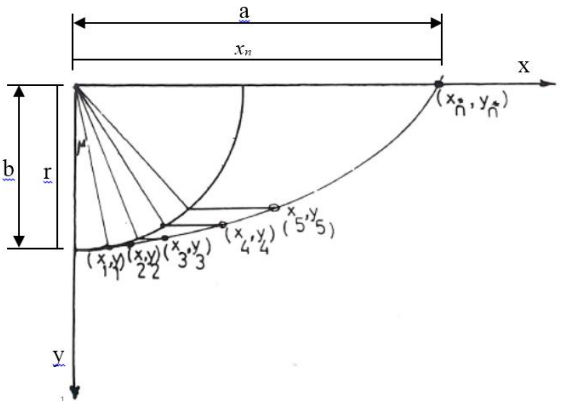

Fig. 3. The pathway of the bucket cutting edge for wheel type trenching machine.

If the ellipse equation applies to this case, equation (3), the values of (a) and (b) can be determined by substituting for

$$\frac{X^2}{a^2} + \frac{Y^2}{b^2} = 1 \qquad (3)$$

X and Y for two cases, one when X = 0 and the other time when Y = 0

When $X = 0$ $\quad b = r$ (4)

When $Y = 0$ $\quad a = r + V_m . n^* t = r + V_m / 4n$ (5)

and the general equation will be:

$$\frac{(r.\sin i\mu + V_m.it)^2}{(r + V_m.n^*.t)^2} + \frac{(r.\cos i\mu)^2}{r^2} = 1 \qquad (6)$$

To check this equation, the left side must be equal to 1 if the elliptic equation applies.

The left side of equation (6) can be written as:

$$\frac{r^2 sin^2 i\mu + V^2{}_m . i^2 . t^2 + 2r\, V_m\, .\, i . t . \sin i\mu}{r^2 + V^2{}_m . n^{*2} . t^2 + 2r . V_m . n^* . t} + cos^2 i\mu$$

$$= \frac{r^2 . sin^2 i\mu + {V_m}^2 . i^2 . t^2 + 2r . V_m . i . t . \sin i\mu + r^2 cos^2 i\mu + V^2{}_m . n^{*2} . t^2 . cos^2 i\mu + 2r . V_m . n^* . t . cos^2 i\mu}{r^2 + V^2{}_m . n^{*2} . t^2 + 2r . V_m . n^* . t}$$

$$= \frac{r^2 (sin^2 i\mu + cos^2 i\mu) + V^2{}_m . n^{*2} . t^2 . \left[\left(\frac{i}{n^*}\right)^2 + cos^2 i\mu\right] + 2rV_m . n^* . t . \left(\frac{i}{n^*} \sin i\mu + cos^2 i\mu\right)}{r^2 + V^2{}_m . n^{*2} . t^2 + 2r . V_m . n^* . t} \quad (7)$$

$$= \frac{r^2 + V^2{}_m . n^{*2} . t^2 . \left[\left(\frac{i}{n^*}\right)^2 + cos^2 i\mu\right] + 2r . V_m . n^* . t . \left(\frac{i}{n^*} . \sin i\mu + cos^2 i\mu\right)}{r^2 + V^2{}_m . n^{*2} . t^2 + 2r . V_m . n^* . t}$$

The values of the left side of equation (6) equal 1 when i=0 and the angle ($i\mu$) = 0 or when $i = n^*$ and $i\mu = \pi/2$, but it deviates in between. The deviation is very small and can be ignored since both the value of ($V^2{}_m . n^{*2} . t^2$) and ($2r . V_m . n^* . t$) are very small compared with the value of (r^2). When reasonable values of the parameters in the left side of equation (6) was considered. The deviation was computed for different values of ($i\mu$) as shown in Table 1.

Table 1- The deviation of the actual pathway of bucket cutting edge from the curve of the equation of ellipse

iμ	0	π/12	π/6	π/4	π/3	π/2.4	π/2
Deviation, %	0	-0.37	-1.2	-2.3	-1.93	-1.69	0

Thus, the computed deviations were less than -2.3 Percent.

Factors affecting the performance of the trenching machine

There are many factors affecting the performance rate of the trenching machine. These factors can be classified into two groups. Soil factors which include; soil specific weight (ω), N.cm^{-3}, soil unit draft (U), N.cm^{-2}, traction coefficient, rolling resistance coefficient (RR), angle between inclined soil surface and the horizontal direction (ψ), and friction coefficients between soil and soil and between soil and metal (F_{ms}). Machine factors which include; machine weight (W_m), N, machine brake power (P_b), kW, machine forward speed (V_m), m s^{-1}, trench cutting width (W_t), cm, vertical depth of the cut trench (d), cm, slip percentage of the tractor device of the machine (S), machine transmission efficiency (η_t), machine field efficiency (η_f), wheel radius (r), m, wheel rotating speed (n), rps, and the number of buckets on the wheel (N_B).

Some assumptions and simplifications were done in order to facilitate mathematical manipulation. These include Homogeneous and isotropic soil, with a constant unit draft. Constant velocities for any moving element, i.e., constant machine forward speed, and constant rotating for the rotating wheel were assumed. The path of the cutting edge was considered elliptical in shape.

Mathematical analysis steps

The mathematical analysis for estimating the performance rate (RP) of the wheel type trenching machine is expected to be in the form of the equation (8):

$$RP = 60 \times Vm \times \eta_t \quad (8)$$

Where:

RP = the actual performance rate of the machine, m min^{-1};

V_m = the machine forward speed, m s^{-1};

η_f = the field efficiency.

To find out the value of V_m, the components of equation (2*) were obtained as the following:

$$P_c + P_r + P_i + P_s + P_t + P_e - P_b = 0 \qquad (2^*)$$

Determination of P_c

Referring to Fig. 4, the pulling power needed for cutting depends on the cutting force (F_c) and the absolute speed of the bucket cutting edge (V_{bi})

$$P_c = 0.001 \left(\sum_{i=1}^{N} F_{ci}.V_{bi} \right)$$

$$P_c = 0.001\, K^*.U.W_t.\sum_{i=1}^{N} V_{bi}.\delta_i \qquad kW$$

Referring to Fig. 4,

$$N = \frac{\propto}{\lambda} = \frac{cos^{-1}(1 - \frac{d}{100\, r})}{2\pi/N_B}$$

Where V_{bi} is the absolute speed of bucket i; δ_i is the cut layer thickness of bucket i; N_B is the number of buckets for the wheel and N is the number of bucket cutting the soil simultaneously.

$$\delta_i = \frac{100\, V_m}{n.N_B}.sin\beta_i \qquad (9)$$

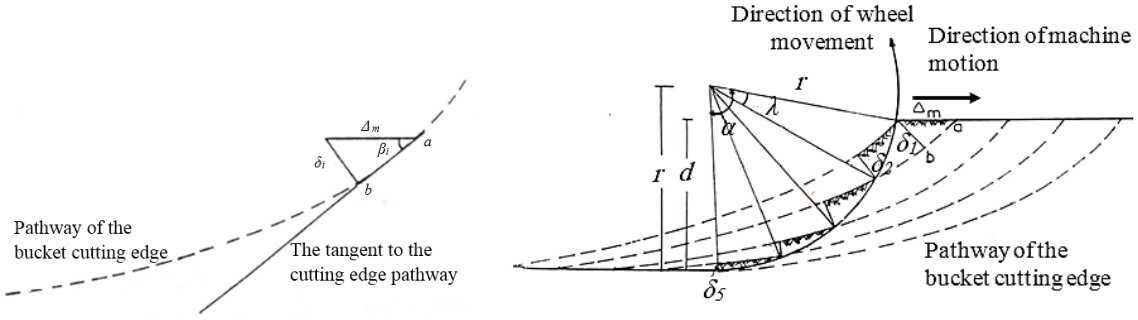

The difference in cut layed thickness on the pathway of bucket cutting edge.

Fig. 4. Determination the thickness of the cut layer for wheel type trenching machine

The angle β_i is the angle between the horizontal direction and the tangent to the curve representing bucket (i) cutting edge pathway and it can be obtained from differentiating ellipse equation;

$$\beta_i = \tan^{-1}\left[\frac{b}{a}.\left(\frac{a^2}{x_i^2} - 1\right)^{-1/2}\right]$$

Where:

$b = r$, $a = r + (V_m/4n)$, $(x_i)^2 = a^2\,[1 - (y^2/b^2)$, and $y_i = r.\cos[\alpha - (i-1)\,.\,a]$

$$\beta_i = \tan^{-1}\left[\left(\frac{1}{1 + (V_m/4\,r.n)}\right).tan(\propto -(i - 1).\lambda)\right]$$

$$\beta_{max} = \tan^{-1}\left[\left(\frac{1}{1+(V_m/4\,r.n)}\right).tan \propto\right] \qquad (10)$$

Using reasonable values for the parameters for the determination of $\sum_{i=1}^{N}\delta_i$ showed that its value = 2.31 δ_{max} with only a deviation of $\pm$1.5 %. Also, instead of using V_{bi}, it was found that using the average speed V_b did not give any serious error.

From the ellipse equation,

$$\bar{V}_b = \pi.n.\left(2r + (V_m/4n)\right) \qquad (11)$$

So,

$$P_c = 0.001 \times \frac{231\pi.K^*.U.W_t.V_m}{N_B}.[2r + (V_m/4n)].sin\beta_{max} \qquad (12)$$

Determination of P_r

$P_r = 0.001\, F_r.V_m$, (Ranjbarian, Askari, & Jannatkhah, 2017)

The resistance force (F_r) due to rolling resistance depends on machine weight (W_m), the weight of cut soil (W_s), the rolling

resistance coefficient (RR), the vertical component of the cutting force (F_{cv}), and the angle ψ between inclined soil surface and the horizontal direction.

$$P_r = 0.001\, V_m . RR . (W_m + W_s + F_{cv}) . cos\psi$$

Referring to Figs (5) and (6), the complete volume of cut of one bucket b_v

$$b_v = \frac{100\, d . W_t . V_m}{n . N_B}$$

While the incomplete volumes of cut of the other buckets could be considered proportional as the areas of the triangles with the same base Δm and decreasing heights L_i with,

$$\sum_{i=1}^{N} L_i = \sum_{i=1}^{N} L_i \left(\frac{N - (i-1)}{N} \right)$$

Also, the weight of soil would include the cut soil in other buckets to the top of the rotating wheel.so, the total volume of cut soil b_{VT} could be

$$b_{VT} = \frac{W_t . \Delta m . L_i}{2} . \left[\frac{1}{N} (N + (N-1) + (N-2) + \cdots + 1) + \left(\frac{N_B}{2} - N \right) \right]$$

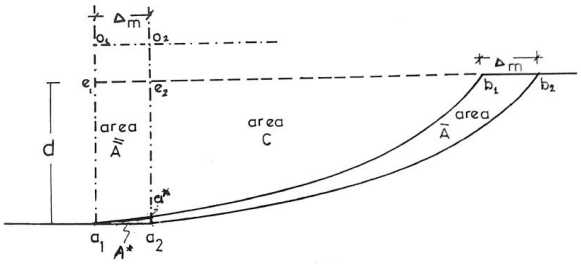

$$A = A^* + A^{/} = A^* + A^{//}$$

$$\Delta_m = 100 V_m . \frac{1}{n . N_B}$$

Fig. 5. Determination the area (A) between the pathway curves of two consecutive bucket cutting edges

$$b_{VT} = \frac{W_t . \Delta m . L_i}{2 \times 2} . (1 + N_B - N)$$

$$W_s = \frac{100\, d . W_t . V_m . \omega}{2 . n . N_B} . (1 + N_B - N)$$

Referring to Fig. 7, the vertical component F_{cv} of the cutting force F_{ci} would be F_{ci} $.sin\beta$. So, the summation of the vertical component of the cutting force would be:

$$F_{cv} = \frac{100\, K^* . U . W_t . V_m}{n . N_B} . \sum_{i=1}^{N} sin\beta_i . sin\beta_i$$

Using reasonable values for the parameters for the determination of $\sum_{i=1}^{N} sin^2\beta_i$ should that its value = $1.77\, sin^2\beta_{max}$ with only a deviation of ± 1.25 %. So,

$$P_r = 0.001\, RR . V_m . cos\psi . \left(W_m + \frac{100\, d . W_t . V_m . \omega}{2 . n . N_B} . (1 + N_B - N) + \frac{177\, K^* . U . W_t . V_m}{n . N_B} . sin^2\beta_{max} \right) \quad (13)$$

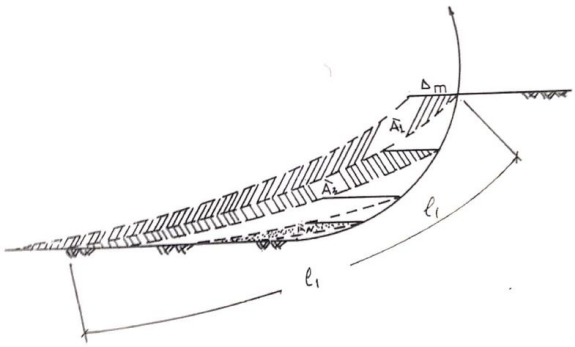

Fig. 6. The determination of the volume of the cut elevated soil

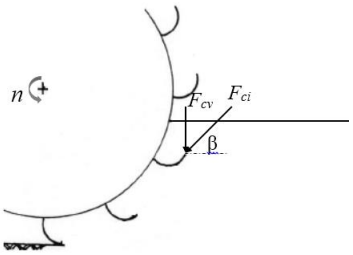

Fig. 7. Cutting force (F_{ci}), vertical component of cutting force F_{cv} and angle β between the horizontal direction and the tangent to the curve representing bucket "i" cutting edge pathway

Determination of *Pi*

The pulling power to overcome slope resistance (Pi) depends on the weight of the machine (W_m), the weight of cut elevated soil (M_s), the machine forward speed (V_m), and the angle (ψ) between the inclined soil surface and the horizontal direction.

$$P_i = 0.001\, V_m.sin\psi.[W_m + W_s]$$

$$P_i = 0.001\, V_m.sin\psi.\left[W_m + \frac{100\ d.W_t.V_m.\omega}{2.n.N_B}.(1 + N_B - N)\right] \quad (14)$$

Determination of P_s

$$P_s = 0.001(F_c + F_r).\left(\frac{S}{100-S}\right).V_m$$

(Ranjbarian *et al.*, 2017)

$$P_s = 0.001\left\{\frac{231K^*.U.W_t.V_m}{n.N_B}.sin\beta_{max} + RR.cos\psi.\left[W_m + \frac{100\ d.W_t.V_m.\omega}{2.n.N_B}.(1 + N_B - N) + \frac{177\ K^*.U.W_t.V_m}{n.N_B}.sin^2\beta_{max}\right]\right\}.\left(\frac{S}{100-S}\right).V_m \quad (15)$$

Determination of P_t

$$P_t = P_b.(1 - \eta_t) \quad (16)$$

Determination of P_e

Referring to Fig. 8, the power P_e required to lift the cut soil would be:

$$P_e = 0.001\ \frac{W_r}{t_{rev}} = 0.001 \times \frac{10^2.\omega.b_{v1}.N_B.\left(2r - \frac{2d}{300}\right)}{t_{rev}} \quad (17)$$

$$P_e = 0.1 \times \omega.W_t.d.V_m.\left(2r - \frac{2d}{300}\right)$$

Referring to equations (2*), (12), (13), (14), (15), (16) and (17);

$$V^2{}_m\left[10^4RR.cos\psi.\omega.W_t.d.(1 + N_B - N) + (3.54 \times 10^4RR.cos\psi.K^*.U.W_t.sin^2\beta_{max}) + \left(462\ K^*.U.W_t.\left(25\pi + S(1 - \pi/4)\right).sin\ \beta_{max}\right) + (10^2 \times \omega.W_t.d.(1 + N_B - N).sin\psi)\right] + V_m\left[200n.N_B.RR.cos\psi.W_t + (2n.N_B.W_m.(100 - S).sin\psi) + (924\pi.K^*.U.W_t.r.n.(100 - S).sin\ \beta_{max}) + \left(200n.N_B.(100 - S).\omega.W_t.d.\left(2r - \frac{2d}{300}\right)\right)\right] - \left(2000P_b.\eta_t.N_B.(100 - S)\right) = 0 \quad (18)$$

$$V^2{}_m + \frac{G}{Q}.V_m - \frac{J}{Q} = 0 \quad (19)$$

Where:

$$Q = Q_1 + Q_2 + Q_3 \quad (20)$$

$$G = G_1 + G_2 + G_3 \quad (21)$$

$$G_1 = n.N_B.W_m.(100RR.cos\psi - (100 - S).sin\psi) \quad (22)$$

$$G_2 = 924\pi.K^*.U.W_t.r.n.(100 - S).sin\ \beta_{max} \quad (23)$$

$$G_3 = 2 \times 10^2n.N_B.(100 - S).\omega.W_t.d.\left(2r - \frac{2d}{300}\right) \quad (24)$$

$$Q_1 = 10^2 \times \omega.W_t.d.(1 + N_B - N).[100RR.cos\psi + sin\psi] \quad (25)$$

$$Q_2 = 462\ K^*.U.W_t.\left(25\pi + S(1 - \pi/4)\right).sin\ \beta_{max} \quad (26)$$

$$Q_3 = 3.54 \times 10^4RR.cos\psi.K^*.U.W_t.sin^2\beta_{max} \quad (27)$$

$$J = 2000P_b.\eta_t.N_B.(100 - S) \quad (28)$$

Applying the rule:

$$V_m = -\frac{b}{2} \pm \sqrt{\left(\frac{b}{2}\right)^2 - \frac{C}{a}} \quad (29)$$

$$\frac{b}{2} = \frac{G}{2Q} \quad (30)$$

$$C = \frac{J}{Q} \quad (31)$$

Equation (29) can be solved for V_m by trial and error method, by giving a reasonable initial value for V_m to solve equations (30) and (31). Using reasonable values for the parameters of equation (29) and using different values of K^* ranged from 1 to 15, resulted in V_m value ranging from 1.38 to 0.17 m s^{-1}.

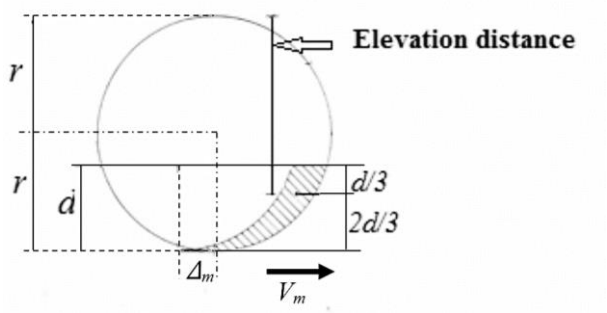

Fig. 8. The elevation distance of the cut soil in wheel type trenching machine

The actual performance rate (*RP*) could be obtained from equation (8) using field efficiency $\eta_t = \eta_s . \eta_w . \eta_{ti}$, where η_s is the efficiency of utilizing the geared speed, η_w is the efficiency of utilizing the proposed width of the machine, and η_{ti} is the efficiency of utilizing the time. However, due to the very low speed of the machine and the actual & theoretical machine width during operation was equals, both η_s and η_w could be considered equal to 1.0.

Table 2- Technical specifications of the wheel type trenching machine

Engine	Daimler Benz (Mercedes) Diesel
Power	130 kW (178 hp) at 1750 rpm
Tank capacity	Fuel 306 lit., Oil 120 lit.
Electricity	24 Vl
Transport speed	0 - 5.0 km h^{-1}
Ground pressure	approx. 3.1 N cm^{-2}
Transmission efficiency	90 %
Digging unit	
Rotating wheel speed	1st speed: 8 rpm. 2nd speed: 19 rpm. 3rd speed: 26 rpm. 4th speed: 34 rpm. 5th speed: 45 rpm. Reverse: 6 rpm.
Wheel diameter	2400 mm.
Buckets number	16
Max. trench depth	1100 mm.
Trench width	350 - 560 mm.
Transport data	
length	8750 mm
Width	8000 mm
Height	2720 mm
Weight	11.562 tons

Field experimental work

The experimental work was carried out through a period of almost one year. The area was in Dakahlia Governorate, meet Ghmr center, Shalaby wa el-Serw village (intersection of latitude 30.7167 and longitude 31.2525), in which the wheel type trenching machine was tested. The specifications of the machine are shown in Table 2. Trench depths of 60 and 90 cm were tested.

Results and Discussion

The average rolling resistance coefficient of the experimental field was taken as 4.0 percent, since it was found ranging between 3.0 and 5.0 percent (Jia & Jia, 2018). The average specific weight of the soil (ω) was found to be 0.011 N cm^{-3} (Jia & Jia, 2018). In addition, the average draft was taken as 10 N cm^{-2} (Jia & Jia, 2018). The average values of field measurements were as shown in Table 3.

Table 3- Average values of field measurements

Field measurements	Ave.	SD	Ave.	SD
Trench depth, cm	60.4	3.1	90.5	3.8
Trench width, cm	35.1	1.15	35.1	1.15
Slip percentage, %	5	---	7	---
Machine forward speed, m s^{-1}	0.33	0.02	0.28	0.11
Wheel rotating speed, rps	0.43	---	0.32	---
K^*; A dimensionless coefficient	12	---	12	---
Angle between inclined soil surface and the horizontal direction, degree	0	---	0	---

Actual performance rate (*RP*) and field efficiency (η_f)

Table 4 shows the breakdown items of the daily machine time, as practically measured in the field. They also show the average of the actual performance rate of the machine and its efficiency.

Table 4- Breakdown items of the daily machine item for the used wheel type trenching machine and its average performance rate and field efficiency

Activities	*Average spent time, min day^{-1}		SD, min day^{-1}	
	Trench depth, cm		Trench depth, cm	
	60.4	90.5	60.4	90.5
Net excavating and pipe laydown	213	180	4.23	5.31
Turning and travelling to start digging another trench	63	71	2.18	2.79
Setup time for reaching the depth	21	33	1.94	2.15
Rest periods	60	60	2.14	2.19
Field quick maintenances	24	27	1.14	2.20
Refill of water and oil tank	23	30	2.23	1.97
Other lost time	21	18	2.19	3.19
Average total time, min day^{-1}	425	419	1.49	5.01
** Total installed length, m day^{-1}	3760	2677	3.15	4.22
Actual performance rate, m min^{-1}	8.85	6.39	2.19	1.23
*** Field efficiency, %	50.1	43.0	2.16	1.18

Theoretical deterioration of the wheel type trenching machine performance rate

To predict the performance rate of the wheel type trenching machine, equations (8), (29), (30), and (31) were used. The specifications of the applied wheel type trenching machine are shown in Table 2. In addition, the field-measured data are shown in Table 3. Using the above mentioned data into equation (30) for the value of *b/2* and into equation (31) for the value of *C* gave the following equations:

For 60.4 cm depth

$$\frac{b}{2} = \frac{1}{2}\left(\frac{13873002.47 + 599354145.38\ sin\beta_{max}}{111938.1 + 154922100.1\ sin\beta_{max} + 5964192\ sin^2\beta_{max}}\right)$$

$$C = \frac{172060200}{111938.1 + 154922100.1\ sin\beta_{max} + 5964192\ sin^2\beta_{max}}$$

Where:

$$\beta_{max} = \tan^{-1}\frac{1}{1+\frac{V_m}{2.064}}$$

Solving equation (29) by trial and error method, gave the computed values of (V_m), Table 5. Applying the computed value of (V_m) into equation (8), gave the predicted value of the performance rate of the wheel type trenching machine:

RP= 60 x 0.309 x 0.501 = 9.29 m min^{-1}.

This predicted value was very close to the experimentally determined value of the performance rate for the 60.4 cm trench depth, which was found to be 8.85 m min^{-1}, Table 5 and Fig. 9. The deviation of the theoretically computed value from the field determined value for the performance rate was only about 5.0 percent.

For 90.5 cm depth

$$\frac{b}{2} = \frac{1}{2}\left(\frac{1195399.9 + 436640065.7 sin\beta_{max}}{223629.1 + 155757306.5\ sin\beta_{max} + 5964192\ sin^2\beta_{max}}\right)$$

$$C = \frac{125349120}{223629.1 + 155757306.5\ sin\beta_{max} + 5964192\ sin^2\beta_{max}}$$

Where:

$$\beta_{max} = \tan^{-1}\frac{3.9288}{1+\frac{V_m}{1.536}}$$

Solving equation (29) by trial and error method, gave the computed values of (V_m), Table 5. Applying the computed value of (V_m) into equation (8), gave the predicted value of the performance rate of the wheel type trenching machine:

RP= 60 x 0.265 x 0.43 = 6.84 m min^{-1}

This computed value was very close to the experimentally determined value of the performance rate for the 90.5 cm trench depth, which was found to be 6.39 m min^{-1}, Table 5 and Fig. 9. The deviation of the theoretically computed value from the field determined value for the performance rate was only about +7.0 percent.

Table 5- The initially proposed and the computed values in the interaction process for the determination of the forward speed of the wheel type trenching machine at 60.4 cm and 90.5 cm depths. (Using trial and error method)

60.4 cm trench depth	V_m proposed value, m s^{-1}	3.000	1.000	0.400	0.309
	V_m computed value, m s^{-1}	0.429	0.336	0.310	0.309
90.5 cm trench depth	V_m proposed value, m s^{-1}	3.000	1.000	0.400	0.265
	V_m computed value, m s^{-1}	0.312	0.276	0.267	0.265

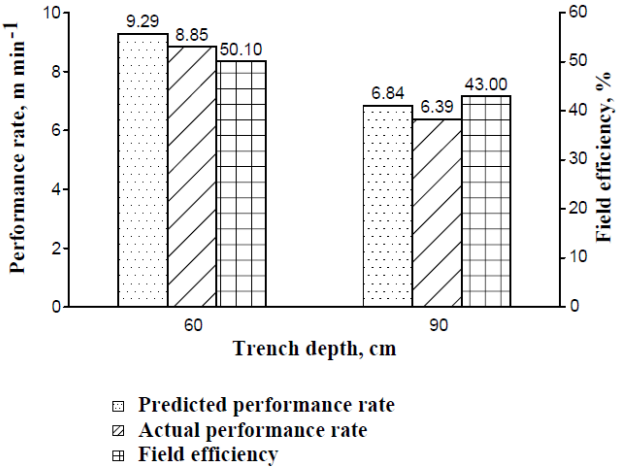

Fig. 9. The actual and predicted performance rate and field efficiency of the wheel type trenching machine

The findings of the used wheel type trenching machine show the degree of accuracy of the mathematically derived equations. These derived equations can be

used with enough confidence to theoretically predict the performance rate of wheel type trenching machine depending on the prevailing operating conditions.

Conclusion

The digging of the trenches is an important process in order to implement the tail drainage projects. This research is concerned with studying the relationship that correlate the performance of the wheel type trencher machine with the factors affecting them, so that the rate of performance can be predicted or controlled through the factors affecting it. Also, a field operating study was conducted under actual operating conditions to test the validity of the derived mathematical equations.

This study showed the validity of the derived equations in predicting the performance rate of chutes. The percentage difference between the performance rate calculated from the equations and the actual field estimated performance rate were 5 and 7% for cutting wheel when they worked at a trench depth of 60.4 and 90.5 cm, respectively. Also, the field efficiency were 43 and 50.1% when the machine working at a trench depth of 60.4 and 90.5 cm, respectively.

References

1. Atangana Njock, P. G., Zheng, Q., Zhang, N., & Xu, Y. S. (2020). Perspective Review on Subsea Jet Trenching Technology and Modeling. *Journal of Marine Science and Engineering*, *8*(6), 460. https://doi.org/10.3390/jmse8060460
2. Day, D. A. (1973). *Construction equipment guide*. John Wiley and Sons., Inc., N. Y., USA, 206-208.
3. Du, Y., Dorneich, M. C., & Steward, B. (2016). Virtual operator modeling method for excavator trenching. *Automation in construction*, *70*, 14-25. https://doi.org/10.1016/j.autcon.2016.06.013
4. Ghonimy, M. (2021). Prediction the performance rate of chain type trenching machine. *Turkish Journal of Agricultural Engineering Research*, *2*(2), 390-402. https://doi.org/10.46592/turkager.2021.v02i02.012
5. Ghonimy, M., Abd El Rahman, E., & Alzoheiry, A. (2022). Mathematical Prediction of Excavating Force and Power of Chain Type Trenching Machine. *Acta Technologica Agriculturae*, *25*(4), 197-204. https://doi.org/10.2478/ata-2022-0029
6. Jia, J., & Jia. (2018). *Soil dynamics and foundation modeling*. New York: Springer.
7. Peurifoy, R. L. (1970). *Construction planning, equipment, and methods*. 2nd ed. McGraw, Hill Kogakusha, Ltd., Tokyo, Japan, pp 695.
8. Ranjbarian, S., Askari, M., & Jannatkhah, J. (2017). Performance of tractor and tillage implements in clay soil. *Journal of the Saudi Society of Agricultural Sciences*, *16*(2), 154-162. https://doi.org/10.1016/j.jssas.2015.05.003
9. Reddy, Y., & Shailesh, P. (2018). Design and Analysis of Excavator Bucket Tooth. *International Journal of Modern Trends in Engineering and Research*, *5*(4), 79-86. https://doi.org/10.21884/IJMTER.2018.5106.Q4FBI
10. Schwap, G. O., Frevert, R. K., Edminster, T.W., & Barnes, K. K. (1966). *Soil and water conservation engineering*. 3rd Ed. 214-218.
11. Sitorus, P. E., Ko, J. H., & Kwon, O. S. (2016). Parameter study of chain trenching machines of Underwater Construction Robots via analytical model. In OCEANS 2016 MTS/IEEE Monterey (pp. 1-6). IEEE. https://doi.org/10.1109/OCEANS.2016.7761072
12. Spencer, A., Machin, J., & Jackson, E. (2007). *Rock cutting With the T750 super trencher*. Unmanned Intervention, New Orleans, LA, 30.

نشریه ماشین‌های کشاورزی
https://jame.um.ac.ir

مقاله پژوهشی
جلد ۱۳، شماره ۱، بهار ۱۴۰۲، ص ۱۳-۱

تجزیه و تحلیل ریاضی برای پیش‌بینی عملکرد ماشین حفاری ترانشه (کانال‌کن) چرخ‌دار

محمد غنیمی[۲،۱*]، منیر مورکاس[۱]، عبداله بدر[۱]

تاریخ دریافت: ۱۴۰۰/۰۳/۳۱
تاریخ پذیرش: ۱۴۰۰/۰۸/۱۰

چکیده

در این مطالعه تحلیلی ریاضی برای تخمین میزان عملکرد ماشین ترانشه‌برداری نوع چرخ‌دار صورت گرفت. این تجزیه و تحلیل ریاضی نهایتا منجر به یک معادله شد و این معادله ریاضی در شرایط عملیاتی مختلف مورد بررسی قرار گرفت. مطالعه عملی عملکرد دستگاه نشان داد که انحراف کارکرد نظری با استفاده از فرمول ریاضی از کارکرد واقعی برای عمق ترانشه ۶۰/۴ و ۹۰/۵ سانتی‌متر به‌ترتیب ۵ تا ۷ درصد بود. همچنین راندمان مزرعه‌ای این نوع ماشین نیز ۴۳ و ۵۰/۱ درصد به‌ترتیب برای عمق ترانشه ۹۰/۵ و ۶۰/۴ سانتی‌متر بود.

واژه‌های کلیدی: زهکشی سفالین، عملکرد ترانشه، مدل‌سازی

۱- گروه مهندسی کشاورزی، دانشکده کشاورزی، دانشگاه قاهره، مصر
۲- گروه تولید و حفاظت از گیاهان، دانشکده کشاورزی و دامپزشکی، دانشگاه قاسم، عربستان سعودی
(*- نویسنده مسئول: Email: mohamed.ghonimy@agr.cu.edu.eg)

https://doi.org/10.22067/jam.2021.71081.1049

Journal of Agricultural Machinery

Homepage: https://jame.um.ac.ir

Research Article
Vol. 13, No. 1, 2023, p. 15-25

Investigation of the Cylinder Liner Wear in Agricultural Tractors

R. Khodabakhshian Kargar[1*], R. Baghbani[2]

1- Assistant Professor, Department of Biosystems Engineering, Faculty of Agriculture, Ferdowsi University of Mashhad, Iran
2- Faculty member, Department of Agricultural Engineering, Technical and Vocational University (TVU), Tehran, Iran
(*- Corresponding Author Email: Khodabakhshian@um.ac.ir)
https://doi.org/10.22067/jam.2022.72790.1066

Received: 02 October 2021
Revised: 27 December 2021
Accepted: 05 January 2022
Available Online: 08 January 2022

How to cite this article:
Khodabakhshian Kargar, R., & Baghbani, R. (2023). Investigation of the Cylinder Liner Wear in Agricultural Tractors. *Journal of Agricultural Machinery*, *13*(1), 15-25. https://doi.org/10.22067/jam.2022.72790.1066

Abstract

The present study aimed to examine the application of accurate and principle-based evaluation of a measuring instrument called the Form Tester in determining and detecting the wear phenomenon in the cylinder liner of agricultural tractors. For this purpose, a cylinder liner of the Perkins 4-248 engine (related to the Massey Ferguson 285 tractor) was manufactured by Keyhan Sanat Ghaem Company was used. The geometric parameters that were measured in this research included roundness, straightness, and concentricity of the cylinder liner. The evaluations on roundness and concentricity of cylinder liner were conducted in 12 circular positions with the same longitudinal distances. The straightness was measured in five lines with the same longitudinal distances in 90° around the cylinder liner environment. The results of the measurements were discussed and analyzed to evaluate the engine status along the functional path of the piston within the cylinder liner. The degree of deviation rate of the parameters indicated significant wear within the cylindrical liner. The wear rate in cross-sections at high and low dead points was significantly greater than that of the same cross-section in the vicinity of the midpoint of the piston movement path inside the cylinder, as well as the cross-sections near the high dead point. The results of this research provide feedbacks for engine designers to apply various changes to the engine and for maintenance and repair engineers to ensure the correct implementation as well as preventive and predictive repair and maintenance strategies.

Keywords: Cylinder liner, Geometric tolerances, Honing process, Tractor, Wear

Introduction

Nowadays, the process of mechanization development highlights that an increase in the operating of agricultural tractors and mechanical power-sharing improves agricultural production. On the other hand, the development of agricultural mechanization heavily relies on how to use this source of power production and how to use the agricultural tractor as the main source of power production. (Karimi, Mesri Gandshamin, & Khadem Alhoseini, 2012; Afsharnia, Asoodar, & Abdeshahi, 2014; Khodabakhshian & Sajadi, 2022). The optimal use of the tractor depends on the quality and durability of its fast-moving parts. If the quality of the parts is not at the desired level, their breakage and wear will cause unwanted stops in the field, and this will affect the technical performance and the economic efficiency of the machine. Therefore, the probability of failure, repair time, and its causes should be considered in the processes (Rohani, Abbaspour-Fard, & Abdolahpour, 2011). In this regard, the rapid development of tractor manufacturing has led to growing expectations for improving the performance of the tractor's engine. Hence, increasing the precision of machining the engine parts of the tractor including the cylinder liner plays a vital role in enhancing the production power of the engine and reducing the fuel consumption, in addition to the direct impact on the amount of

burning oil in the engine and satisfying emission standards (Khodabakhshian & Shakeri, 2011; Söderfjäll, Almqvist, & Larsson, 2016; Kılıç & Temizer, 2016).

Surface roughness after honing operation is regarded as one of the most important parameters in determining the accuracy of machining the cylinder liner. Regarding the Honing process, which is very similar to the grinding process, lines with angles of 45 to 55 degrees are created in the cylinder inner surface by abrasive stones using a specially designed machine to maintain engine oil in these grooves, keep the cylinder wall lubricated, prevent the piston from blocking, minimize the wear of the cylinder liner, and reduce the frictional losses of the engine. For each engine, the designer determines patterns and angles of furrows and grooves of honing to a certain extent. However, if these grooves are created at a much higher angle than the specified value, oil cannot remain in these grooves and returns to the cartel, due to gravity. This trend causes engine rattling, reduces the useful life of the parts, and results in failure. However, if the angles of these grooves are less than the limit, they cause the remaining oil volume in the cylinder wall to be more than the limit, resulting in burning oil in the engine and oil shortage, which can damage other parts (e.g. Bearings and crankshaft) due to the reduced oil pressure (Sudarshan & Bhaduri, 1983; Cabanettes, Dimkovski, & Rosén, 2015; Buj-Corral, Vivancos-Calvet, Rodero-de-Lamo, & Marco-Almagro, 2015).

The Honing process improves the geometric shape of the cylinder liner in terms of its geometric properties, including ovality and conicalness. The ovality of the cylinder because of creating an asymmetric contact surface between the rings and pistons with the cylinder liner wall, increases the friction in the engine and the wear between the ring and the cylinder liner wall. This phenomenon results in the increase of the fuel consumption and the reduction of the output power of the engine and consequently, the useful life reduction of the engine parts over time, with excessive wear between the ring and piston with the cylinder wall (Kim, Kim, & Lee, 2018). In some cases, it has been observed that the liner surface roughness from its allowed range can cause the escape of combustion flame from the contact surface between the ring and the cylinder liner wall and lead to engine power loss and excessive temperature rise, and ultimately, the occurrence of piston seizure (Yusefi *et al*., 2015). Thus, Tractor Manufacturing Companies now apply stricter standards with tight tolerances in the allowed level of cylinder liner roughness, although these standards are different depending on the engine type and the diameter of the cylinder and piston. The precise prediction of Honing parameters reduces the cost of repairs, decreases the time lags for using tractors, provides efficient planning, increases safety, allows financial savings, and enhances economic returns. The optimization of the Honing machine parameters is considered as one of these management systems in the production of cylinder liners (Cabanettes *et al*., 2015; Kim *et al*., 2018).

In Iran, few studies have been conducted to determine the effect of honing parameters on the geometric properties and the wear rate of the cylinder liner in agricultural tractors, as well as the impact of the Honing parameters on the engine functional parameters. Most studies carried out in this area have predicted the maintenance and repair costs of agricultural tractors and determined the economic life of tractors (Almasi & Yeganh, 2002; Khodabakhshian & Shakeri, 2011; Rohani *et al*., 2011). Some researchers have studied the use of the preventive maintenance for agricultural machines (Khodabakhshian *et al*., 2008a, b). Buj-Corral *et al*. (2015) conducted a study in an industrial company and developed models for optimizing the Honing equipment of the driving liner, by comparing the data obtained from the surface roughness test device in the laboratory and the existing Honing machine. In another study, Cabanettes *et al*. (2015) collected information about the surface roughness of the cylinder liner and its associated wear. Yousfi, Mezghani, Demirci, & Mansoria (2015)

examined the impact of plateau honing parameters on the surface roughness of the driving cylinder liner. Kim *et al*, (2018) discussed the effects of Plateau Honing parameters on the friction and wear of the driving cylinder liner.

Furthermore, several studies have been conducted on the correlation between the surface roughness of driving cylinder liner and the Honing parameters by other researchers (Andersson & Tamminen, 2002; Jayadas, Nair, & Ajithkumar, 2007; Ramadan Ali, Mohamed, & Bedewy, 2009; Klein, Fang, & Fang, 2017). However, no information was found regarding the effect of Honing parameters on the wear rate of the cylinder liner of agricultural tractors.

This study presents a precise dimensional and geometrical evaluation on the internal surface of the cylinder liner in agricultural tractors to control the degree of wear variation, which is related to the geometric deviations and changes in the directions of transverse (the cylinder liner is not roundness) and longitudinal (the cylinder liner is not cylindrical) paths. For this purpose, a cylinder liner of the Perkins 4-248 engine (related to the Massey Ferguson 285 tractor) manufactured by Keyhan Sanat Ghaem Company was used to conduct the test. The measured geometric parameters included the roundness, straightness, and concentricity of the cylinder liner.

Materials and Methods

The spatial and temporal domain of research

Keyhan Sanat Ghaem Company, as one of the largest manufacturers of cylinder liners in Iran and the Middle East, was selected as the case study. The current research was conducted in 2021 in this company. Given the purpose of the study, 25 cylinder liners of the Perkins 4-248 engine, which was related to the Massey Ferguson 285 tractor were selected (Fig. 1).

Fig. 1. A sample of the cylinder liner

The tested cylinder liner material is made of high-quality cast iron (GG 25) with a diameter of about 101 mm. Table 1 presents the chemical analysis and mechanical properties of cylinder materials, in which HB represents the hardness range in terms of Brinell.

Table 1- Cylinder liner material specifications

Mechanical Properties		Chemical Properties (wt. %)					
Tensile Strength (MPa)	**Hardness (HB)**	**Cr%**	**S%**	**P%**	**%Mn**	**%Si**	**%C**
Min.225	235	0.5	0.1	0.4	0.9	2.4	3.35

Measuring parameters

The dimensional and geometric specifications of the studied cylinder liner were measured and evaluated using the Formtester MMQ 44, Mahr Company, Germany equipped with the LSQ computational algorithm in the metrology laboratory of the Keyhan Sanat Ghaem Company (Fig. 2). The Formtester device applied in this work was, in fact, a special cylinder liner, which was able to produce correct and principle results with consistent repeatability in the geometric deviations of the liner's inner surface. The approximate transfer speed of the Formtester was 20 mm s^{-1} and the approximate scanning speed of the test device rod during the evaluation period was 20 mm s^{-1}. The evaluations on the roundness and concentricity of the cylinder liner were conducted in 12 circular positions with the same lengthwise distances (Fig. 3). Additionally, the straightness was measured in 5 lines with the same lengthwise distances in 90° around the cylinder liner environment.

Fig. 2. The Formtester used for measuring dimensional and geometric specifications of cylinder liner

All dimensional and geometric specifications of the surface were evaluated with average values of five evaluation tests. The data were analyzed using descriptive statistics such as mean (M), standard deviation (S_D), and combined standard uncertainty (U_C), which is calculated according to the Eq. (1).

$$U_C = \frac{S_D}{\sqrt{n}} \quad (1)$$

Where n represents the number of repetitions of measurements.

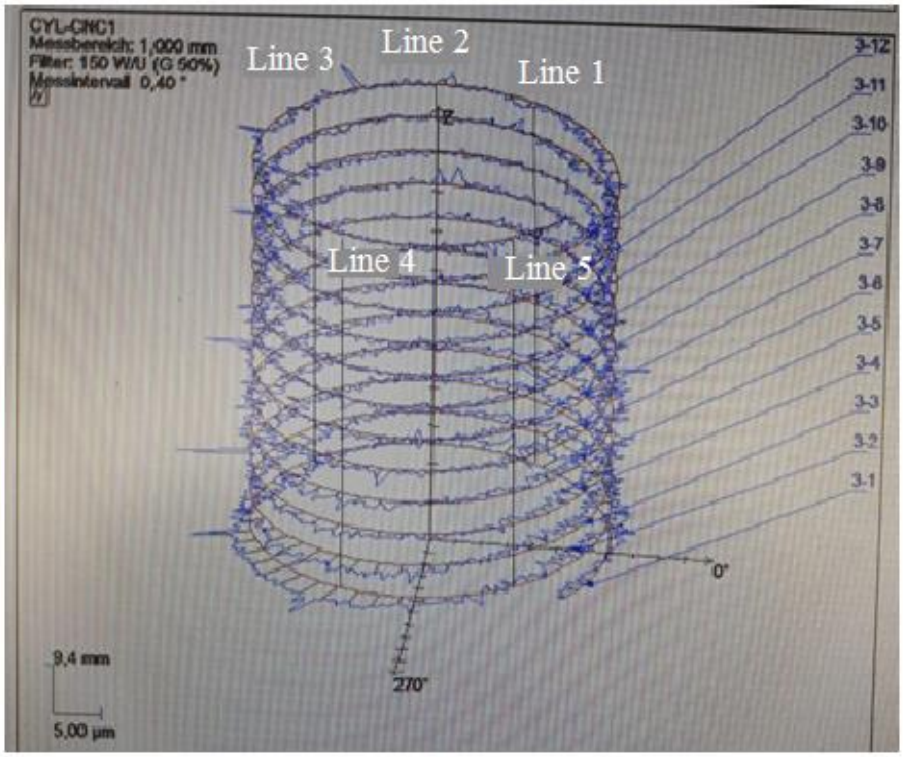

Fig. 3. The position of sections for roundness and straightness measurements

Results and Discussion

Evaluating the uncertainty of measured values: roundness

Table 2 shows the values of the mean, standard deviation (S_D), and combined standard uncertainty (S_D) of roundness measurements for the cylinder liner of Messier Ferguson 285 tractor in the five studied sections (Fig. 3). Due to the relative importance of roundness values and straightness outside of the interval, uncertainty by method B (the method obtained from data and information as a result of previous measurements, experience with general knowledge of physical behavior, properties, tools and specifications provided by the manufacturer were not taken into account for combined standard uncertainty values. As a result, the combined standard uncertainty was only evaluated using method A (based on measurements performed in repeatable conditions). The accuracy and uncertainty of all evaluations were carried out within the standard limits authorized by the manufacturer (customer).

Table 2- Mean, standard deviation, and combined standard uncertainty of roundness measurement

Measuring Position	Repeat 1	Repeat 2	Repeat 3	Repeat 4	Repeat 5	Mean	S_D	U_C
Roundness values (µm)((Based on the minimum error of the crossing circle with the diameter of the cylinder liner from the relevant section)								
Circle 1	18.5	18	18.8	18.9	18	18.44	0.4278	0.1913
Circle 3	25	24.5	24.9	24.7	24.8	24.78	0.1924	0.0860
Circle 6	28.3	28.6	28.7	28.6	28.4	28.52	0.1643	0.0735
Circle 9	37.2	37.3	36.9	36.8	37.1	37.06	0.2074	0.0927
Circle 12	82.5	82.6	82.8	83	83	82.78	0.2280	0.1020

The results of the roundness measurement values outside the interval

The results of the average values of roundness outside the customer's expected range (Ra values) examined for five samples of the studied sections were presented in Figure 3 for the inner surface of the tested cylinder liner with the nominal internal diameter which was measured in Figure 4. This amount of roundness was measured based on the passage of two peripheral and intersecting circles from the cross-sectional profile of the part in the studied section, which was done using the LSQ computational algorithm programmed on the Formtester. The following cases can be concluded according to the analysis performed on the roundness patterns of the internal surface of the cylinder liner illustrated in Fig. 4.

As expected, in the section related to Circle 12 (which is close to the high point of death) due to oil shortage, the highest deviation from the nominal dimension was 102.1152 mm and also the highest value of the mean roundness outside the interval was 82.9 µm which was obtained in this section. As shown in Fig. 4, the smallest deviation from the nominal dimension is 102.0125 mm in the vicinity of the piston stroke midpoint(piston return path) (section 6) while the roundness outside the interval in the circle related to this section is about 28.8 µm. However, the lowest amount of roundness near the dead point (circle 1 related) was obtained at 18.7 µm.

As mentioned, the lowest amount of deviation from the nominal dimension as well as the relatively small amount of roundness was related to the circular cross section No. 6, which had the least inner surface wear changes of the cylinder liner. The reason for low fluctuation at this position may be due to good lubrication and low lateral forces imposed on the piston.

Although the circular section adjacent to the low dead point (section 1) represented the lowest roundness outside the interval, the variation rate of this parameter was higher at this section, which can be perceived from the amount of deviation resulting from the measurement results in this section (Table 2). This issue may be related to the position of the retaining forces of connecting rod while passing this section. In general, in sections near the low and high dead points, the variation rate of roundness outside the interval was more perceptible, due to the same retaining forces of the connecting rod during the piston passage (Table 2).

According to the above results and Figure 6, it was concluded that the device software generates a geometric index reference from the ideal and accurate shape of a number of one or more irregularly scanned sections that provide information and reference data related to the sections which can be utilized in evaluating the final values of the geometric indices of the investigated section.

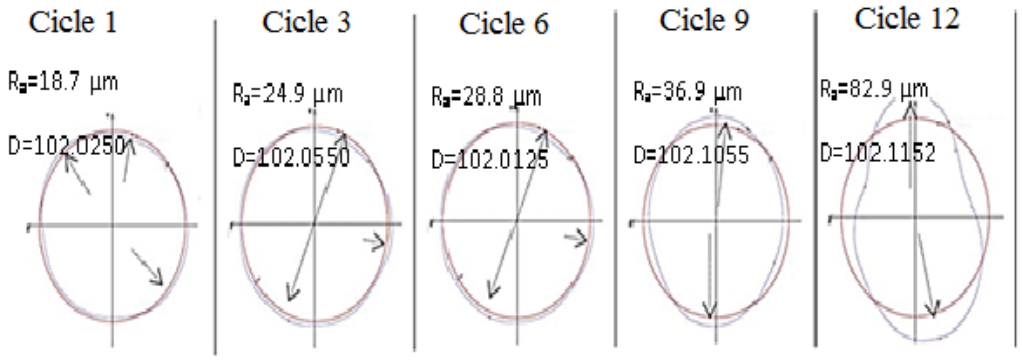

Fig. 4. Roundness measurements and diameter records of the internal surface of the cylinder liner in the studied cross-area position

The results of concentricity measurement values

Given the values of the roundness measurements on the internal surface of the cylinder liner in different transverse positions, the concentricity values of 60.6, 52.5, 45.4, and 28.5 μm were obtained between circles 12 and 1, 12 and 3, 12 and 6, and 12 and 9 around the vertical axis demonstrated in Fig. 3, respectively. These results justify the values of the deviation from the nominal dimension resulting from the severe wear mechanisms in the cylinder liner, which are observed during service and maintenance.

The results of straightness measurement values outside the interval

Fig. 5 shows a report of five lengthwise profiles in the positions of 12 sections studied along the internal surface of the cylinder liner. The maximum straightness value (S_a) obtained from measurements along each longitudinal profile indicates the deviation extent of the domain around the guideline of the cylinder liner (vertical axis in Fig. 3) derived from the appropriate LSQ technique.

The results of the straightness values related to five profiles addressed in Fig. 5 elaborate on the following points:

Uneven wear is perceived along with all longitudinal profiles. Each point on the inner surface of the cylinder liner is exposed to different environmental and dynamic conditions of pressure, friction, lubrication pattern, slip speed, the temperature at the point of contact, and contact force. Therefore, it is necessary to evaluate the fluctuations of the geometric condition of the inner surface of the cylinder liner to predict the signs of surface failure. Each point on the inner surface of the cylinder liner is exposed to different environmental and dynamic conditions of pressure, friction, lubrication pattern, sliding speed, point of contact temperature, and contact force.

The maximum wear rate was always obtained at the contact surface of the first piston rings at the high dead point with mean values of 80.2, 60.6, 32.5, 18.2, and 44.4 μm for the longitudinal profiles related to the lines 1, 4, 5, 3, and 2, respectively (Fig. 3). These cases can be justified by adverse and undesirable tribological conditions at the TDC position. As stated, the maximum straightness deviation (80.2 μm) in the longitudinal profile 1 during the impact period is formed as a quick direct reaction force to the lateral force response at high combustion temperatures. These results and findings are in coinciding with the studies conducted by El-Sherbiny, (1982); Schneider *et al*., (1993); Kilic, Aguirre-Cruz, & Raman (2007); Nabnu, Ren, Yasuda, Zhu, & Wang (2008); Kumar, Prasad Rao, & Hari Narayana Rao, (2015).

The amplitude of the grooves associated with the true tolerance of the inner surface of the cylinder liner showed the highest value for the longitudinal profiles 1 and 4 near the low point of death due to the lateral inertia reaction of the piston, while the longitudinal profiles 5 and 3 showed the lowest amplitude, respectively.

Conclusion

In the present study, geometric measurements of the inner surface of the cylindrical liner were carried out using a Formtester device. Compared to the design tolerance interval (provided by the customer), the measurements indicated that the Formtester device is a new acceptable diagnostic tool for controlling wear and error rate. The dimensional evaluation of the inner diameter of the cylindrical liner in various transverse positions (12 studied sections) along the piston movement path within the cylinder confirmed the previous results and findings, which were obtained using other more sophisticated evaluation techniques.

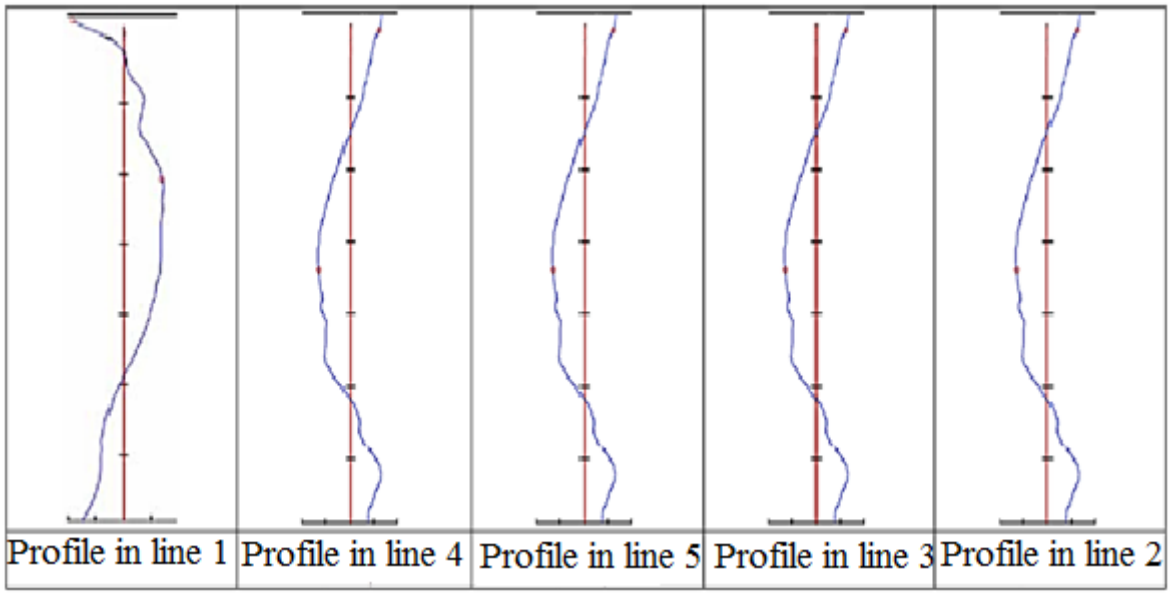

Fig. 5. Straightness measurements of the internal surface of a cylinder liner in the studied cross-area situation

Wear at transverse sections at high and low dead points was significantly greater than that of the same transverse section in the vicinity of the piston movement midpoint inside the cylinder, as well as the transverse sections adjacent to the high dead point. This phenomenon is due to the presence of the engine oil layer maintained in that position.

Investigating the straightness of the cylinder liner at the position of the studied sections indicates non-uniform wear along with all the longitudinal profiles. The maximum wear rate was always at the contact surface of the first piston rings at a high dead point with mean values of 80.2, 60.6, 32.5, 18.2, and 44.4 μm for the longitudinal profiles related to the lines 1, 5, 4, 3, and 2, respectively. The results of this research can provide feedbacks for engine designers when applying various changes to the engine, as well as maintenance and repair engineers to ensure the correct implementation and suggest predictive and preventive maintenance strategies.

Acknowledgment

The present study was conducted in the form of a research project, No. 47948, with the support and cooperation of the Faculty of Agriculture of Ferdowsi University of Mashhad.

References

1. Afsharnia, F., Asoodar, M. A., & Abdeshahi, A. (2014). Regression analysis and presentation of failure rate model and its effective factors in some tractors of Khuzestan province. *Journal of Agricultural Engineering*, *36*(2), 49-58. (In Persian). https://agrieng.scu.ac.ir/article_10478.html
2. Almasi, M., & Yeganeh, H. M. (2000). Determining the appropriate mathematical model for forecasting the costs of maintenance and repair of agricultural tractors used in the Karun Sugar Crop Industry. *Journal of Agricultural Sciences of Iran, 33(4), 707-716.* (In Persian). https://sid.ir/paper/436813/fa
3. Andersson, P., & Tamminen, J. (2002). *Piston Ring Tribology: Aliterature Survey*, Helsinki Univ., VTT Research Notes 2178. https://www.vttresearch.com/sites/default/files/pdf/tiedotteet/2002/T2178.pdf

4. Buj-Corral, I., Vivancos-Calvet, J., Rodero-de-Lamo, L., & Marco-Almagro, L. (2015). Comparison between Mathematical Models for Roughness Obtained in Test Machine and in Industrial Machine in Semifinish Honing Processes. *Procedia Engineering, 132*, 545-552. https://doi.org/10.1016/j.proeng.2015.12.531
5. Cabanettes, F., Dimkovski, Z., & Rosén, B. G. (2015). Roughness variations in cylinder liners induced by honing tools' wear. *Precision Engineering, 41*, 40-46. https://doi.org/10.1016/j.precisioneng.2015.01.004
6. El-Sherbiny, M. (1982). *Cylinder Liner Wear*. 9th Leeds-Lion Symposium on Tribology 2, 132-138. https://scholar.cu.edu.eg/?q=mgs/node/82857
7. Jayadas, N. H., Nair, K. P., & Ajithkumar, G. (2007). Tribological Evaluation of Coconut Oil as an Environment-Friendly Lubricant. *Tribology International, 40*(2), 350-354. https://doi.org/10.1016%2Fj.triboint.2005.09.021
8. Karimi, S., Mesri Gandshamin, T., & Khadem Alhoseini, N. (2012). Mathematical modeling of maintenance costs and analysis of economic useful life of agricultural tractors (Case study of West Azerbaijan province). *Agricultural Knowledge and Sustainable Production, 22*(4), 87-98.
9. Khodabakhshian, R., & Sajadi, S. (2013). Evaluation of the Plateau Honing on the Friction and Wear Cylinder Liners in Agricultural Tractors. *Journal of Agricultural Machinery, 12*(1), 55-66. https://doi.org/10.22067/jam.v12i1.88869
10. Khodabakhshian, R., & Shakeri, M. (2011). Prediction of repair and maintenance costs of farm tractors by using of Preventive Maintenance. *International Journal of Agriculture Sciences, 3*(1), 39-44. https://doi.org/10.9735/0975-3710.3.1.39-44
11. Kılıç, K. I., & Temizer, I. (2016). Tuning macroscopic sliding friction at soft contact interfaces: Interaction of bulk and surface heterogeneities, *Tribology International, 104*, 83-97. https://doi.org/10.1016/j.triboint.2016.08.024
12. Kim, E. S., Kim, S. M., & Lee, Y. Z. (2018). The effect of plateau honing on the friction and wear of cylinder liners. *Wear, 400-401*, 207-212. https://doi.org/10.1016/j.wear.2017.09.028
13. Klein, S., Fang, S., & Fang, D. (2017). Analysis of Different Surface Structures of Hard Metal Guiding Stones in the Honing Process. *Procedia Manufacturing, 10*, 265-275. https://doi.org/10.1016/j.promfg.2017.07.055
14. Kilic, B., Aguirre-Cruz, J. A., & Raman, S. (2007). Inspection of the Cylindrical Surface Feature after turning using Coordinate Metrology. *International Journal of Machine Tools & Manufacture, 47*(12-13), 1893-1903. https://doi.org/10.1016/j.ijmachtools.2007.03.007
15. Kumar, A., Prasad Rao, A. A. V., & Hari Narayana Rao, L. (2015a). Design and Analysis of Dry Cylinder Liners Used in Diesel Engines. *International Journal of Science Engineering and Advance, 3*(9), 1-9. https://core.ac.uk/download/pdf/235196536.pdf
16. Kumar, A., Prasad Rao, A. A. V., & Hari Narayana Rao, L. (2015b). A competing risk model for the reliability of cylinder liners in marine Diesel engines. *Reliability Engineering & System Safety, 8*(94), 1299-1307. https://doi.org/10.1016/j.ress.2009.01.010
17. Nabnu, T., Ren, N., Yasuda, Y., Zhu, D., & Wang, Q. J. (2008). Micro-Textures in Concentrated Conformal-Contact Lubrication: Effects of Texture Bottom Shape and Surface Relative Motion. *Tribology Letters, 29*(3), 241-252. https://doi.org/10.1007/s11249-008-9302-9
18. Ramadan Ali, S. H., Mohamed, H. H., & Bedewy, M. K. (2009). Identifying Cylinder Liner Wear using Precise Coordinate Measurements. *International Journal of Precision Engineering and Manufacturing, 10*, 19-25. https://link.springer.com/article/10.1007/s12541-009-0088-y
19. Rohani, A., Abbaspour-Fard, M. H., & Abdolahpour, S. (2011). Prediction of tractor repair and maintenance costs using Artificial Neural Network. Expert Systems with Applications 38: 8999-9007. *Iranian Journal of Agricultural Science, 4*(33), 707-716. https://doi.org/10.1016/j.eswa.2011.01.118

20. Schneider, E. W., Blossfeld, D. H., Lechman, D. C., Hill, R. F., Reising, R. F., & Brevick, J. E. (1993). Effect of Cylinder Bore Out-of-Roundness on Piston Ring Rotation and Engine Oil Consumption SAE. *International Journal of Materials and Manufacturing, 5*, 796-930. https://doi.org/10.4271/930796
21. Söderfjäll, M., Almqvist, A., & Larsson, P. (2016). Component test for simulation of piston ring –Cylinder liner friction at realistic speeds. *Tribology International*, *104*, 57-63. https://doi.org/10.1016/j.triboint.2016.08.021
22. Sudarshan, T. S., & Bhaduri, S. B. (1983). Wear in cylinder liners. *Wear, 91*(3), 269-279. https://doi.org/10.1016/0043-1648(83)90072-8
23. Yousfi, M., Mezghani, S., Demirci, I., & Mansoria, M. E. (2015). Smoothness and plateauness contributions to the running-in friction and wear of stratified helical slide and plateau honed cylinder liners. *Wear, 332-333*, 1238-1247. https://doi.org/10.1016/j.wear.2014.11.011

نشریه ماشین‌های کشاورزی
https://jame.um.ac.ir

مقاله پژوهشی
جلد ۱۳، شماره ۱، بهار ۱۴۰۲، ص ۲۵-۱۵

بررسی سایش بوش سیلندر در تراکتورهای کشاورزی

رسول خدابخشیان کارگر[1*]، رضا باغبانی[2]

تاریخ دریافت: ۱۴۰۰/۰۷/۱۰
تاریخ پذیرش: ۱۴۰۰/۱۰/۱۵

چکیده

در این تحقیق کاربرد ارزیابی‌های دقیق و اصولی یک دستگاه ابزار اندازه‌گیری به نام فرم تستر در تعیین و تشخیص پدیده سایش در بوش سیلندر تراکتورهای کشاورزی مورد مطالعه و ارزیابی قرار گرفت. بدین منظور از بوش سیلندر موتور پرکنیز ۴/۲۴۸ مربوط به تراکتور مسی-فرگوسن ۲۸۵ تولیدی شرکت کیهان صنعت قائم استفاده گردید. پارامترهای هندسی اندازه‌گیری‌شده شامل گردی، تلرانس راستی و هم‌مرکزی سطح داخلی بوش سیلندر بود. ارزیابی‌های میزان گردی و هم‌مرکزی بوش سیلندر در ۱۲ موقعیت دایره‌ای با فواصل طولی یکسان صورت گرفت. تعیین تلرانس راستی مورد اندازه‌گیری نیز در ۵ خط با فواصل طولی یکسان به‌صورت ۹۰ درجه پیرامون محیط بوش سیلندر صورت گرفت. نتایج حاصل از اندازه‌گیری‌ها به‌منظور بررسی و ارزیابی وضعیت موتور در طول مسیر عملکردی پیستون در درون بوش سیلندر آن مورد بحث، بررسی و تجزیه و تحلیل قرار گرفتند. وضعیت شدت انحرافات پارامترهای مورد مطالعه نشان‌دهنده وقوع میزان سایش قابل‌توجه در درون بوش سیلندر بود. به‌طوری‌که میزان سایش در مقاطع عرضی در نقاط مرگ بالا و پایین به مراتب بیشتر از میزان سایش صورت گرفته در همان مقطع عرضی در مجاورت نقطه وسط مسیر حرکت پیستون در درون سیلندر و همچنین مقاطع عرضی در مجاورت نقطه مرگ بالا بود. نتایج این بررسی به نوبه خود بازخوردهایی برای طراحان موتور در هنگام اعمال تغییرات مختلف در موتور و هم برای مهندسان نگهداری و تعمیرات به‌منظور اجرای صحیح نگهداری و تعمیرات پیشگیرانه و پیش‌بینانه را فراهم می‌آورد.

واژه‌های کلیدی: بوش سیلندر، تراکتور، تلرانس‌های هندسی، سایش، فرآیند هونینگ

۱- استادیار، گروه مهندسی بیوسیستم، دانشکده کشاورزی، دانشگاه فردوسی مشهد، ایران
۲- عضو هیات علمی، گروه مهندسی کشاورزی، دانشگاه فنی و حرفه ای، تهران، ایران
(*- نویسنده مسئول: Email: Khodabakhshian@um.ac.ir)

https://doi.org/10.22067/jam.2022.72790.1066

Journal of Agricultural Machinery

Homepage: https://jame.um.ac.ir

Research Article
Vol. 13, No. 1, 2023, p. 27-39

Detection of Cucumber Fruit on Plant Image Using Artificial Neural Network

D. Mohammadzamani[1*], S. M. Javidan[2], M. Zand[3], M. Rasouli[4]

1- Assistant Professor, Department of Biosystems Engineering, Takestan Branch, Islamic Azad University, Takestan, Iran
2- Department of Biosystems Engineering, Tarbiat Modares University, Tehran, Iran
3- M.Sc. Graduated, Department of Biosystems Engineering, Takestan Branch, Islamic Azad University, Takestan, Iran
4- Assistant Professor, Department of Plant Breeding, Takestan Branch, Islamic Azad University, Takestan, Iran
(*- Corresponding Author Email: dr.dmzamani@gmail.com)
https://doi.org/10.22067/jam.2022.73827.1077

Received: 24 November 2021
Revised: 23 January 2022
Accepted: 21 February 2022
Available Online: 21 February 2022

How to cite this article:
Mohamadzamani, D., Javidan, S. M., Zand, M., & Rasouli, M. (2023). Detection of Cucumber Fruit on Plant Image Using Artificial Neural Network. *Journal of Agricultural Machinery*, *13*(1), 27-39. https://doi.org/10.22067/jam.2022.73827.1077

Abstract

The main purpose of this study was to provide a method for accurately identifying the position of cucumber fruit in digital images of the greenhouse cucumber plant. After balancing the brightness histogram of the desired image, it multiplies the image with a window containing the image of a cucumber fruit, which causes larger coefficients to be obtained in areas with suspected cucumber. By extracting these local maximums, clusters of initial points are obtained as possible windows of cucumber existence. Then, in order to accurately detect the location of the cucumbers, these points and areas around them are referred to a neural network that has been trained using a number of images including cucumber images, non-cucumber images and their optimal responses. The proposed method was implemented in the Simulink toolbox of MATLAB software. The proposed method was then simulated using this network structure and tested on 120 images obtained from a greenhouse by a digital camera. The areas obtained from this network led to the accurate detection of the location of the cucumbers in the image. The proposed method was then simulated and tested on 120 images. The proposed method had a low error and was able to detect high levels of cucumber fruit in the images. This detection took an average of 5.12 seconds for each image. The accuracy of the network in correctly identifying the position of the cucumber fruit in the images was 95.3%. This method had low error and was able to detect a high rate at a good time of cucumber fruits in discover images.

Keywords: Artificial Neural Network, Detection, Greenhouse cucumber, Image processing

Introduction

Greenhouse cucumber is one of the important high yields horticultural crops which are widely cultivated in Iran. Due to the rapid growth of cucumber and its difficult and time-consuming harvest, it is necessary to mechanize the greenhouse cucumber harvesting operations. One way to improve the quality and health of the production is to use automated machines without the involvement of human agents (Li, Lee, & Hsu, 2011). In the past, most farming operations were done manually using manpower. With recent advances in various technologies, and consequently in agricultural engineering, and in particular agricultural machinery, the role of manpower in agricultural activities has diminished (Zhao, Gong, Huang, & Liu, 2016). The robot consists of three main parts, including mechanics, electronics, and software. The core of the robot's software is the visual machine, which gives the robot an understanding of the world around it and enables the robot to perform its tasks correctly. For example, in a cucumber harvesting robot, the visual machine has the task of using image processing and machine learning techniques to determine the location of the cucumber fruit so

that the robot can detect the fruit and remove it from the stem (Li, Miao, Yang, & Wang, 2019). So the purpose of image processing of greenhouse cucumber bushes by the neural network is to provide a convenient and efficient way, without the need for sophisticated and specific hardware in greenhouse images processing in order to detect cucumber fruit in these images and to separate it from the plant. The results of this detection should be applicable to the mechatronic portion of the greenhouse cucumber harvesting robot.

Yuan *et al*. (2008) proposed a visual machine algorithm for detecting cucumber fruit based on near-infrared spectral imagery. They first eliminated the problem of fragmentation of similar colors in complex environments by shooting near-infrared monochromatic spectra at 85 nm. Then, to distinguish the fruit, they used image fragmentation using threshold processing. Then, by adaptive pattern extraction software, they divided the images into other sub-branches, and finally eliminated possible noises, including parts of the stem and leaf. This method was tested on 40 images including 30 images containing cucumber and 10 images without cucumber taken from a greenhouse environment and the results showed that the detection accuracy was 83.3% and 100%, respectively. Yuan, Li, Feng, & Zhang (2010) developed an algorithm for detecting cucumber fruit in a greenhouse environment. They first used a binocular stereo imaging system to capture near-infrared monochrome images to eliminate the problem of color segmentation in complex environments, and then they proposed an algorithm to identify the cucumber fruit to distribute gray matter histograms, threshold processing and noise removal using morphological analysis and finally feature extraction using pattern recognition. The results of the experiment on 120 greenhouse cucumber images showed that the proposed algorithm can detect fruit at a rate of 86%. Li, Zhao, Zhao, Gao, & Xu (2017) prepared a technique based on texture analysis and color analysis for detecting cucumber in greenhouse. In this research RGB image was converted to gray-scale image and HSI image to perform algorithm, respectively. MSER and HOG were applied to texture analysis in gray-scale image. The support vector machine is the classifier used for the identification task. The accuracy of this method was 83.2%. Yuan *et al*. (2008) developed an optical machine algorithm for the detection of cucumber fruit based on near-infrared spectral imaging. They first eliminated the problem of splitting similar colors in complex environments by single-infrared imaging at 85 nm then, using threshold processing, image segmentation to detect fruit and split the images into subcategories by extraction software and eventually eliminated potential noise including parts of the stem and leaves. The method was tested on 40 images containing 30 images of cucumber and 10 images of no cucumber capture in a greenhouse environment and the results showed that the accuracy of detection was 83.3% and 100%, respectively. Hayashi, Ganno, Ishii, & Tanaka (2002) have designed and fabricated an eggplant harvesting robot using an optical machine algorithm to detect eggplant fruit. The basis of their visual machine algorithm was the color characteristics and morphological characteristics of the eggplant fruit. So that in the images taken from the product using eggplant color characteristics removed it from the field and since some parts of the leaf and stem of the plant could be mistaken for the fruit as the morphological characteristics of eggplant fruit with the help of fuzzy feedback control model. Their system was able to harvest the eggplant correctly at a 62.5% rate. Liu *et al*. (2019) developed Resnet-101 for cucumber fruits detection in greenhouses based on instance segmentation. This method is selected as the backbone of Mask RCNN with feature pyramid network (FPN).The test results are compared with that of original Mask RCNN. The score of improved Mask RCNN in test results reaches 89.47%, which is higher than the other methods. The average elapsed time of improved Mask RCNN is

0.3461 s, which is only lower than the original Mask RCNN.

The main objective of this study is to present a method for real-time detection of cucumber fruit location in greenhouse images. The main difference in the fruit recognition mechanism in images with the same color spectrum is the complexity in distinguishing fruit from leaf and stem. This was also the case with images of cucumber fruit. Therefore, in this study, an innovative method was used to separate the color characteristics of cucumber fruit from background.

Materials and Methods

Proposed method

This research was conducted in the research greenhouse of Islamic Azad University, Takestan Branch in 2021. This research seeks to provide an efficient way of detecting cucumber fruit in greenhouse images which can be used to design greenhouse cucumber harvesting robots. Therefore, this method should be far from complex so that it can be practically implemented and also does not require sophisticated hardware. Processing time was also important in this study and should be as short as possible for the greenhouse cucumber harvesting robot to have a good efficiency (Ma, 2018). Another challenge with cucumber fruit detection is that the greenhouse cucumber has a similar color to its leaves and stems, thus color and background color differences cannot be used to detect it. So another feature should be used to reduce the complexity of the issue (Lin, Tang, Zou, Xiong, & Fang, 2019; Bao, 2016). Finally, a method for greenhouse cucumber detection using window correlation coefficient including an arbitrary cucumber on image and neural network classifier was presented. The proposed method consists of two parts. The first part includes finding windows that are more likely to have cucumbers, which will explain how to find them. Each window is identified by its center. The output of the first part is a number of points that are considered to contain cucumber. These places are called inaccurate centers, because these windows do not contain cucumbers and their location is slightly different from the actual cucumbers in the image. Here comes the second part, which is the inaccurate space search algorithm. In this algorithm, space exploration requires a cucumber to accurately detect windows to test the presence and absence of cucumbers. It is a neural network trained with windows with and without cucumber. These parts are presented in more detail in the following.

Inaccurate determination of cucumber location

The purpose of this section is to identify inaccurate windows which may contain cucumbers. A large image contains thousands of windows. If the window is identified by its center which is a dot or a pixel, we can approximate the number of pixels of the window image by approximating the margins. The problem is a large number of windows. With a large number of operations that occur on each window, it is not possible to process all the windows at the desired time. On the other hand, cucumber fruit color information cannot be used. The main idea is to apply correlation coefficients. The correlation coefficient of a window containing an arbitrary cucumber with the cucumber in the image produces a larger value than other parts of the image such as the background. The correlation is equal to moving the window over the image and multiplying it internally. In order to determine the incorrect centers, the histogram balancing process is performed on the input image first. This is done to create the highest possible contrast. The result is then multiplied by a window of arbitrary cucumber image that produces larger coefficients in areas with suspected cucumber presence. By extracting these local maximums, clusters of initial points are obtained as inaccurate centers of potential cucumber windows. Figure 1 shows the general outline of this method.

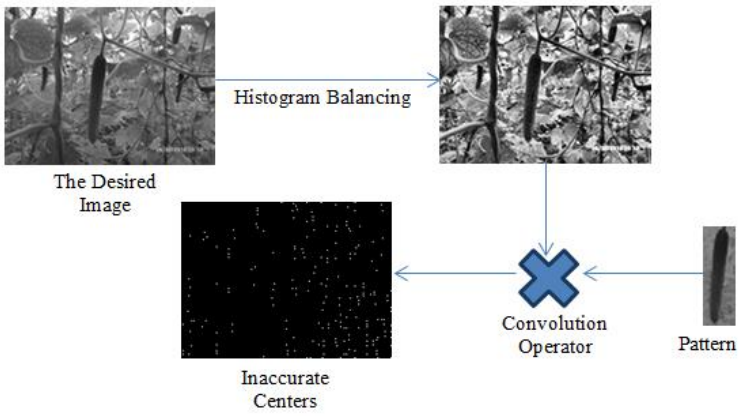

Fig. 1. Total structure for determining the inaccurate center of the windows containing cucumber

In practice, to increase the accuracy of this method and to reduce the dependence on the lighting conditions, two identical cucumber images with two different contrasts were used to determine the incorrect centers, each individually multiplied by the desired image and the sum of the points obtained.

Precise detection of cucumber location

According to the test the incorrect centers in the previous section, which are centered on rectangular windows, either do not contain cucumbers in general or that the center of the windows on the cucumber center does not match the image. In this situation, if necessary, an algorithm is needed to investigate the space around these inaccurate centers to find the best answer for the presence of cucumbers. The following algorithm provides such a possibility.

A. Inaccurate centers are first marked to refer to the network.

B. Until a test center is not found:

1. Return the marked centers to the neural network.

2. If the neural network returns a value greater than the threshold for each center, the lateral pixels are marked. Finally, only those necessary areas have been investigated, and the algorithm provides a great saving in detecting cucumbers.

Extracting features

Referencing the window to the neural network is not done directly. Rather, there is a class for extracting window features, and these are the properties vectors that go to the neural network for the presence or absence of cucumber. These extracted properties make the cucumbers detection resistant to changing ambient light. The feature extraction class used the Gabor filter (Gabor wavelet transform). Gabor wavelet transform is used like other wavelet transforms due to its unique properties in the areas of image processing and visual machine (Fernandes, 2015). These wavelets provide the background for understanding the frequency of images and analyzing them in the field of location and their greatest advantage is the slow changes in the frequency domain. Gabor's 2D functions enhance the edges as well as bumps of the image. If the input image is with light intensity values of gray surfaces, the image wavelet transform is calculated according to Eq. (1) from the convolution of one member of the wavelet family with the input image (Mohamadzamani, Sajadian, & Javidan, 2020; Vakilian & Massah, 2016).

$$\psi_{\mu,\upsilon}(z) * O_{\mu,\upsilon}(z) = I(z) \quad (1)$$

Where * denotes the convolution operator, O is the result of the conversion, ψ is the wavelet used to convert with μ and magnification υ. The Gabor wavelet equation is, in fact, a simple plane wave with a specific frequency and direction trapped under a Gaussian function. This equation can be defined in different shapes and forms depending on the coordinate system, whether

polar or Cartesian, and the form Eq. (2) is the most common form of representation in various articles (Mohamadzamani *et al.*, 2020; Vakilian & Massah, 2016).

$$\psi_{u,v}(z) = \frac{\|k_{u,v}\|^2}{\delta^2} exp\left(\frac{-\|k_{u,v}\|^2 \|z\|^2}{2\delta^2}\right)\left(e^{ik_{u,v}z} - e^{\frac{-\delta^2}{2}}\right) \quad (2)$$

In Eq. (2), K denotes the wave length and direction and is calculated from Eq. (3):

$$\phi_\upsilon = \mu\frac{\pi}{8}k_\upsilon = \frac{k_{ma}}{f^\upsilon} k_{\mu,\upsilon} = k_\upsilon e^{i\phi\mu} \quad (3)$$

As it is known from Eq. (3), μ is multiplied by π/8 and has a phase number k, so it will have an integer value of zero to seven and ϕ is known as the phase offset of the function. Larger quantities produce a wave with duplicate directions. U can also have a value between zero and four and in total forty wavelets can be obtained with different directions and sizes (3 and 2). For the better analytical understanding of this wavelet, one of the 128 × 128 dimensions and the parameters δ = 2π, k_{ma} = π, f = f =√2, μ = 4, υ = 7 is shown in Figure 2 (Mohamadzamani *et al.*, 2020; Vakilian & Massah, 2016).

According to Figure 2, the Gabor wavelet is a plate wave with reduced amplitude. Figure 3 shows all the 45 wavelets used in this study, which five of these wavelets repeated twice. After introducing the Gabor filter here, the feature is extracted from the image of cucumber. Figure 3 shows the general structure of the feature extraction steps of a cucumber image. The image window that is to be decided on its cucumber is first of all balanced by the histogram of the gray surfaces. In the next step, the Fourier transform is multiplied by the Fourier transform of the Gabor wavelets (time-domain convolution). Then the inverse Fourier transform of the 45 images obtained is aligned side by side, making the matrix properties of the desired window. Here, if the rectangular entry window is 60×20, then the properties matrix will be obtained from the Eq. (3) and (4).

(60×20) × 45 = 54000 (4)

Obviously, this number of features (54000) is too high for processing in any classifier and will slow down the detection process. Feature reduction algorithms such as Principal Component Analysis (PCA) can be applied. However, applying this algorithm in a space of its own magnitude is time-consuming. Therefore, considering the processing time, in this study, the dimension matrix dimensionality was reduced by averaging equal blocks and averaging its 3 × 3 blocks. This reduced the attribute matrix to 6000 (60 × 100) layers. In the next step, the matrix is vectored, and then its densities are normalized to the largest dot in absolute magnitude so that all the dots are in the range [-1, +1]. This was done because the maximum and minimum values of the output of the Gabor filter are not specified and in neural network design the constraints between the two values are needed. At this stage, the vector properties of the image window are ready to be referred to the artificial neural network.

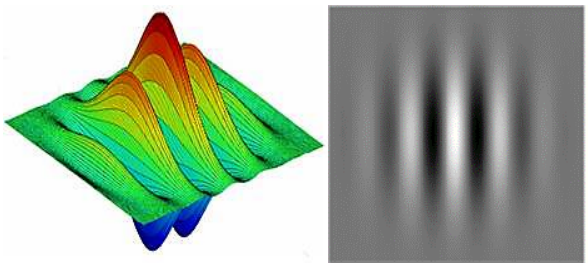

B A

Fig. 2. Gabor wavelet representation as: A) two-dimensional B) three-dimensional

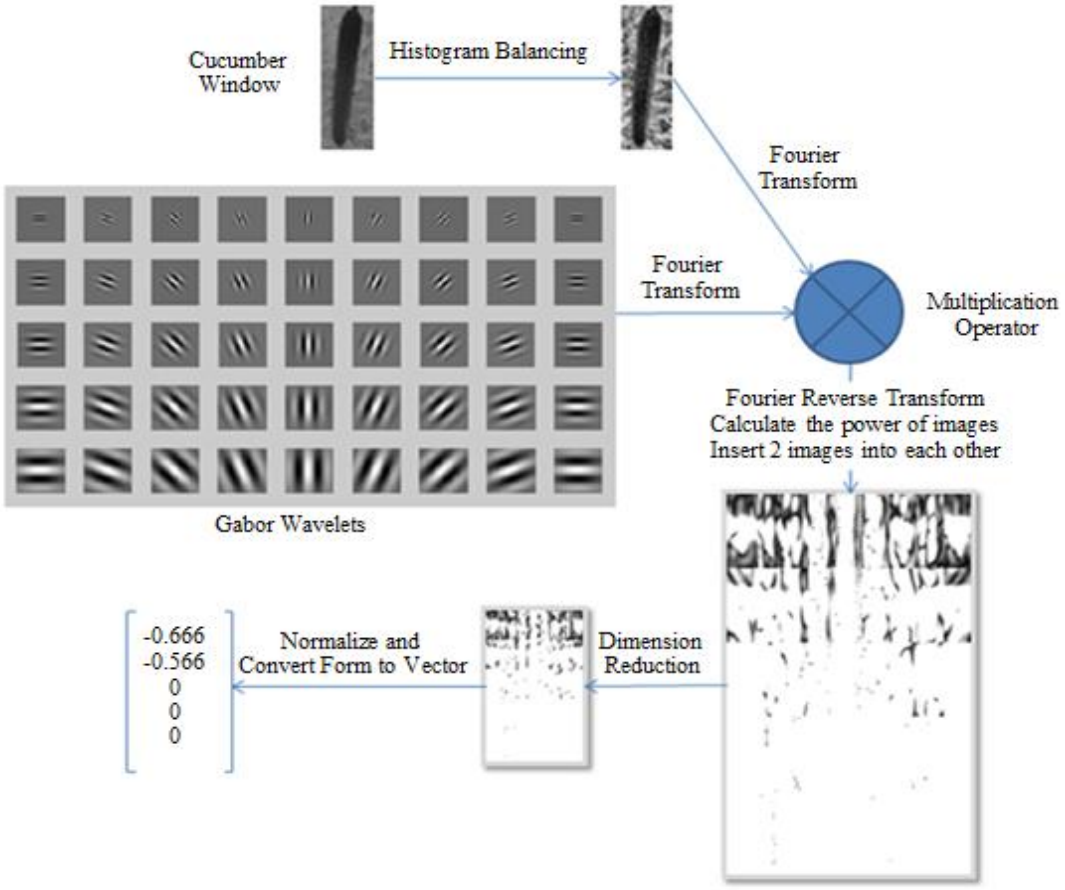

Fig. 3. Feature extraction stages by Gabor filter for a cucumber image

Artificial neural network structure

Classifying the properties of the vector into two classes of cucumber and non-cucumber can be done in a number of methods. One of these methods is the artificial neural network which has been developed in recent years.

Many factors should be considered for selecting and designing the artificial neural network structure. Three prominent examples of these factors are computational volume, response time, and generalizability. Generalizability means that the network has been trained with a limited number of training data, including cucumber and non-cucumber vectors, and it is expected that the network will respond favorably to vectors that have not been previously observed. To improve network response, network structure, training data and extracted features play an important role. Neural networks are subdivided into different types from topological and structural to learning approaches, and each performs well in specific applications. Because no specific method has been devised so far to select the best network to solve a particular problem, this is done experimentally based on experimentation of different networks as well as different network structure and finally the best response.

To select the neural network suitable for the proposed method, four networks including perceptron, feedback propagation, cascade forward propagation and Elman network were simulated. In order to determine the best network for the proposed method, these networks were simulated, trained and tested. All four networks were attempted to simulate as closely as possible the same conditions. They all have two layers. The perceptron, the feedback propagation and the back-

propagation cascade network have 500 neurons in the first layer and 1 neuron in the output layer and the Elman network has 25 neurons in the first layer and 1 neuron in the output layer. The training algorithm for each of the four networks is SCG and the mean squared error with regularization rate is determined 10^{-3} and was trained for up to 200 epochs. All four networks were trained using 24 images of cucumber, 27 non-cucumber images and their optimal response. After training, the four networks were tested with 14 images in identical conditions and their performance was compared.

Perceptron multilayer neural network with error propagation learning method is one of the most commonly used networks, which in this study, after investigating and testing several networks, was considered as the best possible neural network for the proposed method to detect cucumber fruit in greenhouse images. The neural network used is a three-layer perceptron neural network with 320 neurons in the first layer and 160 neurons in the second layer and one neuron in the output layer. The transfer function of each neuron is a tan-sigmoid whose output varies between -1 and +1 as shown in Figure 4.

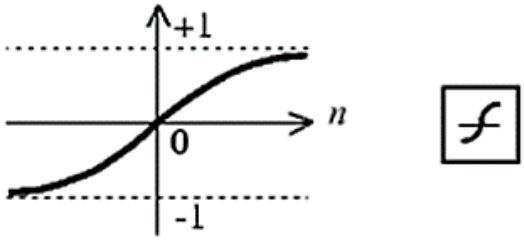

Fig. 4. Tan-sigmoid function

Figure 5 shows the structure of the perceptron network used in this study. It is notable that so far no general rule of thumb about the number of layers and neurons in multilayer neural networks has been recommended and different results can be obtained by changing the structure of the network. In this research, many networks were simulated and tested in terms of combination of number of layers and number of neurons of each layer, among which three combinations were presented that had the best results. These three combinations are:

1- Two layer network with 500 neurons in the first layer and 1 neuron in the output layer.

2- Three layer network with 320 neurons in the first layer, 160 neurons in the second layer and 1 neuron in the third layer.

3- Four-layer network with 300 neurons in the first layer, 100 neurons in the second layer, 20 neurons in the third layer and 1 neuron in the last layer.

The neural network identifies each cucumber with a point that corresponds to the geometric center of the cucumber fruit. This point is the center of the rectangle drawn around the cucumber fruit, and the drawing of this rectangle around the coordinates revealed by the neural network in the processed images is merely to show the result of the processing. Therefore, the output vector of the neural network(Y) includes the coordinates of the geometric center of the rectangles that the neural network has identified as the fruit of the cucumber.

Neural network training

The neural network is trained to minimize the function of the network. Neural networks are divided into supervised and unsupervised education groups. There are several training algorithms for training neural networks in which 5 training methods have been investigated in this study to select one of them for training the network used in the proposed method. These five algorithms are Gradient Descent with Adaptive learning rate (GDA), Gradient Descent back-propagation with

momentum (GDX), Scaled Conjugate Gradient (SCG), Conjugate Gradient Fletcher (CGF) and Conjugate Gradient Polak (CGP) algorithm. The five training algorithms were applied to train an identical perceptron network.

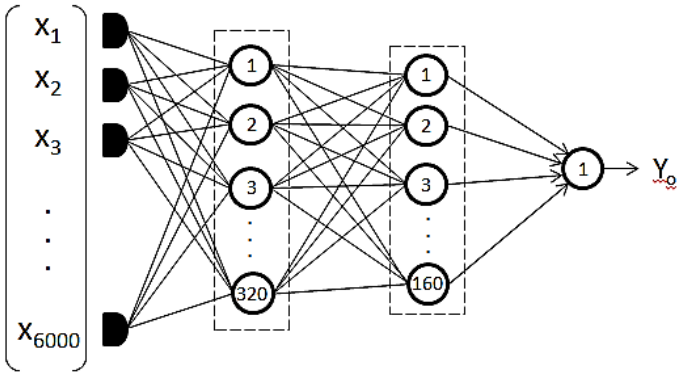

Fig. 5. Perceptron network used in this research (X_i: feature vector, Y: vector containing fruit)

Finally, the network is weighted by the Scaled Conjugate Gradient (SCG) algorithm. The training of the network was that the images of cucumbers with the quality of 20×60×60 as well as the dimensions of the windows were sent individually to the feature extraction unit and then converted to 6000 elements after extraction of the feature. Then a large matrix with each column a feature vector of one of the training images was used to train the network with the optimal response of each column equal to 0.9 for cucumber vectors and -0.9 for non-cucumber vectors. Images of cucumber are easily accessible and produced. The main problem is the selection (not the preparation) of non-cucumber images. It is obvious that these images can be customized, but the network efficiency depends on the selected images. For this purpose, the windows diagnosed as inaccurate in the network test process can be added to the non-educational image set and the training process can be repeated. In this study, 21 cucumbers and 45 non-cucumber images were used in the training phase. Also, for each image of cucumber, its mirror image as well as at angles of 5, 10 and 15 degrees in the positive and negative direction and images with one pixel shift in all four directions were included in the training set to reduce the sensitivity of the network. For non-cucumber images, their mirrors and their 180-degree conversion were included in the training data. The proposed method was simulated by MATLAB software and run on a computer with an Intel Core i3 processor with 2 GB of memory. After simulation of the proposed method, the three-layer perceptron neural network was trained.

Results and Discussion

The three-layer perceptron network is well trained and has a minimal performance function. The results of the training of the four networks are presented in table 1.

Table 1- The results of the training of the four networks

Network	Epoch	Time	Performance
perceptron	61	2' 38"	0.000999
feedback propagation	79	3' 22"	0.000939
cascade forward propagation	132	5' 37"	0.000981
Elman	200	7' 58"	0.0021

The perceptron, the feedback propagation and the cascade forward propagation networks have reached the set performance of 10^{-3}, but the perceptron network has done so with less epochs and a shorter period of time. However since only achieving performance rates is not the determinant of the best network, these four networks need to be tested to determine which network works best. Therefore, in order to select the best network, these four networks have been tested using the proposed method for cucumber fruit detection in 14 identical images, which are presented in table 2.

Table 2- The results of four selected networks test on 14 identical images containing 20 cucumber fruits

Network	Average time (s)	Undetected cucumbers error	Incorrect detection error
Perceptron	12.5	2	1
Feedback propagation	15.46	3	5
Cascade forward propagation	15.84	6	11
Elman	16.11	3	22

In Table 2, the undetected cucumber errors are cucumbers not detected by the network and incorrect detection errors are the points incorrectly identified as cucumbers. As can be seen from the results, the perceptron network performs better than other networks and has less processing time. Therefore, the perceptron network is more suitable than the other networks and it is considered as the base network for the proposed method.

The network trained by the SCG algorithm has reached the minimum performance function (msereg) with less epoch than the other algorithms. This demonstrates the appropriate ability of the SCG algorithm to train the perceptron network to detect cucumber fruit in greenhouse images. After selecting the perceptron network as the most appropriate neural network and the SCG algorithm as the best training algorithm possible for this particular problem, one can now optimize the neural network structure in terms of number of layers and number of neurons per layer.

These three networks were trained after simulation by SCG algorithm with 21 cucumber images and 45 non-cucumber images and up to 100 epochs to reach10^{-4} as msereg and then tested on 14 similar images to choose the best combination of them.

Table 3- Training results of the three proposed Perceptron network

Perceptron network	Epoch	Time	Performance function rate
Two layers	100	3' 56"	0.000443
Three layers	37	1' 38"	0.000804
Four layers	100	2' 38"	0.000230

As shown in Table 3, the proposed three-layer perceptron network performs better than the other two networks and has achieved a set performance function value over a fewer epoch and shorter time. These three networks were tested on 14 identical images after the simulation (Table 4).

Table 4- The results of three proposed perceptron networks on 14 images including 20 cucumber fruits

Perceptron network	Average time(s)	Number of undetected cucumbers	Incorrect detection error
Two layers	12.5	2	1
Three layers	4.57	0	0
Four layers	14.64	2	3

The best results were obtained with a three-layer network with 320 neurons in the first layer, 160 neurons in the second layer, and 1 neuron in the output layer, which showed superiority both in processing time and in accuracy of detection. This detection took an average of 4.57 seconds for each. The shorter processing time is important to increase the efficiency of the cucumber harvesting robot.

After simulating the proposed method and training the three-layer perceptron neural network for the detection of cucumber fruit in the images, the proposed method was tested on 120 images obtained from a greenhouse. These images were taken daily without special lighting systems and under different lighting conditions using a Samsung S1050 camera that has the optical properties suitable to use in greenhouse cucumber harvesting robots. The relevant results are presented in Table 5.

Table 5- Results of the simulated method test

Number of images	Number of cucumbers on images	Number of undetected cucumbers	Incorrect detection error	Average processing time(s)
120	255	12	8	5.12

Incorrect detection error includes locations of the image that were mistaken for cucumber, which was equal to 3.13% (8 cucumbers) in these images. Obviously, these errors are due to the inability of the neural network to correctly classify which can be corrected for network configuration or training process. The undetected error was 4.7% (12 cucumbers) and included locations on the image where the cucumber was present, but was not detected as a cucumber. In other words, the accuracy of the network in correctly identifying the position of the cucumber fruit in the images was 95.3%. This result is consistent with the research of Yuan *et al*. (2008) which corresponds to 40 images including 30 images containing cucumber and 10 images without cucumber taken from a greenhouse environment and reached 83.3% and 100% detection accuracy, respectively. This error can be attributed to the neural network or may not be located in the wrong spots from the beginning. The results showed that most errors were related to inaccurate point's estimation. In other words, some of the cucumbers in the images were not identified as the center of a probable cucumber in the original estimates, in which case the presence or absence of cucumbers was not investigated. Figures 6 and 7 show the three sample images tested by the proposed method, along with the detection results and processing times of each network.

C B A

Fig. 6. Three sampled images for processing by proposed method
(A: 250*188 pixels, B: 175*131 pixels and C: 210*124 pixels)

A B C

Fig. 7. Results of three processed images by proposed method
(Processing time for image A: 13.16 s, image B: 3.65 s and image C: 4.49 s)

Conclusion

In this study, a method was proposed to determine the location of cucumber fruit on greenhouse images for use in greenhouse cucumber harvesting robots. Greenhouse-grown cucumber detection imposes several challenges due to the similar coloration of the fruits and the leaves, stems and flowers; a large number of occlusions, which creates high variability in the apparent shape of the cucumbers; and the random positions and orientations in which fruits can be found. The proposed method was then simulated and tested on 120 images. The proposed method had a low error and was able to detect high levels of cucumber fruit in the images. This detection took an average of 5.12 seconds for each image. Therefore, considering the results of testing this method and also considering the need of the proposed method for specific hardware and the ease of application of this method, it can be concluded that the proposed method can be an efficient method for detecting greenhouse cucumbers on greenhouse pictures. However, preliminary experimental results demonstrate the satisfactory performance of the proposed algorithm and highlight its potential benefits.The results of this study were used to detect fruit in a greenhouse cucumber harvesting robot developed by the authors.

References

1. Bao, G., Cai, S., Qi, L., Xun, Y., Zhang, L., & Yang, Q. (2016). Multi-template matching algorithm for cucumber recognition in natural environment. *Computers and Electronics in Agriculture, 127*, 754-762. https://doi.org/10.1016/j.compag.2016.08.001
2. Fernandes, S., & Bala, J. (2015). Study on MACE Gabor Filters, Gabor Wavelets, DCT-Neural Network, Hybrid Spatial Feature Interdependence Matrix, Fusion Techniques for Face Recognition. *Recent Patents on Engineering, 9*(1), 29-36. https://doi.org/10.2174/2210686303666131118220632
3. Hayashi, S., Ganno, K., Ishii, Y., & Tanaka, I. (2002). Robotic Harvesting System for Eggplants. *Japan Agricultural Research Quarterly: JARQ, 36*(3), 163-168. https://doi.org/10.6090/jarq.36.163
4. Li, D., Zhao, H., Zhao, X., Gao, Q., & Xu, L. (2017). Cucumber detection based on texture and color in greenhouse. *International Journal of Pattern Recognition and Artificial Intelligence, 31*(08), 1754016. https://doi.org/10.1142/S0218001417540167
5. Li, P., Lee, S., & Hsu, H. Y. (2011). Review on fruit harvesting method for potential use of automatic fruit harvesting systems. *Procedia Engineering, 23*, 351-366. https://doi.org/10.1016/j.proeng.2011.11.2514

6. Li, Z., Miao, F., Yang, Z., & Wang, H. (2019). An anthropometric study for the anthropomorphic design of tomato-harvesting robots. *Computers and Electronics in Agriculture, 163*, 104881. https://doi.org/10.1016/j.compag.2019.104881
7. Lin, G., Tang, Y., Zou, X., Xiong, J., & Fang, Y. (2019). Color, depth, and shape-based 3D fruit detection. *Precision Agriculture*. https://doi.org/10.1007/s11119-019-09654-w
8. Liu, X., Zhao, D., Jia, W., Ji, W., Ruan, C., & Sun, Y. (2019). Cucumber Fruits Detection in Greenhouses Based on Instance Segmentation. *IEEE Access, 7*, 139635-139642. https://doi:10.1109/access.2019.2942144
9. Ma, J., Du, K., Zheng, F., Zhang, L., Gong, Z., & Sun, Z. (2018). A recognition method for cucumber diseases using leaf symptom images based on deep convolutional neural network. *Computers and Electronics in Agriculture, 154*, 18-24. https://doi.org/10.1016/j.compag.2018.08.048
10. Mohamadzamani, D., Sajadian, S., & Javidan, S. M. (2020). DDetection of *Callosobruchus maculatus* F. with image processing and artificial neural network. *Applied Entomology and Phytopathology, 88*(1), 103-112. https://doi.org/10.22092/jaep.2020.341684.1324
11. Vakilian, K. A., & Massah, J. (2016). An apple grading system according to European fruit quality standards using Gabor filter and artificial neural networks. Scientific Study & Research. *Chemistry & Chemical Engineering, Biotechnology, Food Industry, 17*(1), 75.
12. Yuan, T., Li, W., Feng, Q., & Zhang. J. (2010). Spectral Imaging for Greenhouse Cucumber Fruit Detection Based on Binocular Stereovision. 2010 Pittsburgh, Pennsylvania. https://doi.org/10.13031/2013.29858
13. Yuan. T., Chen-guang, X., Yong-xin, R., Qing-chun, F., Yu-zhi, T., & Wei, L. (2008). Detecting the Information of Cucumber in Greenhouse for Picking Based on NIR Image. College of Engineering China Agricultural University Beijing 100083. https://doi.org/10.3964/j.issn.1000-0593(2009)08-2054-05
14. Zhao, Y., Gong, L., Huang, Y., & Liu, C. (2016). A review of key techniques of vision-based control for harvesting robot. *Computers and Electronics in Agriculture, 127*, 311-323. https://doi.org/10.1016/j.compag.2016.06.022

نشریه ماشین‌های کشاورزی
https://jame.um.ac.ir

مقاله پژوهشی
جلد ۱۳، شماره ۱، بهار ۱۴۰۲، ص ۳۹-۲۷

شناسایی میوه خیار در تصاویر گیاه به کمک شبکه عصبی مصنوعی

داود محمدزمانی[1*]، سید محمد جاویدان[2]، معین زند[3]، محمد رسولی[4]

تاریخ دریافت: ۱۴۰۰/۰۹/۰۳
تاریخ پذیرش: ۱۴۰۰/۱۲/۰۲

چکیده

در این مطالعه، یک رویکرد شبکه عصبی برای تعیین محل دقیق میوه خیار بر روی تصاویر گلخانه‌ای پیشنهاد شده است. برای این منظور پس از متعادل کردن هیستوگرام روشنایی تصویر مورد نظر، تصویر را با پنجره‌ای حاوی تصویر میوه خیار ضرب می‌کند که باعث می‌شود در مناطق مشکوک به خیار ضرایب بزرگ‌تری به‌دست آید. با استخراج این حداکثرهای محلی، خوشه‌هایی از نقاط اولیه به‌عنوان پنجره‌های احتمالی وجود خیار به‌دست می‌آید. سپس برای تشخیص دقیق محل قرارگیری خیارها، این نقاط و نواحی اطراف آن‌ها به یک شبکه عصبی که با استفاده از تعدادی تصویر شامل تصاویر خیار، تصاویر غیر خیار و پاسخ بهینه آن‌ها آموزش داده شده است، ارجاع داده می‌شود. مناطق به‌دست‌آمده از این شبکه منجر به تشخیص دقیق محل خیارها در تصویر شد. روش پیشنهادی در جعبه ابزار Simulink نرم‌افزار متلب پیاده‌سازی شد. سپس روش پیشنهادی با استفاده از این ساختار شبکه شبیه‌سازی شد و بر روی ۱۲۰ تصویر به‌دست‌آمده از یک گلخانه توسط دوربین دیجیتال آزمایش شد. این روش خطای پایینی داشت و توانست نرخ بالایی را در زمان مناسب میوه‌های خیار در تصاویر کشف‌شده تشخیص دهد.

واژه‌های کلیدی: تشخیص، پردازش تصویر، خیار گلخانه‌ای، شبکه عصبی مصنوعی

۱- استادیار، گروه مهندسی بیوسیستم، دانشگاه آزاد اسلامی واحد تاکستان، تاکستان، ایران
۲- گروه مهندسی بیوسیستم، دانشگاه تربیت مدرس، تهران، ایران
۳- دانش‌آموخته کارشناسی ارشد، گروه مهندسی بیوسیستم، دانشگاه آزاد اسلامی واحد تاکستان، تاکستان، ایران
۴- استادیار، گروه اصلاح نباتات، دانشگاه آزاد اسلامی واحد تاکستان، تاکستان، ایران
(*- نویسنده مسئول: Email: dr.dmzamani@gmail.com)

https://doi.org/10.22067/jam.2022.73827.1077

Journal of Agricultural Machinery

Homepage: https://jame.um.ac.ir

Research Article
Vol. 13, No. 1, 2023, p. 41-53

Cold Plasma: A Novel Pretreatment Method for Drying Canola Seeds: Kinetics Study and Superposition Modeling

F. Osloob[1], M. Moradi[2*], M. Niakousari[3]

1- M.Sc. Graduated, Department of Biosystems Engineering, School of Agriculture, Shiraz University, Shiraz, Iran
2- Associate Professor, Department of Biosystems Engineering, School of Agriculture, Shiraz University, Shiraz, Iran
3- Professor, Department of Food Science and Technology, School of Agriculture, Shiraz University, Shiraz, Iran
(*- Corresponding Author Email: moradih@shirazu.ac.ir)
https://doi.org/10.22067/jam.2022.75630.1096

Received: 03 March 2022
Revised: 07 April 2022
Accepted: 19 April 2022
Available Online: 19 April 2022

How to cite this article:
Osloob, F., Moradi, M., & Niakousari, M. (2023). Cold Plasma: A Novel Pretreatment Method for Drying Canola Seeds: Kinetics Study and Superposition Modeling. *Journal of Agricultural Machinery*, *13*(1): 41-53. https://doi.org/10.22067/jam.2022.75630.1096

Abstract

Accurate investigation of kinetics and development of high-precision seed drying models will help better studying the drying process by identifying effective parameters. Present study investigates the application of cold plasma (CP), as a pretreatment process, in air drying of canola seeds. This may bring about some complication into the drying kinetics investigation. Canola seeds with an initial moisture content of 27.5±1% (dry basis) were exposed to CP for 0, 15, 30, and 60 s prior to fluidization by air at temperatures of 40, 50 and 60°C in a pilot scale fluidized bed heated by a solar panel. The results showed a decreasing trend in drying time from 40 to 60°C. The shortest drying time corresponds to samples dried at 60°C with no CP pretreatment. The longest period however occurred for samples dried at 40°C with 60 s of CP pretreatment. The greatest effect of CP on reducing the drying time was observed at temperatures of 40 and 50°C at the CP exposure time of 15 and 60 s, respectively. A reasonably accurate study of drying kinetics was accomplished using the superposition method. Accordingly, using experimental data, curves correspond to different drying conditions were plotted and in two steps these were shifted to a reference curve to acquire a final drying curve. The curve then was fitted to a second-order equation, and was validated using the experimental data. The correlation coefficients, mean square error and mean absolute error were 0.99, 0.03, and 0.023, respectively.

Keywords: Canola seeds, Mean comparison, Shifted factor, Superposition

Introduction

Drying is a process by which the water in food is reduced by evaporation or sublimation using a heat source with precise and controlled conditions. Drying, while reducing the risk of mold, decreases the final weight of the product and makes the material easier to transport. Canola (*Brassica napus*) is a plant of the nightshade family, annual, allogamy, and one of the most important crops whose seeds are used to produce oil (McVetty & Duncan, 2016). The initial moisture content of canola seeds at the harvesting time is about 25%, which must be dried to prevent spoilage of wet seeds. Today, the use of hybrid methods helps speeding up the drying process. Cold Plasma (CP) is a non-thermal technology that includes gases containing reactive electrons, ions, and neutral species which shown to possess antimicrobial characteristics, change molecular structure, causes physical and chemical changes at the polymer surface, inactivate enzymes, reduce or eliminate toxins (Amin & Ghoran nevis, 2016; Pankaj *et al.*, 2015; Pankaj & Keener, 2018). Food types, shapes, their ingredients and even their moisture content have a significant effect on the efficacy of CP (Li *et al.*, 2019). CP is a promising new technology which has been widely used in food and agriculture and may have the potential to enhance the drying

process, in turn improves the nutritional value of the products. There are small numbers of studies which investigated the influence of pretreatment by CP on the drying kinetics (Zhang *et al.*, 2019).

Modeling the drying process not only ensure achieving an optimum design but also save time and money when scaling up the process. There are theoretical, semi-empirical, and empirical methods in mathematical modeling of the drying process (Ghasemi, Moradi, Karparvarfard, Golmakani, & Khaneghah, 2021; Benseddik, Azzi, Zidoune, & Allaf, 2018). Theoretical models are based on the physical principles of drying such as heat, mass, and momentum transfers. These methods are less accurate and in the majority of cases require fast and expensive computing capabilities due to a large computational processing. Semi-empirical modeling on the other hand may be one of the best methods to describe the drying process. In the semi-empirical technique, we use recognized equations developed by other researchers and for other products. In comparison, the semi-empirical models are more accurate than theoretical ones. However, there are some drawbacks too, as lack of standard models and the use of a specific template has practically made the application of the semi-empirical more difficult for some products. It is well known that highest accuracy might be obtained when applying empirical models (Simha, Mathew, & Ganesapillai, 2016; Benseddik *et al.*, 2018). Among the empirical models, application of the superposition method, in addition to identifying the direct effect of traits, can increase the accuracy of the final model. It was used to explain the drying kinetics of thyme leaves at temperatures of 30, 40, and 50 $^{\circ}$C, and three air velocities of 0.5, 0.8, and 1.2 m s^{-1}. The final curve, obtained using this method was an exponential function of two parameters (temperature and air velocity), with a determination coefficient of 0.996 (Khazaei, Chegini, & Bakhshiani, 2008). In another study, the method of superposition for modeling the drying kinetics of Aloe vera gel slices under different temperatures and air velocities was investigated. The findings showed that the developed model possess acceptable accuracy (Moradi, Niakousari, & Mousavi Khaneghah, 2019).

To the best of our knowledge, no article has been published to incorporate the influence of cold-plasma pretreatment in the modeling of drying process. In order to investigate the effect of CP pretreatment on the drying kinetics of canola seeds, a fluidized bed dryer operating at 3 inlet air temperatures was set up. The seeds were dried with and without CP pretreatment. A model based on the superposition was developed to simulate the drying kinetics of canola seeds.

Materials and Methods

Sample preparation

Fresh canola seeds were harvested from a farm located in faculty of Agriculture of Shiraz University. The initial moisture content of seeds was determined to be 27.5 ±1% (dry basis). The drying in a fluidized bed was carried out using 250 g of fresh seeds. The drying was continued until the average moisture content was around 8% (dry basis).

Dryer

A solar assisted fluidized bed dryer was deployed to investigate the drying kinetics of canola seed (Figure 1). An electric blower (1) (3 phases with a maximum power of 3 kW) was used to blow ambient air on a black galvanized flat plate solar collector (2) with an area of 4 m^2. The air then enters into an auxiliary heating channel (4) which includes an electrical heater (2 kW) after leaving the collector. By adopting a control system, the electrical heater is turned on if the air outlet temperature from the collector is less than the desired drying temperature. The air velocity (6) was adjusted to ensure that the grains are in vibrating motion within the chamber (5) throughout the drying process. Based on the preliminary experiments, the air velocity of 3 m s^{-1} was determined to be suitable. This velocity was used throughout this experimental study. The drying chamber was cylindrical in shape made of transparent

Plexiglas having a diameter and height of 190 and 400 mm, respectively. To adjust the air temperature to the desired value, a thermocouple (type K with an accuracy of 1°C) was installed just before the drying chamber. Fresh canola seeds with an initial moisture content of about 27.5 ±1 % (dry basis) were poured in the drying chamber and was dried to moisture content of 8% (dry basis).

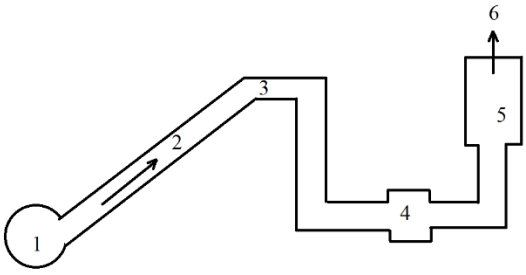

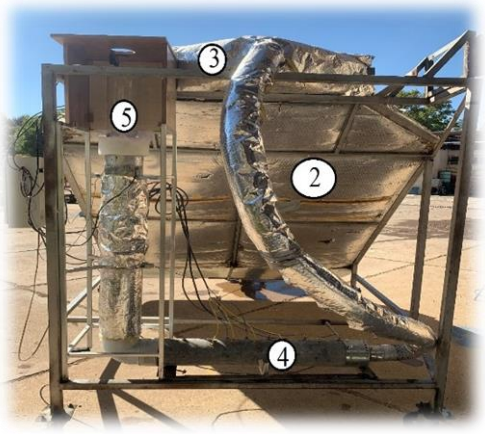

(b)

Fig.1. a) Schematic and b) back view of the solar dryer deployed in the present study
1- Electric blower, 2- Solar collector, 3- Collector outlet, 4- Heating channel, 5- Drying chamber, 6- Air outlet

Cold plasma

The cold plasma device (Nik Plasma Tech Co., Tehran, Iran) was applied for the pretreatment process. The equipment consisted of a generator and a reactor. The reactor consisted of two electrodes and two dielectric plates, an inlet for the flow of selected gas. In the process, after adjusting the generator to desired set up values, fresh canola seeds were spread on a plate between two electrodes in a thin layer manner. It was then exposed to CP for 15, 30 or 60 s, depending on the experiment predetermined times. The unit was operated at a voltage of 11 kV, a frequency of 14 kHz with N_2 gas at pressure of about 1 atm, as the CP gas. The whole process was operated at the atmospheric pressure.

Experimental design

In order to investigate the effect of different operating conditions on the drying time, three levels of air temperature (40, 50 and 60°C) at an air velocity of 3 m s^{-1} were selected. Prior to the drying, the seeds were exposed to 0, 15, 30 or 60 s of nitrogen CP. The procedure was carried out in a completely randomized factorial design. All runs were executed in triplicates and analysis of variance and mean comparison were performed on SPSS 16 software based on the Duncan's test.

Modeling

The superposition (SP) is an empirical method which has relatively high accuracy while being quite simple to be used in a simulation (Cheung, Terekhov, Chen, Agrawal, & Olshausen, 2019). In simulating the drying process by SP, different curves should be shifted to a reference one. To accomplish this, firstly, the moisture ratio during drying time for different drying conditions was obtained using the experimental data. Then, the six standard models in the literature were fitted to the experimental moisture ratio and, the most appropriate one was selected to describe the moisture ratio of canola seeds at one-minute intervals. Thereafter, by selecting a temperature as the reference (in the present work, 50°C), the drying curves for other temperatures (40 or 60°C) were shifted to the reference curve by shift factors. The moisture ratio versus the logarithmic times for each run (with and without CP exposure) for 3

temperatures were plotted (Figs. 6 to 9), and the points with the same values of moisture ratio in the reference curve and the other curve, were identified and shifted by a reduced time factor (D), obtained from equation (1), while shift factor (a) is calculated using equation (2):

$$D = \mathrm{Log}(t_r) - \mathrm{Log}(t_i) \quad (1)$$

$$a = 10^{D} \quad (2)$$

Where the same value of moisture ratio was observed in time of "t_r" on the reference curve (50°C) and in the time of "t_i" on the other curves (40 or 60°C).

Thus, a shifted drying curve was achieved for each CP exposure time. In the next step, as in the previous step, by selecting a CP exposure time (15 s) as the reference and by shift the other drying curves to it, a single drying curve was obtained. Therefore, by two stages of superposition, a final curve was obtained. Multiplying the shift factors, by the drying time at each step was performed to achieve the final reduced time, and using regression analysis, the equation of the final curve was attained as a function of the reduced time. To validate the model, the produced moisture ratios by the superposition model were compared to the experimental moisture ratio.

Results and Discussions

Drying kinetics

Moist canola seeds were harvested with an initial moisture content of 27±1 % (dry basis) from the field. The seeds in a thin layer manner exposed to CP for 0 (no CP exposure), 15, 30 and 60 s prior to drying at 40, 50 and 60°C. The drying air velocity was kept constant at 3 m s^{-1} throughout the experiments. Using analysis of variance, the effect of independent parameters on the drying time was investigated (Table 1).

Table 1- Analysis of variance of the effect of CP pretreatment and air temperature on drying time

Variables	DF	Sum squares	Mean squares	F
T	2	5390.92	2695.46	2343.89**
P	3	9.56	3.20	2.80*
T×P	6	117.95	19.66	17.11**
Error	24	24	1.15	
Total	35	5542.43		

* and **: significant at a level of 5 % and 1 %, respectively.

Accordingly, two factors of temperature (P<0.01) and CP exposure time (P <0.05) and their interaction (P <0.01) have a significant effect on the drying time. Therefore, any alteration in the said mentioned parameters results in change in the drying time. In similar studies, the highly significant effect of the drying temperature on the drying time was reported (Moradi, Azizi, Niakousari, Kamgar, & Khaneghah, 2020; Yousefi, Niakousari, & Moradi, 2013). Other researchers' data indicates the significant effect of CP on the drying rate when drying wolfberry and corn kernels (Zhou *et al.*, 2020; Li *et al.*, 2019).

Means comparison

The mean values of the drying time for different drying modes are given in Fig. 2. Accordingly, with increasing the drying air temperature, the drying time was decreased. When drying at 40°C, CP pretreatment (15 s) was applied, the drying time was reduced by 3% in comparison with runs with no CP pretreatment. On the contrary, at longer CP exposure (30 and 60 s), to our surprise the drying time increased by 0.5 and 4.6%, respectively, in comparison to samples which did not experienced CP. Thus, at lower temperature range, the influence of longer duration of CP is negative in term of drying time; i.e. the optimum CP exposure time is 15 s. In another study, the effect of CP in four exposer times of 15, 30, 45, and 60 s on the drying time of red pepper at a constant temperature of 70°C and air velocity of 6 m s^{-1}, was investigated. The optimum exposure time

of 30s was reported to give rise to the lowest drying time (Zhang *et al.*, 2019). At air temperature of 50°C, increasing CP exposure duration from 15 to 60 s, lead to decrease in the drying time from about 3% to over 12%, compared to no CP exposure. Here, we observed the positive trends in effect of CP pretreatment on drying time. Drying at 60°C; we observe a negative effect of exposure to CP. The drying time went up between 10-16% as the seeds were pretreated between 15 and 60 s by CP. Hence, when drying at 60°C, we would be better off not to exposed the canola seeds prior to the air drying. CP applied on the surface of the drying material, creates small cracks in the cell wall. This is good for water release from the seeds; but increasing the exposure duration may lead to cell wall destruction and loss of porosity which in turn reduces the water vapor evaporation from the seed's surface (Zhang *et al.*, 2019). Similar adverse effect may be the reason for this discrepancy in the trend of drying time while drying canola seeds.

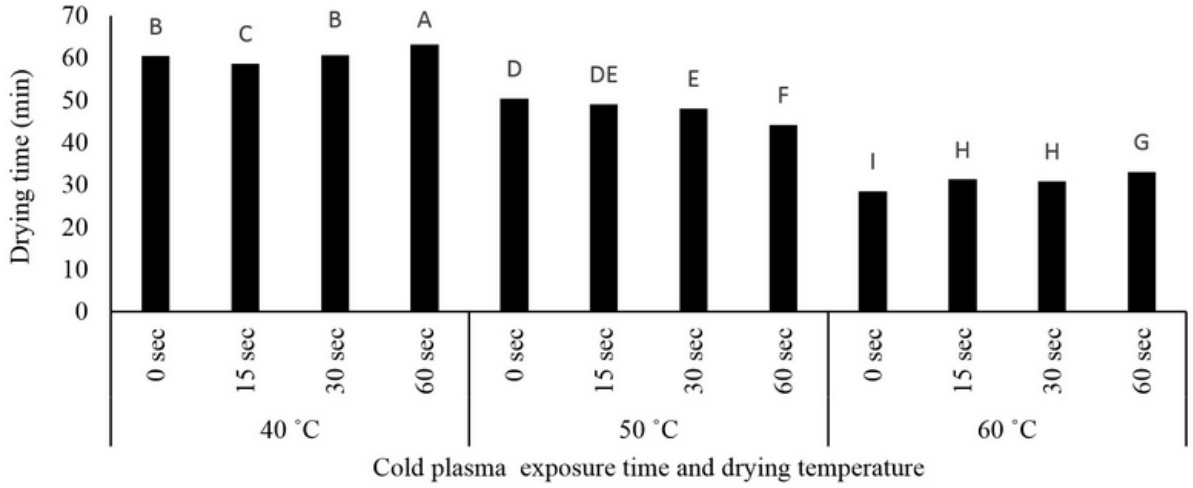

Fig. 2. Mean drying time for different drying conditions with or without pretreatment by CP

Figures 3, 4, and 5 show the changes in the moisture ratio versus the drying time for temperatures of 40, 50, and 60°C, respectively. Accordingly, the best pretreatment of CP in the temperatures of 40, 50, and 60°C, were 15, 60, and 0 s, respectively. The reason for the change in CP behavior with the change in drying air temperature may be related to the effect of temperature on the seed shell microstructure under the influence of CP pretreatment. Probably, CP produces some sort of case hardening on the surface of the seeds hence moisture cannot easily exit the seeds surface. This may be attributed to the nature of CP being an amalgam of various particles. Another reason could be the drying effect of CP gas on seeds as the exposure duration is increased.

In another study, a CP air with ambient pressure and flow of 3 L min^{-1} and frequency of 20 kHz and power consumption of 750 W was used as a pretreatment of drying of red pepper. Red pepper samples were exposed to CP in four different time treatments (15, 30, 45, and 60 s). In all-time conditions, drying time was significantly reduced compared to the control treatment that did not use CP pretreatment. However, the greatest reduction in drying time was associated with a CP time of 30 s (Zhang *et al.*, 2019).

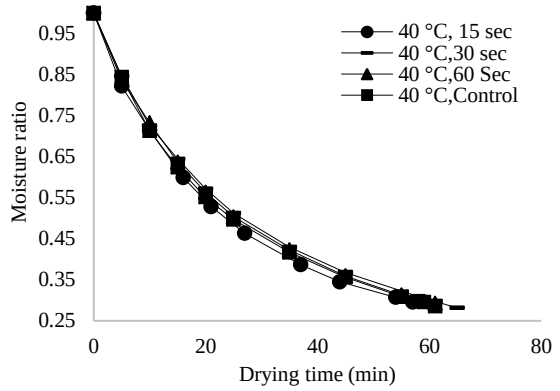

Fig. 3. Variations of moisture ratio versus drying time for drying temperature of 40°C

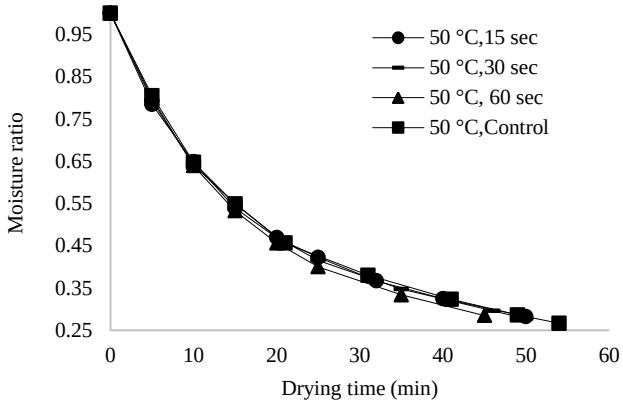

Fig. 4. Variations of moisture ratio versus drying time for drying temperature of 50°C

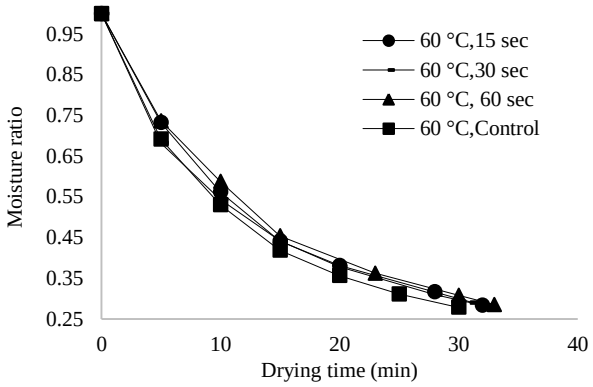

Fig. 5. Variations of moisture ratio versus drying time for drying temperature of 60°C

In another study, the cooking time in half of rice was reduced after the application of CP. In that research, after CP pretreatment, cracks and depressions were observed on the surface of rice grain (Sarangapani, Devi, Thirundas, Annapure, & Deshmukh, 2015). Increasing the exposure time to the CP can potentially lead to the formation of larger diameter cavities and thus reduce the drying time (Nishime *et al.*, 2017). However, the drying time cannot be less than a certain amount, and with increasing CP time, cell wall disruption may occur; resulting in a reduced porosity and increased resistance to moisture movement within the material (Saengrayap, Tansakul, & Mittal, 2015). Jujube slices were dried at three temperatures of 50, 60, and 70°C with (15, 30 and 60s) or without CP pretreatment. The results showed that the interaction between the plasma pretreatment time and the drying

temperature was significant so that at the temperature of 50°C the usage of CP pretreatments showed less effect on the drying time than the control treatment (no CP pretreatment). While the use of drying temperatures of 60, and 70°C with a cold plasma pretreatment of 15 s showed the greatest effect in reducing the drying time. However, with increasing the CP pretreatment time to 30 and 60 s, it was observed that the drying time was increased (Bao, Hao, Shishir, Karim, & Chen, 2021).

Developing a model based on superposition

In order to obtain the superposition model, at first, the moisture ratio of canola seeds should be determined during drying time. Therefore, standard semi-empirical models developed by the previous researchers, were used and the most appropriate model was selected based on the correlation between the seed moisture ratio predicted by the models and those obtained from the experimental results (Table 2).

Table 2- Coefficients of standard models and their correlation with experimental results

Model name	Model Coefficients	R^2	RMSE	X^2	MAE
Page	K=0.0464, n=0.8490	0.90	0.0864	0.0075	0.0628
Newton	K=0.0302	0.88	0.0966	0.00949	0.0759
Modified page	K=0.0269, n=0.849	0.90	0.0863	0.00758	0.0628
Henderson and Pabis	K=0.0291, a=0.9834	0.87	0.0944	0.0090	0.0749
Logarithmic	K=0.0449, a=0.7534	0.86	0.0999	0.0101	0.0655
Two term	a=0.5686, k_0=0.0115, b=0.4333, k_1=0.0726	0.92	0.086	0.0075	0.0595

K, n, a, k_0, and k_1 are model coefficients. Since Two term model, has a higher correlation coefficient and a lower error coefficient, it was selected as the most suitable model to predict the instantaneous moisture ratio of the canola seeds. In another study, the drying of rice paddy grains in a fluidized bed dryer was simulated using the above standard models. The results indicate that Midilli model was best fitted to the experimental data (Khanali, Rafiee, Jafari Hashemabadi, & Banisharif, 2012). Therefore, in the present study, to determine the sum of drying effects, the moisture ratio of canola seeds at one-minute intervals was predicted using Two term model. The variations of moisture ratio against the logarithmic time were obtained and plotted for different experiments (Figs. 6 to 9).

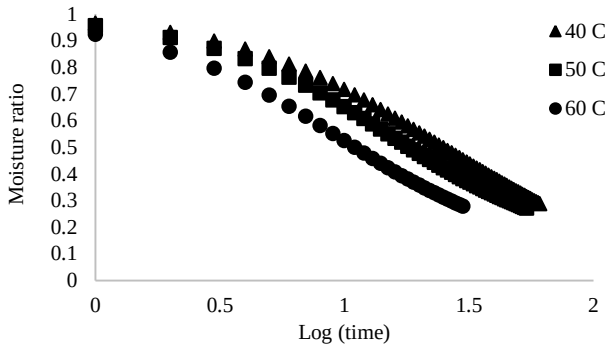

Fig. 6. Moisture ratios versus Log (time) for control experiments (no CP treatment) at different temperatures

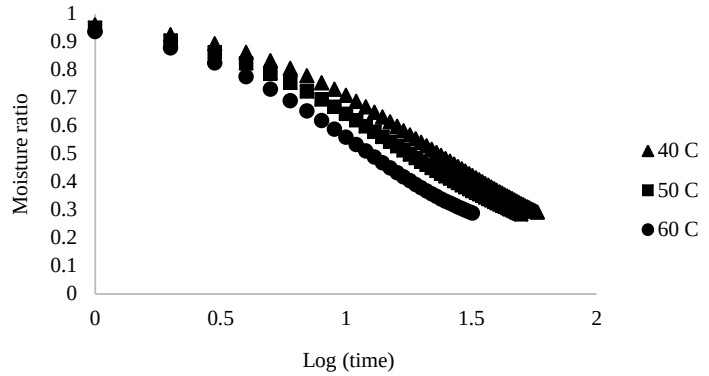

Fig. 7. Moisture ratios versus Log (time) for experiments (15 s CP treatment) at different temperatures

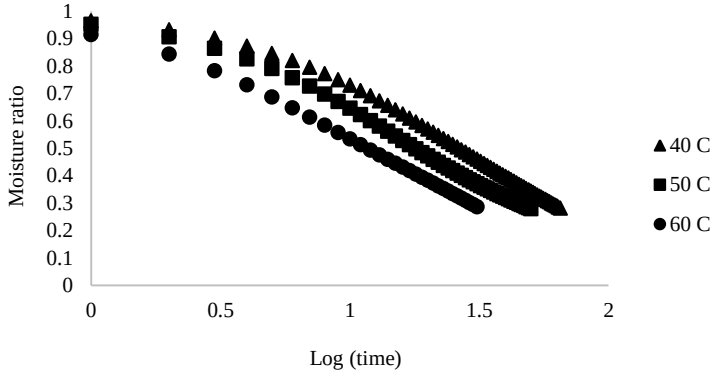

Fig. 8. Moisture ratios versus Log (time) for experiments (30 s CP treatment) at different temperatures

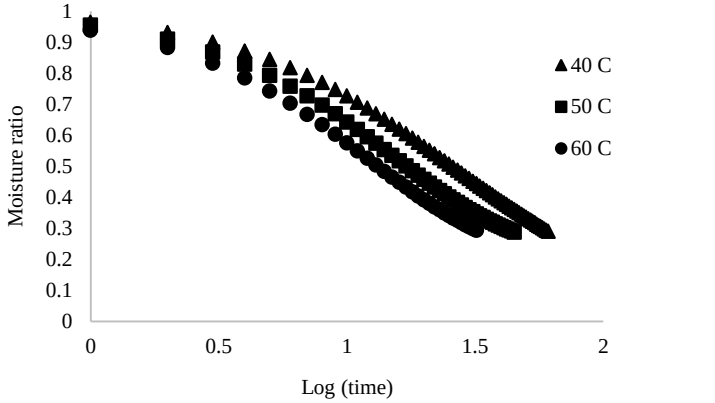

Fig. 9. Moisture ratios versus Log (time) for experiments (60 s CP treatment) at different temperatures

As there are two independent parameters, namely temperature and CP duration, the transfer process ought to be materialized in two stages in order to med to generate a final drying curve. Hence, in the first stage, in figures 6-9, points with the same value of moisture ratio were identified, and by application of equations (1) and (2),

temperature shift factors (aT) were calculated (Table 3). Afterwards, in each CP duration, by shifting the curves with temperatures 40 and 60°C to the reference curve (50°C), four shifted curves were obtained. For the second transfer stage, in those curves, points with the same moisture ratio values were identified, and CP time shift factors (aP) were calculated using Equations (1) and (2) (Table 3). Here, 15s CP exposure time was designated as the reference curve and the other three curves (0, 30, and 60 s CP treatment) were shifted to this curve using the aP and the final drying curve was obtained (Fig. 10). "aT" for the experiments at 40°C is smaller and at 60°C is greater than one. This is an indication that drying time for 40°C is longer and 60°C is shorter compared to 50°C. For 40°C, the greatest "aT" value of 0.78 is observed when the CP exposure time was 15 s. This indicates a shorter drying time in comparison with other plasma modes is at 40°C. When setting the air temperature to 50°C, at longer exposure time of seeds by CP, the aP is increased to the highest value of 1.031 at the CP exposure time of 60 s. Bearing in mind that the highest value of "aT" at 60°C corresponds to 0 exposure duration (The control runs). Therefore, it is shown that the shortest drying time at 60°C is when the seeds are not exposed to the cold plasma prior to hot air drying process. These interesting findings reveals that the results obtained in the superposition model are in good agreement with those acquired in the experimental works which presented and discussed in the previous section.

Table 3- Shift factors at different plasma times and temperatures

T (°C)	P (sec)	aT	aP
40	0	0.753	0.931
50	0	1.000	0.931
60	0	1.659	0.931
40	15	**0.780**	1.000
50	15	1.000	1.000
60	15	1.480	1.000
40	30	0.698	0.991
50	30	1.000	0.991
60	30	1.548	0.991
40	60	0.693	1.031
50	60	1.000	**1.031**
60	60	1.330	1.031

Based on Figure 10, the final curve obtained from the shifting of 12 different curves, can accurately predict the moisture ratio with a quadratic equation (Equation 3).

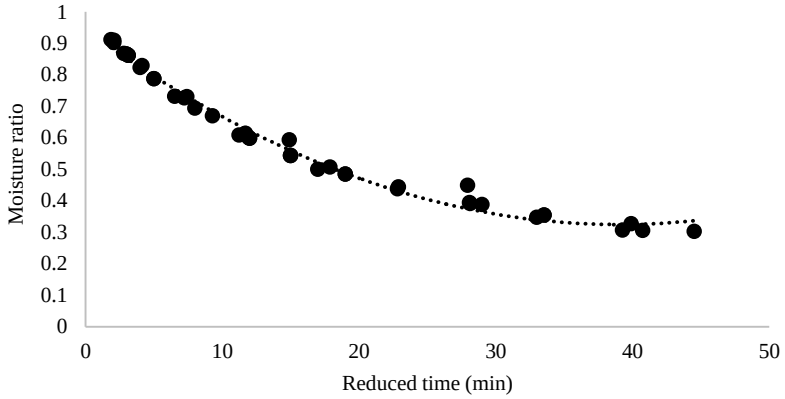

Fig. 10. Final shifted curve with the polynomial regression equation

$MR = 0 \cdot 0004\, t'^2 - 0 \cdot 0318\, t' + 0 \cdot 9441 \qquad R^2 = 0 \cdot 988$ (3)

Where t' is the reduced time, obtained from Equation (4):

$t' = t \times aT \times aP$ (4)

That "t" is the actual drying time. Thus, in order to simulate the moisture ratio of the drying product, at first, the reduced time should be calculated using Equation (4) and the amounts of "aT" and "aP" given in the Table 3. Then, moisture ratio can be obtained using Equation (3).

Evaluation of model

Using Equation (3), all the moisture ratios of different experiments were obtained and the results were plotted against the actual moisture ratios obtained by the experiment (Figure 11).

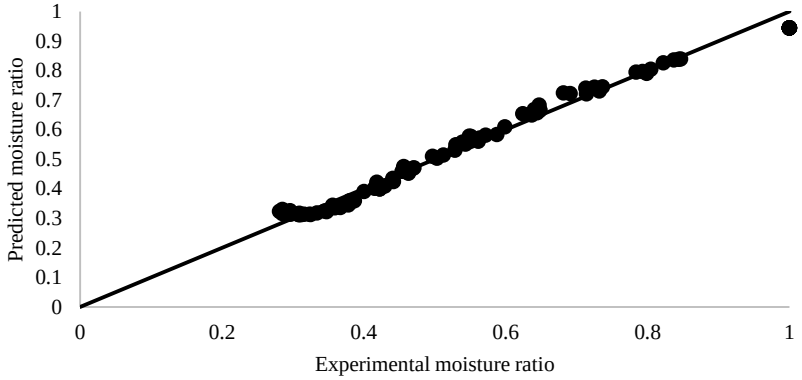

Fig. 11. Comparison between experimental and predicted moisture ratio

Accordingly, good agreement between predicted and measured moisture ratio was observed. The mean absolute error (MAE), k^2, and R^2 were 0.022, 0.0009, and 0.98, respectively. These are indications that the developed superposition model accurately predicts the drying kinetics of canola seed pretreated with CP. Simulation of drying of Aloe vera gel slices in a cabinet dryer with two drying modes of with and without osmotic pretreatment was performed using the superposition method. The results showed that the final model has a good accuracy compared to the other theoretical and semi-empirical methods (Moradi *et al.*, 2019). In another study, modeling of drying thyme leaves in a cabinet dryer was performed using the superposition technique and its results revealed the final model has a good correlation with the experimental results (Khazaei *et al.*, 2008). In another study, the Guava drying process was simulated using the Midilli-Kucuk model and the superposition model. The results showed that the second-order equation of superposition can predict simulation with great accuracy (Kek, Chin, & Yusof, 2014). Therefore, the method of superposition, which is generally used to simulate processes in engineering, in comparison with the other modeling methods, in addition to very high accuracy, has a very little modeling time and cost (Wang & Sharma, 2018). Such models have a very high power and validity in predicting existing processes in engineering (Wang, Yi, & Sharma, 2018). The superposition method can help the final design of the device by separating the effect of independent parameters on the dependent one. As can be concluded in the present study, the effect of CP and temperature on the drying kinetics can be seen in full detail.

Conclusion

A fluidized bed dryer was employed to investigate the effect of cold plasma pretreatment on the drying kinetics of canola seeds. In the experiment, canola seeds were dried at 40, 50 and 60°C following exposure to 0, 15, 30 and 60 s of CP. The shortest drying time of less than 30 min was accomplished

when drying seeds at 60°C without exposure to CP.

Also, the shortest drying time for the temperature of 40 and 50°C was at the CP exposure time of 15 and 60 s, respectively. However, further investigation is required to examine the effect of CP on other properties of dried canola seeds. The superposition technique used to simulate the drying process offered the simplicity as well as reasonably good accuracy. It exhibits the influence of each independent variable on the drying time. The developed model accurately predicted the time in seeds drying with different CP exposure time. Thus using an empirical model, we can investigate the effect of independent parameters of temperature and CP exposure time in full detail.

Acknowledgment

We gratefully acknowledge the financial support of the Research Affairs Office at Shiraz University to support the cost of the conducted experiments (Grant # 99GCB1M215809).

References

1. Amini, M., & Ghoranneviss, M. (2016). Effects of cold plasma treatment on antioxidants activity, phenolic contents and shelf life of fresh and dried walnut (*Juglans regia* L.) cultivars during storage. *LWT- Food Science and Technology, 73*, 178-184. https://doi.org/10.1016/j.lwt.2016.06.014
2. Bao, T., Hao, X., Shishir, M. R. I., Karim, N., & Chen, W. (2021). Cold plasma: An emerging pretreatment technology for the drying of jujube slices. *Food Chemistry, 337*, 127783. https://doi.org/10.1016/j.foodchem.2020.127783
3. Benseddik, A., Azzi, A., Zidoune, M. N., & Allaf, K. (2018). Mathematical empirical models of thin-layer airflow drying kinetics of pumpkin slice. *Engineering in Agriculture, Environment and Food, 11*(4), 220-231. https://doi.org/10.1016/j.eaef.2018.07.003
4. Cheung, B., Terekhov, A., Chen, Y., Agrawal, P., & Olshausen, B. (2019). Superposition of many models into one. *arXiv preprint arXiv*, 1902.05522.
5. Ghasemi, J., Moradi, M., Karparvarfard, S. H., Golmakani, M. T., & Khaneghah, A. M. (2021). Thin layer drying kinetics of lemon verbena leaves: a quality assessment and mathematical modeling. *Quality Assurance and Safety of Crops & Foods, 13*(1), 59-72. https://doi.org/10.15586/qas.v13i1.835
6. Kek, S. P., Chin, N. L., & Yusof, Y. A. (2014). Simultaneous time-temperature-thickness superposition theoretical and statistical modeling of convective drying of guava. *Journal of Food Science and Technology*, *51*(12), 3609-3622. https://doi.org/10.1007/s13197-013-0923-0
7. Khanali, M., Rafiee, Sh., Jafari A., Hashemabadi, S. H., & Banisharif, A. (2012). Mathematical modeling of fluidized bed drying of rough rice (*Oryza sativa* L.) grain. *Journal of Agricultural Technology*, *8*(3), 795-810.
8. Khazaei, J., Chegini, G. R., & Bakhshiani, M. (2008). A novel alternative method for modeling the effects of air temperature and slice thickness on quality and drying kinetics of tomato slices: Superposition technique. *Drying Technology*, *26*, 759-775. https://doi.org/10.1080/07373930802046427
9. Li, S., Chen, S., Han, F., Xv, Y., Sun, H., Ma, Z., ... & Wu, W. (2019). Development and Optimization of Cold Plasma Pretreatment for Drying on Corn Kernels. *Journal of Food Science, 84*(8), 2181-2189. https://doi.org/10.1111/1750-3841.14708
10. McVetty, P. B. E., & Duncan, R. W. (2016). *Canola/Rapeseed: Genetics and Breeding*. In Reference Module in Food Science; Elsevier: Amsterdam, the Netherlands.
11. Moradi, M., Niakousari, M., & Mousavi Khaneghah, A. (2019). Kinetics and mathematical modeling of thin layer drying of osmo-treated Aloe vera (*Aloe barbadensis*) gel slices. *Journal of Food Process Engineering*, *42*(6), e13180. https://doi.org/10.1111/jfpe.13180

12. Moradi, M., Azizi, S., Niakousari, M., Kamgar, S., & Khaneghah, A. M. (2020). Drying of green bell pepper slices using an IR-assisted Spouted Bed Dryer: An assessment of drying kinetics and energy consumption. *Innovative Food Science & Emerging Technologies, 60*, 102280. https://doi.org/10.1016/j.ifset.2019.102280
13. Nishime, T. M. C., Borges, A. C., Koga-Ito, C. Y., Machida, M., Hein, L. R. O., & Kostov, K. G. (2017). Non-thermal atmospheric pressure plasma jet applied to inactivation of different microorganisms. *Surface and Coatings Technology, 312*, 19-24. https://doi.org/10.1016/j.surfcoat.2016.07.076
14. Pankaj, S. K., Bueno-Ferrer, C., Misra, N. N., O'Neill, L., Tiwari, B. K., Bourke, P., & Cullen, P. J. (2015). Dielectric barrier discharge atmospheric air plasma treatment of high amylose corn starch films. *LWT-Food Science and Technology, 63*(2), 1076-1082. https://doi.org/10.1016/j.lwt.2015.04.027
15. Pankaj, S. K., & Keener, K. M. (2018). *Cold plasma processing of fruit juices*. In Fruit juices (pp. 529-537). Academic Press. https://doi.org/10.1016/B978-0-12-802230-6.00026-6
16. Sarangapani, C., Devi, Y., Thirundas, R., Annapure, U. S., & Deshmukh, R. R. (2015). Effect of low-pressure plasma on physico-chemical properties of parboiled rice. *LWT- Food Science and Technology, 63*, 452-460. https://doi.org/10.1016/j.lwt.2015.03.026
17. Simha, P., Mathew, M., & Ganesapillai, M. (2016). Empirical modeling of drying kinetics and microwave assisted extraction of bioactive compounds from Adathoda vasica and Cymbopogon citratus. *Alexandria Engineering Journal, 55*(1), 141-150. https://doi.org/10.1016/j.aej.2015.12.020
18. Saengrayap, R., Tansakul, A., & Mittal, G. (2015). Effect of far-infrared radiation assisted microwave-vacuum drying on drying characteristics and quality of red chili. *Journal of Food Science and Technology, 52*(5), 2610-2621. https://doi.org/10.1007/s13197-014-1352-4
19. Yousefi, A., Niakousari, M., & Moradi, M. (2013). Microwave assisted hot air drying of papaya (*Carica papaya* L.) pretreated in osmotic solution. *African Journal of Agricultural Research, 8*(25), 3229-3235. https://doi.org/10.5897/AJAR12.180
20. Wang, H., Yi, S., & Sharma, M. M. (2018). A computationally efficient approach to modeling contact problems and fracture closure using superposition method. *Theoretical and Applied Fracture Mechanics, 93*, 276-287. https://doi.org/10.1016/j.tafmec.2017.09.009
21. Wang, Y., Guo, P., Dai, F., Li, X., Zhao, Y., & Liu, Y. (2018). Behavior and modeling of fiber-reinforced clay under triaxial compression by combining the superposition method with the energy-based homogenization technique. *International Journal of Geomechanics, 18*(12), 04018172.
22. Zhang, X. L., Zhong, C. S., Mujumdar, A. S., Yang, X. H., Deng, L. Z., Wang, J., & Xiao, H. W. (2019). Cold plasma pretreatment enhances drying kinetics and quality attributes of chili pepper (*Capsicum annuum* L.). *Journal of Food Engineering, 241*, 51-57. https://doi.org/10.1016/j.jfoodeng.2018.08.002
23. Zhou, Y. H., Vidyarthi, S. K., Zhong, C. S., Zheng, Z. A., An, Y., Wang, J., ... & Xiao, H. W. (2020). Cold plasma enhances drying and color, rehydration ratio and polyphenols of wolfberry via microstructure and ultrastructure alteration. *LWT- Food Science and Technology, 134*, 110173. https://doi.org/10.1016/j.lwt.2020.110173

نشریه ماشین‌های کشاورزی
https://jame.um.ac.ir

مقاله پژوهشی
جلد ۱۳، شماره ۱، بهار ۱۴۰۲، ص ۵۳-۴۱

پلاسمای سرد: یک روش پیش‌تیمار جدید برای خشک کردن دانه‌های کلزا: مطالعه سینتیک و مدل‌سازی جمع آثار

فاطمه اسلوب[۱]، مهدی مرادی[۲*]، مهرداد نیاکوثری[۳]

تاریخ دریافت: ۱۴۰۰/۱۲/۱۲
تاریخ پذیرش: ۱۴۰۱/۰۱/۳۰

چکیده

بررسی دقیق سینتیک و توسعه مدل‌های خشک‌کردن با دقت بالا با شناسایی پارامترهای موثر به مطالعه بهتر فرآیند خشک‌کردن کمک می‌کند. تحقیق حاضر به بررسی کاربرد پلاسمای سرد (CP) به‌عنوان یک فرآیند پیش‌تیمار، برای خشک‌کردن بذر کلزا با هوای گرم‌شده می‌پردازد. این پدیده ممکن است باعث ایجاد پیچیدگی‌هایی در بررسی سینتیک خشک‌کردن شود. دانه‌های کلزا با رطوبت اولیه ۱±۲۷/۵ درصد (بر اساس خشک) ابتدا تحت زمان‌های صفر، ۱۵، ۳۰ و ۶۰ ثانیه در معرض CP قرار گرفته و سپس در خشک‌کن بستر سیال که گرمای آن توسط یک جمع‌کننده خورشیدی تامین می‌شود، در دماهای ۴۰، ۵۰ و ۶۰ درجه سلسیوس خشک شد. نتایج به‌دست‌آمده حاکی از روند کاهشی زمان خشک‌شدن از ۴۰ تا ۶۰ درجه سلسیوس بود. کوتاه‌ترین زمان خشک‌شدن مربوط به نمونه‌هایی است که در دمای ۶۰ درجه سلسیوس بدون پیش‌تیمار CP خشک شده‌اند. با این حال، طولانی‌ترین دوره برای نمونه‌های خشک‌شده در دمای ۴۰ درجه سلسیوس با پیش‌تیمار CP ۶۰ ثانیه رخ داد. همچنین بیشترین تاثیر پلاسمای سرد بر کاهش زمان خشک کردن در دماهای ۴۰ و ۵۰ درجه سلسیوس به‌ترتیب با پیش‌تیمارCP ۱۵ و ۶۰ ثانیه مشاهده شد. مطالعه دقیق سینتیک خشک‌کردن با استفاده از روش جمع آثار انجام گرفت. بر این اساس، با استفاده از داده‌های تجربی، منحنی‌های مربوط به شرایط مختلف خشک‌کردن رسم شده و در دو مرحله به منحنی مرجع انتقال داده شدند تا منحنی خشک‌کردن نهایی به‌دست آید. سپس منحنی به یک معادله مرتبه دوم برازش داده شده و با استفاده از داده‌های تجربی اعتبارسنجی انجام گرفت. ضرایب همبستگی، میانگین مربعات خطا و میانگین خطای مطلق به‌ترتیب ۰/۹۹، ۰/۰۳ و ۰/۰۲۳ بودند.

واژه‌های کلیدی: دانه کلزا، جمع آثار، ضریب انتقال، مقایسه میانگین

۱- دانش‌آموخته کارشناسی ارشد، بخش مهندسی بیوسیستم، دانشکده کشاورزی، دانشگاه شیراز، شیراز، ایران
۲- دانشیار، بخش مهندسی بیوسیستم، دانشکده کشاورزی، دانشگاه شیراز، شیراز، ایران
۳- استاد، بخش مهندسی صنایع غذایی، دانشکده کشاورزی، دانشگاه شیراز، شیراز، ایران
(*- نویسنده مسئول: Email: moradih@shirazu.ac.ir)

https://doi.org/10.22067/jam.2022.75630.1096

Journal of Agricultural Machinery

Homepage: https://jame.um.ac.ir

Research Article
Vol. 13, No. 1, 2023, p. 55-66

Mass and Volume Determination of Orange Fruit using Ultrasonic Sensors

H. Masoudi[1*]

1- Assistant Professor, Department of Biosystems Engineering, Faculty of Agriculture, Shahid Chamran University of Ahvaz, Ahvaz, Iran
(*- Corresponding Author Email: hmasoudi@scu.ac.ir)
https://doi.org/10.22067/jam.2022.76674.1106

Received: 13 May 2022
Revised: 03 November 2022
Accepted: 08 November 2022
Available Online: 08 November 2022

How to cite this article:
Masoudi, H. (2023). Mass and Volume Determination of Orange Fruit using Ultrasonic Sensors. *Journal of Agricultural Machinery*, *13*(1): 55-66.
https://doi.org/10.22067/jam.2022.76674.1106

Abstract

In this study, an electronic system was built to determine the mass and volume of orange fruits from their dimensions using ultrasonic sensors. The system hardware parts include a metal box, three ultrasonic sensors, a load-cell sensor, an Arduino board, a memory card module, a voltage converter, a keypad, a display and a power adapter. A computer program was written to obtain data from ultrasonic sensors and determine the mass and volume of fruits using regression relationships in Arduino software. 100 samples of orange fruits (Dezful local variety) were picked randomly from a garden and various measurements were done to determine the main physical properties of fruits including three dimensions, mass (M), and volume (V). The system output values for mass and volume of orange fruits with their actual values had no significant difference at 1% probability level. The root mean square error (RMSE) in determining the oranges mass and volume by the system were 9.02 g and 10.90 cm^3, respectively. In general, the proposed system performance was acceptable and it can be used for determining the mass and volume of orange fruits.

Keywords: Electronic system, Hardware parts, Orange Fruit, Regression modeling, Volume and mass determination

Introduction

A large amount of orange fruits (*Citrus sinensis*) produced in Iran are lost (15-20%) due to lack of proper processing and storage conditions (Ahmadi, Ebadzade, Hatami, Hoseinpoor, & Abdeshah, 2020). While, it is possible to prevent the waste of this useful crop with suitable grading, packaging, and storage. Fruits can be graded based on various parameters such as size, colour, volume, and mass (Vivek Venkatesh, Iqbal, Gopal, & Ganesan, 2015). The speed of automatic machines grading is faster than manual grading. High cost of the automatic machines is the main obstacle to use them (Dağtekin & Beyaz, 2017). Therefore, using appropriate techniques for cheap and rapid measurement of fruits mass and volume can play an important role in developing automatic grading systems and reducing orange fruits losses (Mir-Ahmadi, Mireei, Sadeghi, & Hemmat, 2016).

Various methods such as water displacement method (WDM), digital scales, density grading tubes, aerial comparison pycnometer, and radiation have been used to determine the volume and mass of agricultural products (Mohsenin, 1986; Kachariya, Vasaniya, Dhameliya, & Savant, 2015). These methods are usually time consuming and cannot be done automatically. Today, some systems equipped with electronic tools are used for the rapid weighing of agricultural products (Mir-Ahmadi *et al.*, 2016). Also, indirect and non-destructive methods, and using machine vision and various sensors have been considered by many researchers to

determine the mass and volume of agricultural products (Concha-meyer, Eifert, Wang, & Sanglay, 2018; Yildiz, Özdemir, & Uluişik, 2019). According to the literatures, the image processing technique is effective for grading of the citrus fruits (Omid, Khojastehnazhand, & Tabatabaeefar, 2010; Fellegari & Navid, 2011; Raj Gokul, Raj, & Suriyamoorthi, 2015) and can be considered as a potential replacement to manual sorting (Vivek Venkatesh *et al.*, 2015); But the vision systems are very expensive, complex, and do not work in every lighting conditions. So, developing new techniques for fruits volume estimation to overcome problems like cost and accuracy is essential (Kachariya *et al.*, 2015). Replacing vision cameras with ultrasonic sensors can reduce the cost of fruits grading system and lead to grading in various lighting conditions. The ultrasonic sensors are more useful for determining distance in different lighting conditions compared to vision sensors (Dağtekin & Beyaz, 2017).

The objective of this study was to use electronic system that can determine the mass and volume of citrus fruits such as oranges from their dimensions using ultrasonic sensors, so that this technique can be used to determine the mass and volume of citrus fruits for online grading purposes.

Materials and Methods

In this study, 100 samples of orange fruits (Dezful local variety) were picked randomly from a garden and were transferred to the laboratory. Then, various measurements were employed to determine the main physical properties of fruits including three dimensions, mass (M), and volume (V) at temperature of 17 to 22 °C and relative humidity of 53 to 73%. The oranges dimensions including height (h), width (w) and thickness (t) were determined in three directions perpendicular to each other using a calliper with 0.05 mm accuracy. The oranges mass was determined using a digital scale with accuracy of 0.01 g. The WDM was used to determine the volume of fruits (Mohsenin, 1986).

Two types of techniques (regression and ANN) were considered for modeling of the fruits mass and volume based on their dimensions. In the regression model (F(h,w,t)), three dimensions of the orange fruits were selected as independent variables and their mass or volume were selected as dependent variable (Masoudi & Rohani, 2017). Also, multilayer perceptron (MLP) neural network was used for modeling the mass and volume of orange fruits based of their dimensions (A (h, w, t)). The orange dimensions normalized values were selected as inputs and the orange mass or volume was selected as output of the ANN. Sigmoid function was selected as neurons activation function. Back-propagation with declining learning-rate factor (BDLRF) algorithm was used for the ANN training. Computer program of the ANN algorithm was developed in MATLAB version 8.1 software (Masoudi & Rohani, 2016).

The electronic system set up was built according to Figure 1, using CATIA v5, R2013 software (Dassault Systèmes, France). This system instantly determines the three geometric dimensions of orange fruit, including height (h), width (w), and thickness (t), and saves them in memory. The hardware components of this system include a metal case, three ultrasonic sensors, a load-cell sensor, an Arduino microcontroller board, a memory card module, a voltage converter, a keypad, an LCD, and a power adapter.

A Mega Arduino microcontroller board was used as the system processor (Figure 2-a). A memory card module (Arduino data logger shield) mounted on the Arduino board was used to save the data. A voltage converter module was also used to supply the required voltage to the sensors from the adapter. A 3×4 keypad and a 4×20 LCD were mounted on the top of metal case for settings and showing results (including three dimensions, mass, and volume of oranges).

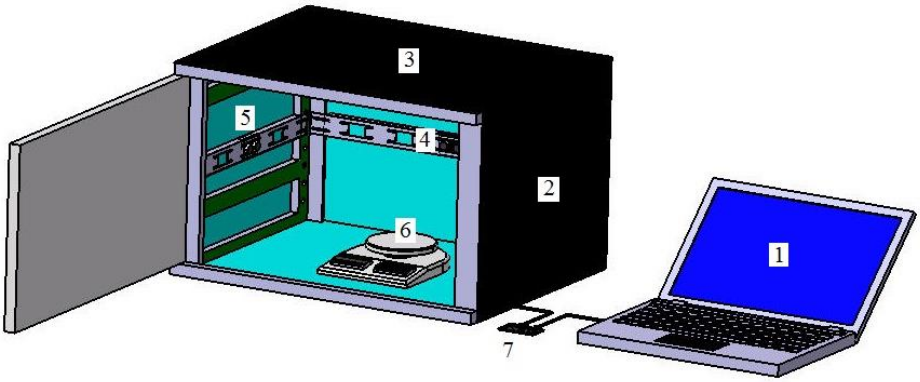

Fig. 1. Electronic system set up to determine the mass and volume of orange fruits (1- Computer 2- Metal body 3- LCD display 4- Thickness sensor 5- Width sensor 6- load-cell sensor 7- Arduino board)

(a) (b)

Fig. 2. a) Arduino Mega board, and b) USS3 ultrasonic sensor

Three USS3 ultrasonic sensors (Best Technology, Japan) were used to determine dimensions of the orange fruit (Figure 2-b). Values of the internal parameters of this sensor were adjusted to detect objects at distances of 15 to 250 cm (Anonymous, 2008). An ultrasonic sensor was installed at top of the case to determine the fruit height, one on the right side of the case to determine the fruit width, and another at the back of case to determine the fruit thickness. Then, the analogue output of the sensors was connected to the A/D input of the Arduino board. Each sensor receives a reflection by sending a sound wave, and sends the fruit-sensor distance, as a DC voltage in its output, to the Arduino board. USS3 sensor output voltage in the analogue mode (V) is proportional to distance (d). The calibration coefficient, named DAC_value [cm], shows the distance in which the sensor output is 5 Volt. In this study, DAC_value was determined (=45.75 cm) and used to calculate distance using Equation 1. Also, sound speed (v in m s^{-1}) can be saved as an internal parameter of USS3 sensors according to the environment temperature (T in °C). This parameter was calculated for the laboratory temperature (= 22 °C) and saved as an internal parameter of the sensors using Equation 2 (Anonymous, 2008):

$$d = V \times DAC\_value / 5 \quad (1)$$

$$v = 331.5 + 0.605 \times T \quad (2)$$

An YZC-133 load-cell sensor with 5 kg capacity was used to get the fruits mass (Figure 3-a). An AD620 voltage amplifier module was used to amplify the output signals of the load-cell up to 4000 times. The load-cell calibration equation was obtained as shown in Figure 3-b.

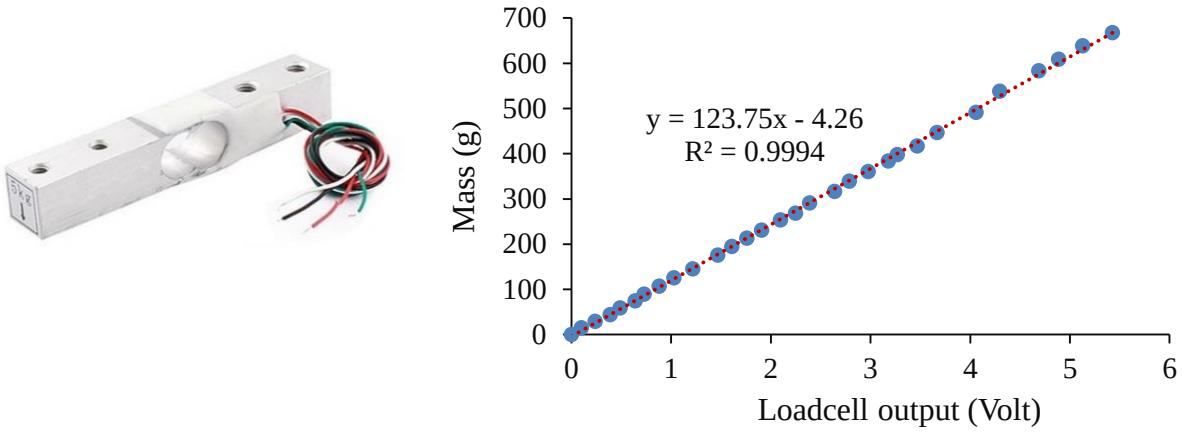

(a) (b)

Fig. 3. a) YZC-133 Load-cell and b) Calibration graph and equation of the load-cell

A computer program was written using Arduino IDE version 1.8.9 to obtain data from the ultrasonic and load-cell sensors by the microcontroller, determine the required parameters (including orange mass and volume), and display and save them on the memory card. In the computer program, the relationships between three dimensions and fruit mass and volume were used to determine the fruit mass and volume obtained by regression modeling (Figure 4). While the Sync line of USS3 sensors was used, the sensors were activated at one-second intervals. Therefore, the sensors output were read with one-second distance between them. As a result, the signals interference was decreased. A median filter was also used in the program for deleting remained noises from all sensors outputs. The system performance was simulated in Proteus 8.13 software (Labcenter Electronics, England) as shown in Figure 5.

To evaluate the performance of electronic system in determining the mass and volume of orange fruits, 50 samples (Concha-Meyer *et al.*, 2018) of the fresh orange fruit (Dezful local variety) were provided, and the actual values of their three dimensions, mass and volume were determined by a digital caliper, a digital scale (with an accuracy of 0.05 g), and WDM, respectively. Then, as shown in Figure 6, three dimensions, mass and volume of all 50 fruits were measured using the proposed electronic system at four repetitions. Finally, two statistical criteria, i.e. root mean square error (RMSE) (Equation 3) and mean absolute percentage error (MAPE) (Equation 4) were used for the results evaluation. Comparison of the mean of real values with the system output values was performed at 1% probability level by paired Student t test using Excel 2013 software (Microsoft, USA) (Masoudi & Rohani, 2021).

$$RMSE = \sqrt{\frac{\sum_{i=1}^{n}(A_i - P_i)^2}{n}} \quad (3)$$

$$MAPE = \frac{\sum_{i=1}^{n}\left|\frac{A_i - P_i}{A_i}\right|}{n} \times 100 \quad (4)$$

Where A_i is the actual mass or volume of the fruit, P_i is the output value of the system, and n is the number of fruits.

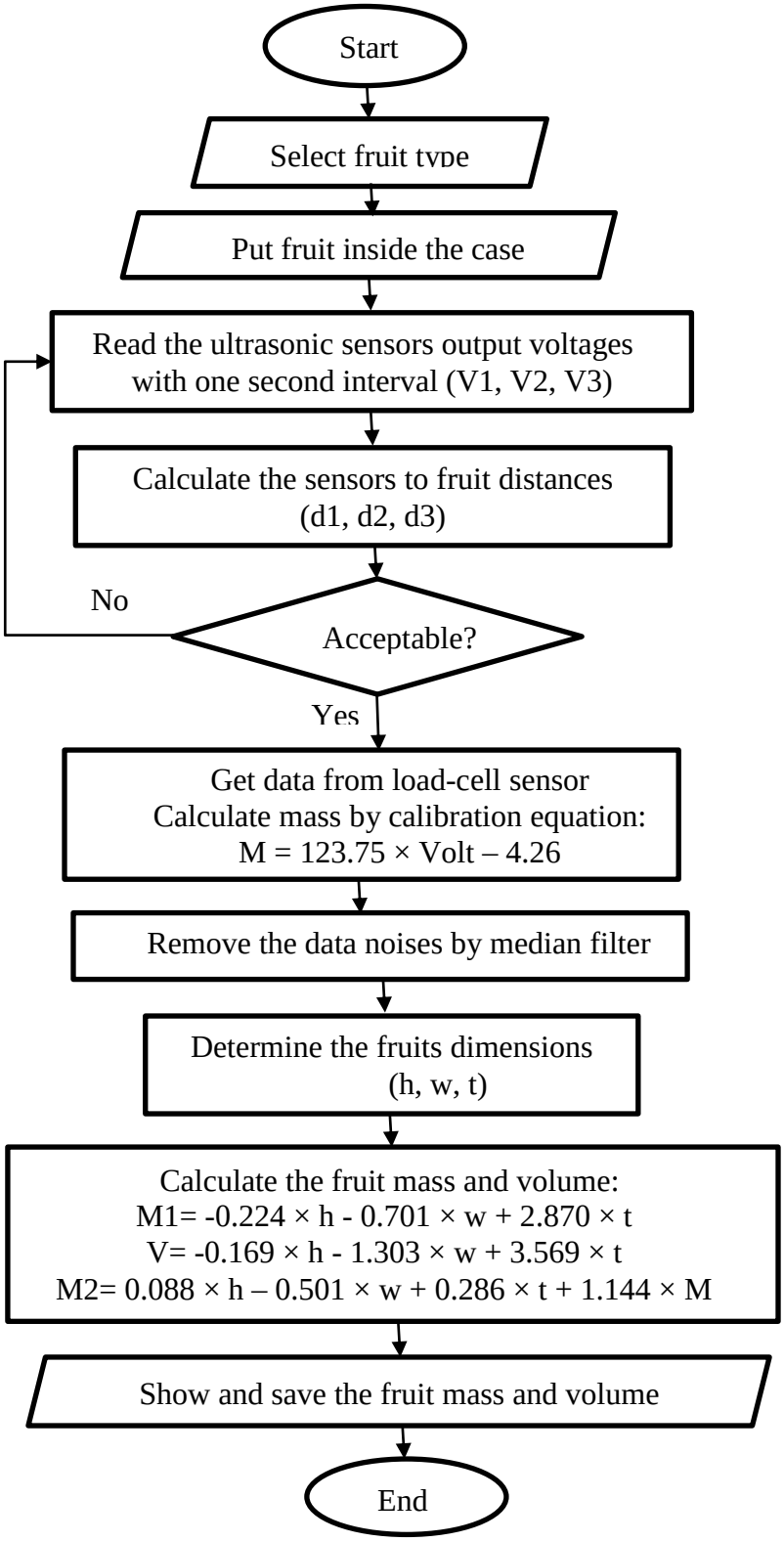

Fig. 4. Steps for determining the orange mass and volume by the electronic system

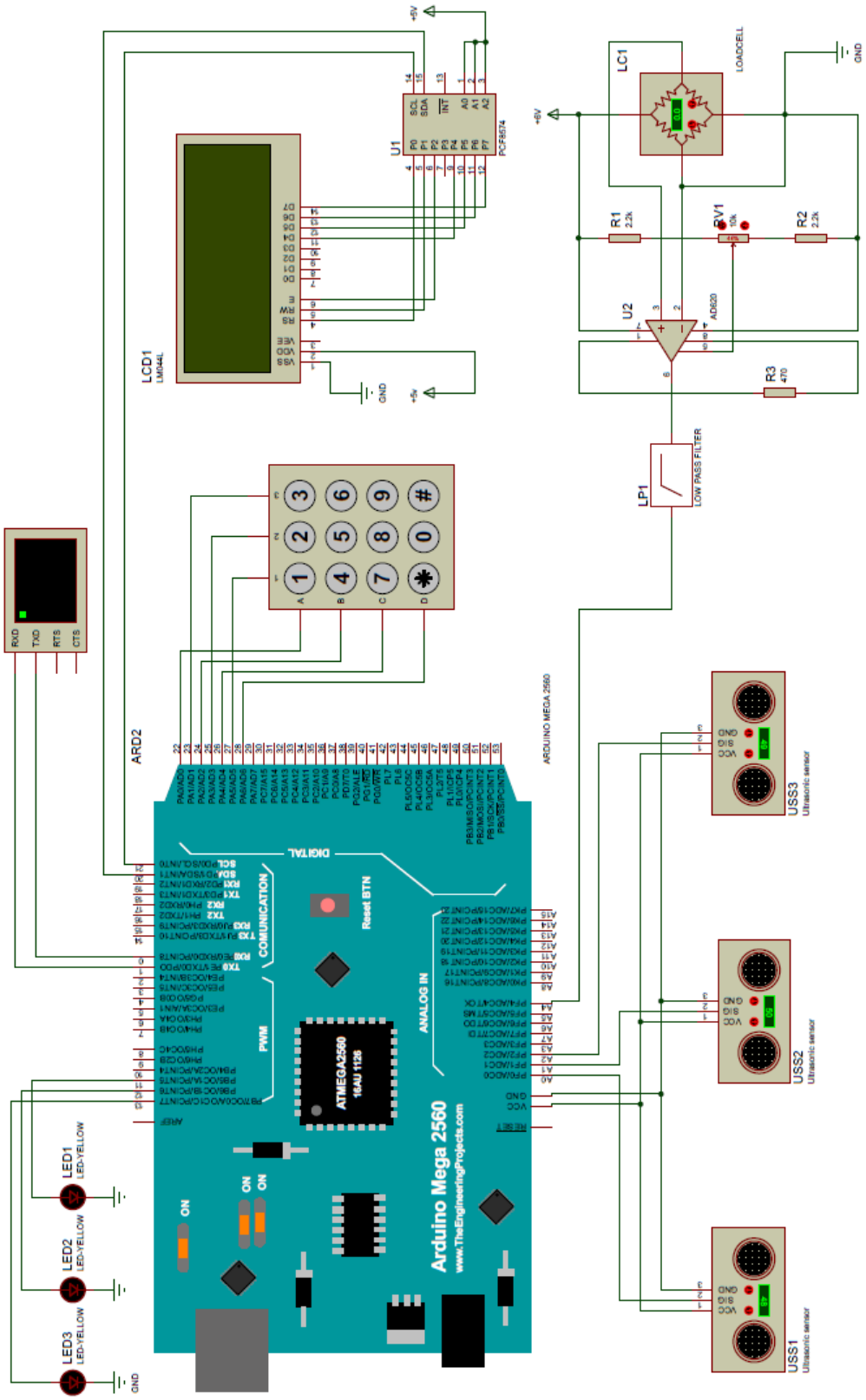

Fig. 5. Electronic circuit of the system designed in Proteus software

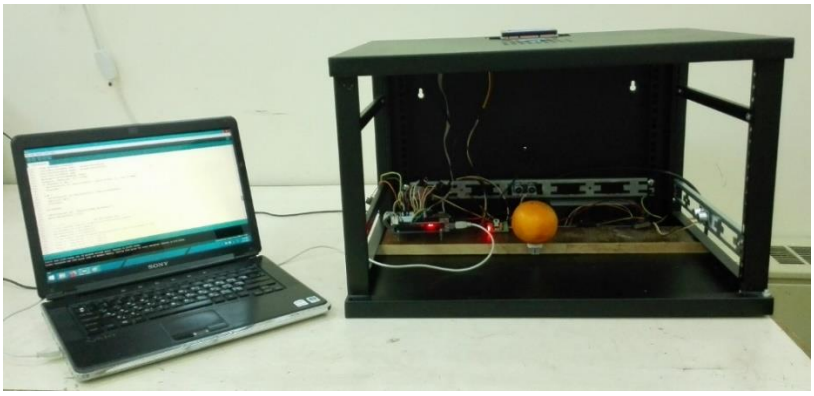

Fig. 6. Practical tests to evaluate the performance of the built electronic system

Results and Discussion

Analysis of variance of the F (h,w,t) model showed that there was a significant relationship at 1% level between the mass or volume of oranges and three dimensions. The obtained regression equations for orange mass and volume estimation based on three dimensions are shown in Equations 5 and 6. The R^2 values show that these equations can justify 95.97% and 98.01% of changes in the orange mass and volume, respectively (Masoudi & Rohani, 2017).

$$M = -188.30 + 0.600\,h + 1.899\,w + 2.583\,t \quad , \quad R^2 = 95.97\ \% \tag{5}$$

$$V = -252.30 + 1.703\,h + 2.246\,w + 2.317\,t \quad , \quad R^2 = 98.01\ \% \tag{6}$$

Also, in the ANN modeling, the results of statistical comparisons between the mean, variance, and distribution of the actual data and the predicted data showed that there was no significant difference between them and the minimum value of R^2 for the mass and volume in all three phases of the ANN was equal to 0.96. According to these results, the A (h, w, t) model could learn well the pattern of changes in the mass and volume of orange fruits using their dimensions (Masoudi & Rohani, 2016).

Finally, the two proposed models for estimating the mass and volume of orange fruits were compared with each other. According to the small values for RMSE and MAPE and the large value for EF indices, the prediction performance of A (h, w, t) model was better than the F (h, w, t) model. One-way analysis of variance was done for three set of data including the actual data, the predicted data by the F (h, w, t), and the predicted data by A (h, w, t). The results of mean comparison by LSD method for these three set of data showed that the difference between them were not significant at 1% probability level. So there was no difference between the two models statistically and each one of the models could be used to estimate the orange mass or volume (Masoudi & Rohani, 2016, 2017). Since, the regression model implementation was easier and its running was faster than the ANN model in Arduino boards, so this model was used for final evaluation of the electronic system performance in this study.

The actual values of the physical characteristics for Dezful local variety of orange fruit along with the values measured by the system are given in Table 1. Low standard deviation (SD) and coefficient of variation (CV) of characteristics indicate the uniformity of fruit. Regression equations between the geometric dimensions of orange fruit with their actual mass and volume values were obtained according to Equations 7 to 9. Due to high R^2 of these relationships and since the regression equations in terms of three dimensions of oranges have good accuracy in determining the mass and volume of orange fruit (Masoudi & Rohani, 2016, 2017), these regression equations were used to evaluate the system performance. In practice, the volumes calculated by equations 8 and 9 were completely equal together. Therefore, the

results mentioned below are correct for both of these equations.

$$M = -0.2243\,h - 0.7013\,w + 2.8703\,t \quad , \quad R^2 = 99.61\% \qquad (7)$$

$$V = -0.1690\,h - 1.3027\,w + 3.5691\,t \quad , \quad R^2 = 99.54\% \qquad (8)$$

$$V = 0.0876\,h - 0.5005\,w + 0.2859\,t + 1.1438\,M \quad , \quad R^2 = 99.97\% \qquad (9)$$

The comparison of the actual geometric dimensions of the orange fruit (obtained from the practical experiments) with the measured dimensions by the electronic system is shown in Figure 7. Comparing the means with Student t-test showed no significant difference between the system output values and their real values for orange fruit height and width at 1% probability level. However, there was a significant difference between the actual thickness values and the system output at 5% probability level. Therefore, the system accuracy in determining the thickness was less than the other two dimensions. But, considering that there is no significant difference between the values of geometric mean diameters (GMD) in both methods at 1% level, it can be concluded that the electronic system performance in determining the geometric dimensions of orange fruit is acceptable.

Table 1- Physical characteristics of the orange fruits determined by the system

Physical characteristics	Average		SD		CV (%)	
	Actual value	System output	Actual value	System output	Actual value	System output
Height (mm)	59.34	59.14	2.62	2.11	4.42	3.57
Width (mm)	60.87	60.39	2.36	3.05	3.88	5.05
Thickness (mm)	60.17	58.97	2.38	2.83	3.96	4.81
GMD* (mm)	60.12	59.48	2.19	2.23	3.65	3.74
Mass (g)	116.48	113.64	11.84	6.55	10.17	5.77
Volume (cm^3)	125.15	121.79	13.54	7.59	10.82	6.23
Density (g cm-3)	0.93	0.93	0.02	0.01	1.70	0.99

* Geometric mean diameters

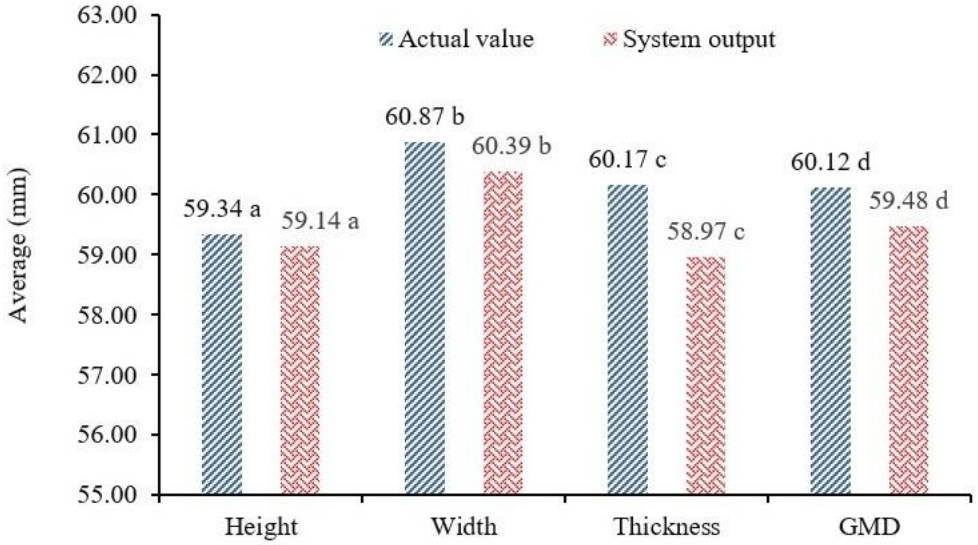

Fig. 7. Comparison of the actual values of orange fruits geometric dimensions with the values measured by the electronic system

As shown in Figure 8, based on the Pearson's correlation coefficient values the actual and measured values for volume and mass of orange fruits were highly correlated. Also, the mean errors (RMSE) for determining the orange mass and volume by the system were 9.02 g and 10.90 cm^3, respectively, and the MAPE for determining the mass and volume of oranges by the system was 5.54 and 6.13%, respectively. These mean that the electronic system could determine the mass and volume of fruits with a minimum error that is acceptable for commercial uses.

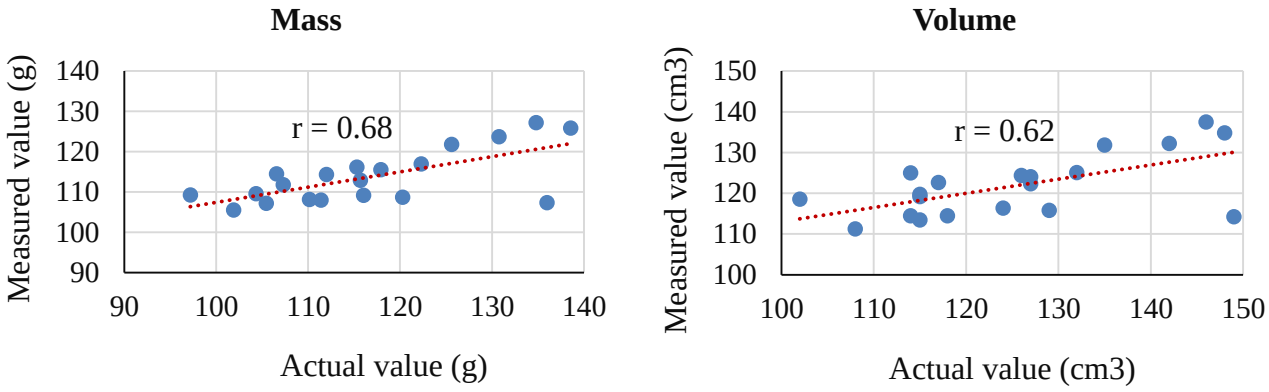

Fig. 8. Correlation of actual and measured values for mass (left) and volume (right) of orange fruits

The student t-test showed no significant difference between the system output values for mass, volume and density of orange fruit with their actual values at 1% probability level. Comparison of the actual mass and volume of orange fruit (obtained from the practical experiments) with the values measured by the electronic system is shown in Figure 9. In the study of Omid *et al.* (2010), and Fellegari & Navid (2011), no significant difference was observed between the orange volume predicted by the image processing technique and the actual values of this parameter.

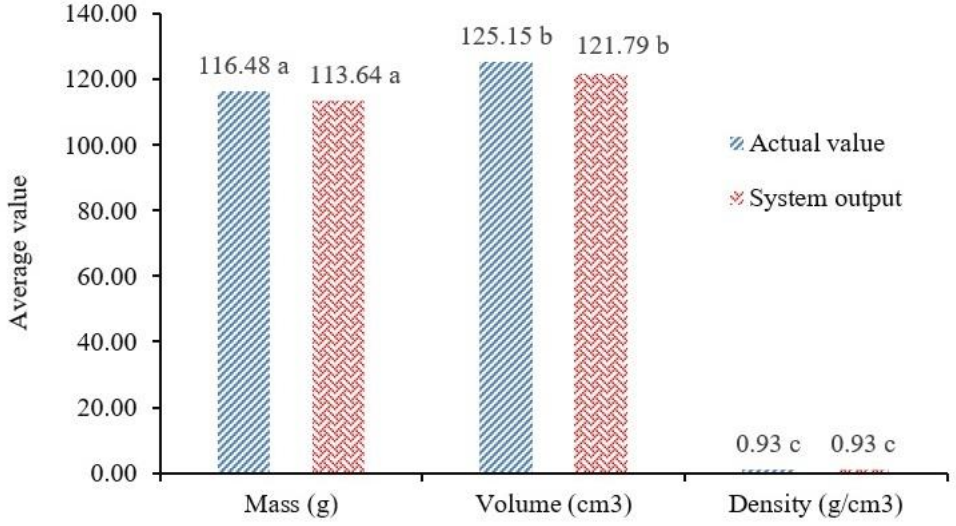

Fig. 9. Comparison of the actual values of mass and volume of orange fruits with the values measured by the electronic system

According to these results, the electronic system performance in determining the mass and volume of orange fruit is acceptable. This system can be used to determine these two characteristics. The proposed system is a prototype and laboratory version. By this system, it is possible to estimate the volume of one fruit in 5 seconds, which will be 720 fruits per hour and will weigh between 80 and 100 kg. For 10 hours of work per day, about 1000 kg of fruits can be graded. Also, installing several grading lines in parallel can increase the grading capacity. Since volume determination by WDM takes about 1 minute time, so this system is more comfortable and about 12 times faster than WDM.

Conclusion

The applied system evaluation experiments, using regression equations, showed that the system performance in determining the orange fruit mass and volume is acceptable and can be used to determine these two characteristics. Since, the system can determine the volume of fruits with only three ultrasonic sensors, by removing the load-cell, the system production costs will decrease. For commercialization, regression equations to estimate the fruits volume from their dimensions for various fresh and un-fresh fruits with different moisture content should be extracted and added to the computer program of the system. The salient features of the presented system for online grading of fruit based on their volume are: less complex than vision systems, working in any lighting conditions, less cost, and ability to save the results.

Acknowledgements

This work was supported by the Vice Chancellor for Research and Technology of Shahid Chamran University of Ahvaz, Iran [internal research plan number 1263]. The authors thank the Shahid Chamran University of Ahvaz for this financial support.

References

1. Ahmadi, K., Ebadzade, H. R., Hatami, F., Hoseinpoor, R., & Abdeshah, H. (2020). *Agricultural Statistics Letter*, Volume 3: Horticultural crops. Ministry of Agriculture, Deputy of Planning and Economics, Information and Communication Technology Center, Tehran. (in Persian)
2. Anonymous. (2008). USS3 ultrasonic sensor. Retrieved from https://www.besttechnology.co.jp. Accessed 17 November 2021. (in Japanese).
3. Concha-meyer, A., Eifert, J., Wang, H., & Sanglay, G. (2018). Volume estimation of strawberries, mushrooms, and tomatoes with a machine vision system. *International Journal of Food Properties*, *21*(1), 1867-1874. https://doi.org/10.1080/10942912.2018.1508156
4. Dağtekin, M., & Beyaz, A. (2017). Use of different types of sensors for size measurement of some agricultural products (fruit) grown in Mediterranean climatic conditions. *Environmental Engineering and Management Journal*, *16*(5), 1129-1136. https://eemj.eu/index.php/EEMJ/article/view/3268
5. Fellegari, R., & Navid, H. (2011). *Determining the orange volume using image processing. International Conference on Food Engineering and Biotechnology* (IPCBEE v. 9). Singapoore: IACSIT Press, p. 180-184.
6. Kachariya, H., Vasaniya, K., Dhameliya, S., & Savant, R. (2015). A review of volume estimation techniques of fruit. *International Journal of Engineering Research & Technology*, *4*(1), 217-221.
7. Masoudi, H., & Rohani, A. (2016). Mass and volume prediction of orange fruit (Dezful local variety) using MLP neural networks. *Journal of Agricultural Engineering*, *39*(2), 133-142. (in Persian). https://doi.org/10.22055/agen.2017.12609

8. Masoudi, H., & Rohani, A. (2017). Determination of physical characteristics and regression modeling of orange (Dezful local variety) mass and volume. *Journal of Biosystems Engineering, 6*(2), 34-42. (in Persian).
9. Masoudi, H., & Rohani, A. (2021). Citrus fruit grading based on the volume and mass estimation from their projected areas using ANFIS and GPR models. *Fruits, 76*(4), 169-180. https://doi.org/10.17660/th2021/76.4.2
10. Mir-Ahmadi, S., Mireei, S. A., Sadeghi, M., & Hemmat, A. (2016). Online weighing of kiwifruit using impact method. *Journal of Agricultural Machinery,* 6(1), 163-175. (in Persian). https://doi.org/10.22067/jam.v6i1.33683
11. Mohsenin, N. N. (1986). *Physical Properties of Plant and Animal Materials*. Gordon and Branch Sci. Pub., New York.
12. Omid, M., Khojastehnazhand, M., & Tabatabaeefar, A. (2010). Estimating volume and mass of citrus fruit by image processing technique. *Journal of Food Engineering, 100*(2), 315-321. https://doi.org/10.1016/j.jfoodeng.2010.04.015
13. Raj Gokul, P., Raj, Sh., & Suriyamoorthi, P. (2015). *Estimation of volume and maturity of sweet lime fruit using image processing algorithm*. International Conference on Communication and Signal Processing. April 2-4, 2015, India.
14. Vivek Venkatesh, G., Iqbal, S. Md., Gopal, A., & D. Ganesan. (2015). Estimation of volume and mass of axi-symmetric fruits using image processing technique. *International Journal of Food Properties, 18*(3), 608-626. https://doi.org/10.1080/10942912.2013.831444
15. Yildiz, F., Özdemir, A. T., & Uluişik, S. (2019). Evaluation performance of ultrasonic testing on fruit quality determination. *Journal of Food Quality*, Article ID 6810865: 7 pages. https://doi.org/10.1155/2019/6810865

نشریه ماشین‌های کشاورزی
https://jame.um.ac.ir

مقاله پژوهشی
جلد ۱۳، شماره ۱، بهار ۱۴۰۲، ص ۶۶-۵۵

تعیین جرم و حجم میوه پرتقال با استفاده از حسگرهای فراصوتی

حسن مسعودی[1*]

تاریخ دریافت: ۱۴۰۱/۰۲/۲۳
تاریخ پذیرش: ۱۴۰۱/۰۸/۱۷

چکیده

در این پژوهش یک سامانه الکترونیکی برای تعیین جرم و حجم میوه پرتقال با استفاده از حسگرهای فراصوتی ساخته شد. اجزای سخت‌افزاری سامانه شامل بدنه فلزی، حسگرهای فراصوتی، حسگر نیرو، برد آردوینو، ماژول کارت حافظه، مبدل ولتاژ، صفحه کلید، نمایشگر و آداپتور برق می‌باشد. یک برنامه رایانه‌ای برای اخذ داده‌ها از حسگرهای فراصوتی و تعیین جرم و حجم پرتقال‌ها با کمک روابط رگرسیونی در نرم‌افزار آردوینو نوشته شد. ۱۰۰ نمونه از میوه پرتقال رقم محلی دزفول از یک باغ به‌صورت تصادفی چیده شد و آزمایش‌های مختلفی برای تعیین خواص فیزیکی آن‌ها شامل ابعاد، جرم و حجم میوه انجام شد. مطابق نتایج ارزیابی سامانه، بین مقادیر خروجی سامانه با مقادیر واقعی جرم و حجم میوه‌های پرتقال رقم محلی دزفول اختلاف معنی‌داری در سطح احتمال یک درصد مشاهده نشد. مقادیر ریشه میانگین مربعات خطا (RMSE) در تعیین جرم و حجم پرتقال‌ها توسط سامانه به‌ترتیب برابر با ۹/۰۲ گرم و ۱۰/۹۰ سانتی‌مترمکعب به‌دست آمد. در مجموع، عملکرد سامانه ساخته‌شده قابل‌قبول بود و لذا می‌توان از آن برای تعیین جرم و حجم میوه‌های پرتقال استفاده نمود.

واژه‌های کلیدی: اجزای سخت‌افزاری، تعیین جرم و حجم، سامانه الکترونیکی، مدل‌سازی رگرسیونی، میوه پرتقال

۱- استادیار، گروه مهندسی بیوسیستم، دانشکده کشاورزی، دانشگاه شهید چمران اهواز، اهواز، ایران
(*- نویسنده مسئول: Email: hmasoudi@scu.ac.ir)

https://doi.org/10.22067/jam.2022.76674.1106

Journal of Agricultural Machinery

Homepage: https://jame.um.ac.ir

Research Article
Vol. 13, No. 1, 2023, p. 67-83

Experimental Investigation of Performance and Emissions of a Compression Ignition Engine Using a Combination of Compressed Natural Gas and Diesel Fuel

Y. Niknam[1], D. Mohammadzamani[2*], M. Gholami Pareshkoohi[3]

1- Ph.D. student, Department of Biosystems Engineering, Islamic Azad University, Ttakestan Branch, Takestan, Iran
2- Assistant Professor, Department of Biosystems engineering, Islamic Azad University, Ttakestan Branch, Takestan, Iran
3- Associate Professor, Department of Biosystems engineering, Islamic Azad University, Ttakestan Branch, Takestan, Iran
(*- Corresponding Author Email: dr.dmzamani@gmail.com)
https://doi.org/10.22067/jam.2023.79199.1127

Received: 16 October 2022
Revised: 25 December 2022
Accepted: 07 January 2023
Available Online: 07 January 2023

How to cite this article:
Niknam, Y., Mohamadzamani, D., & Gholami Pareshkoohi, M. (2023). Experimental Investigation of Performance and Emissions of a Compression Ignition Engine Using a Combination of Compressed Natural Gas and Diesel Fuel. *Journal of Agricultural Machinery, 13*(1): 67-83. https://doi.org/10.22067/jam.2023.79199.1127

Abstract

This study presents the effects of compressed natural gas fuel on a four-cylinder compression ignition engine. Compressed natural gas as the main fuel and diesel fuel as the igniter were used to investigate performance and emissions from the dual fuel engine. According to the engine speed and load, the amount of diesel fuel as igniter was adjusted using mechanical changes in the governor, while no ignition system was used. The engine experimental tests were performed at engine speeds of 1200, 1400, 1600, 1800 and 2000 rpm, using diesel fuel and dual fuel. These data were collected in the Engine Research Center of Tabriz Motorsazan Company and experimental runs were repeated three times. The maximum torque of the engine in diesel mode was 360 N m at 1400 rpm. Compared to the diesel mode, the dual fuel mode showed the maximum torque by 334 N m at 1600 rpm, which is about 26 N m less than that gained from the diesel mode. Considering emissions analysis at 2000 rpm, it is seen that the amount of NOX, HC, CO_2 and CO emissions in the dual fuel mode was 20, 53, 16 and 86% more than diesel mode, respectively. However, O_2 and soot showed the highest reduction at 2000 rpm for dual fuel mode by 51% and 69% respectively. This study indicated that there was a considerable enhancement in exhausted emissions when the injection of the diesel fuel as igniter was done mechanically. In this regard, control the amount and time of the igniter injection could likely be helped for better control of emissions. Therefore, further research on the modification of the diesel injection system as igniter or CNG injection system is needed towards reducing emissions.

Keywords: Compression ignition engine, Compressed natural gas, Diesel, Pollution, Power

Introduction

The massive energy subsidies in the transportation sector have been the serious challenges of the Iranian economy in recent decades. The dependence of the country's transportation cycle on imported petroleum products is a very vulnerable from both political and peripheral point of view. The release of gasoline and diesel prices, quotas, gas burning and all -out public transport development have been described as solutions to exit this crisis. Among these options, and in terms of the fleet's approach and a glimpse of alternatives, as well as the frequency of Iran's gas reserves as the second source of the gazette, the option of using gas -fired vehicles from other options Distinct (Mirfattah, 2010). Countries around the world have set a variety of goals in the use of Compressed Natural Gas (CNG). They use gas cars partly to reduce fuel costs and partly to reduce environmental pollution. International law and the recommendation of the international community to protect the environment are an

impact on the approach to the natural way. In 1995, for example, the global Energy Authority in Tokyo officially declared compressed natural gas consumed in the transportation system (Mirfattah, 2010). In the meantime, compression ignition engines are widely used in the transportation sector, where demand for fossil fuels is high. About 60 percent of European passenger cars use these types of engines (Saravanan, Kumar, Ettappan, Dhanagopal, & Vishnupriyan, 2020). Given the effect that contamination has on human health and the environment, it can be concluded that the issue of contamination of internal combustion engines is of high importance (Assasi, Mirzaei, & Khoshbakhti Saray, 2017).

The use of compressed natural gas fuel in combustion engines based on liquid fuels is associated with problems such as reducing efficiency and increasing corrosion of the engine components. The use of compressed natural gas fuel in combustion engines based on the auto cycle (spark ignition) has passed its research and development stage for years and is now widely used in some countries, including Iran. However, the use of compressed natural gas fuel in diesel cycle engines without the use of sparking system goes through its research steps and is not widely used commercially. One of the problems with the use of compressed natural gas fuel in common compressions is the high cost of converting these engines into a spark ignition engine. This conversion requires the use of spark system components such as coil, wire and candles, and in electronic spraying systems, processors and sensors. It is also a relatively difficult task to change the cylinder head and install candles. On the other hand, the compression ignition engine that turns into a spark ignition engine can only work with a type of fuel (CNG) and cannot be used in diesel fuel (Sajedian, Mohammadzamani, & Ranjbar, 2014). In comparison with other fuels that can be used in compression ignition engines, diesel fuel has a lower Stan number, lower energy consumption from well-to-wheel, and the amount of CO and HC emissions is relatively low, but the amount of NO_X and suspended particles from well-to-wheel is high (Azizi, Mahdaloui, & Hassani, 2013). Relatively few researches have been conducted on the possibility of using compressed natural gas in diesel engines without the use of an ignition system, and a significant part of the existing studies has been on systems equipped with spark ignition. In a study, the Perkins 1104D-E44TA engine heat release was studied with compressed gas and diesel fuel. The heat release property is a criterion of the combustion process, so this variable affects the engine performance indicators. In this study, heat release for a dual engine was compared with the heat release features for a diesel engine under the same operating conditions. The analysis of heat release properties was performed in the range of their effect on the concentration of NO_2 in the engine exhaust. The results of this study showed that the greater share of compressed natural gas in the total amount of energy released in the engine cylinders causes a greater difference in the combustion process and also reduces the concentration of NO_2 in the engine exhaust (Kurczynski, Lagowski, & Pukalskas, 2019). In a research to investigate the effect of ignition fuel amounts on the combustion process, performance and emissions, dual fuel diesel engines with indirect injection were evaluated in all load conditions. In this research, the ignition delay time interval and the combustion process and the formation of pollutants in the dual engine were investigated in two ways. In the first case, the amount of ignition fuel is kept constant, and by adding gas fuel, the engine load is increased, and in the second case, for partial load of 25% and full load, the increase in gas fuel and the decrease in ignition fuel shortens the length of the combustion process. and it reduces CO and HC pollutants, but in partial loads with increasing gas fuel and decreasing ignition fuel, the duration of the combustion process becomes longer and CO and HC pollutants increase strongly (Mohammadi Koosha, Piroozpanah, Khoshbakht Sarai, & Salsbili, 2008). In a

study, the functional variables and emissions of diesel engine in different ratios of air-to-fuel balance ratio were discussed using diesel-channel fuel mixtures. The results showed that the increase in ethanol in the diesel and ethanol mixture increased the air -to -fuel balance ratio, resulting in a decrease in power and torque and increased engine fuel consumption (Shadidi, Haji Agha Alizade, Najafi, Moosavian, & Khazaee, 2020). A number of researchers conducted an empirical examination of a compression combustion engine to study functional and pollution parameters, using compressed natural gas fuel and diesel. The engine was modified to work with a mixture of diesel fuels and natural gas in dual -fuel state so that diesel fuel was injected into the cylinder, while natural gas into the input air pipe with two controlled injectors were injected. The energy content of the gas fuel injected in zero values (diesel fuel), 15, 40 and 75% of the total fuel energy content vary. In addition to experiments, the engine was modeled with a single-dimensional commercial software. The results showed that both NO_X and soot emissions decreased by 15 and 40% and energy content rates in the gas-burn mix, respectively, compared to diesel fuel. However, an increase in carbon monoxide emissions was observed by adding 15% natural gas fuel compared to diesel fuel (Karagoz, Sandalc, Koylu, Dalkilicx, & Wongwises, 2016). In a resaerch, experimental investigation of compressed natural gas using in an indirect injection diesel engine at different conditions was conducted. The novelty of this experimental work is replacing different mass fractions of diesel fuel with natural gas in an indirect injection diesel engine and evaluating its effect on the emissions of soot and nitrogen oxides, and brake specific fuel consumption in the presence of cold exhaust gas recirculation. Experiments were done at different equivalence ratios with 1200, 2000, and 3000 rpm and at 25, 50, and 75% of the full load in each speed. Replacing 40% mass fraction of input diesel fuel by adding natural gas resulted in a maximum 74% reduction of soot; the reason is a decrease in carbon to hydrogen ratio in the mixture (Bayat & Ghazikhani, (2020)). An empirical and numerical study on the effect of diesel injection scheduling from 10 to 50 degrees before the top death center (BTDC) on combustion and greenhouse gas emissions of a dual-fuel-burner-powered engine in the engine was conducted. The results of this study showed that the highest thermal efficiency indicated was obtained in the scheduling of diesel injection 2 and 2 degrees BTDC. Finally, with increased diesel injection time from 10 degrees BTDC to 50 degrees BTDC, NO_X, methane and CO decreases by 65.8, 83 and 60%, respectively, while the thermal efficiency increases by 7.5% (Yousefi, Birouk, & Guo, 2017). A research was conducted on CNG-diesel dual fuel engine by optimizing the timing of CNG injection from 70° to 150° ATDC and the duration of CNG injection from 70° to 150° CA with 20° intervals at low load. The results explained that by retarded the timing of CNG injection (130° ATDC) yielding a value of cylinder pressure and heat release rate (HRR) was the highest with emissions of hydrocarbon (HC), carbon monoxide (CO) and particulate matter (PM) were lower and also the amount of CNG volume inserted into the cylinder was more large with optimal CNG injection duration of 110° CA on CNG-diesel dual fuel engine under low load (Yuvenda, Sudarmanta, Wahjudi, & Muraza, 2020).

Considering that the studies have focused on the possibility of using CNG using a spark ignition system, this study aims to determine the feasibility of using compressed natural gas in a compression ignition engine without using an ignition system and its effects on engine performance and pollutant emissions have been investigated. So the aim of the research was to investigate the effect of using two types of fuel including diesel fuel and dual fuel (diesel + CNG) in a compression ignition engine on performance indices and the amount of pollutant emissions.

Materials and Methods

The combustion engine used in this study is a four -cylinder complication engine manufactured by Tabriz Motorsazan Company whose maximum power is at the speed of 2000 rpm, 82 hp. Other technical specifications of this engine are presented in Table 1. In the tests, the engine was started with diesel fuel and CNG fuel was not used in idle mode. In the tests, by increasing the rotational speed of the engine, CNG fuel was used as the main fuel and diesel (with Euro 4 standard) was used as the ignition fuel.

Table 1- Technical specifications of the engine used in the research

Engine specifications	Value
Cylinder number	4
Piston diameter (mm)	100
Piston courses (mm)	127
Compression ratio	17.5
Maximum power (hp) at 2000 (rpm)	82
air inlet system	Turbocharger
Maximum torque (N m) at 1400 (rpm)	360
Volume Capacity (L)	3.99

Equation (1) was used to achieve fuel consumption in the dual diesel and natural gas refueling system in each combustion chamber (Sontag, Borgnakke, & Van Wylen, 2015).

$$\dot{V}_{Fuel} = \dot{V}_{Diesel\,oil} + \dot{V}_{CNG} \quad (1)$$

In which $\dot{V}_{Fuel}$is volume flow rate of combined $\dot{V}_{CNG}$ is volumetric flow rate of CNG fuel consumption (l.hr^{-1}).

The ratio of gas entry to dual ga and diesel (α) is calculated as follows:

$$\rightarrow \dot{V}_C = \alpha \dot{V}_f \longrightarrow \quad \dot{V}_g = (1-\alpha)\dot{V}_f$$

$$\alpha = \frac{\dot{V}_c}{\dot{V}_F} \quad (2)$$

In which $\dot{V}_c$ is volumetric flow rate of gas and $\dot{V}_F$is volumetric flow rate gas and diesel.

Due to the power of 82 hp for the compression ignition engine used in this study, the dual fuel system (diesel and CNG) must be able to supply the energy needed to produce this power. Therefore, according to the first law of thermodynamics (Equation 3 (Sontag *et al.*, 2015)):

$$\dot{Q} = (\dot{U}_2 - \dot{U}_1) + \dot{W} \quad (3)$$

In which $\dot{Q}$is the heat rate created in the process (hp), $\dot{U}_1$is the producted power in the process (hp), $\dot{U}_2$ is the internal energy rate in the process (hp) and $\dot{W}$ is equal to 82 hp.

Table 2- Some physical and thermal properties of air, diesel fuel and CNG (Chala, Aziz, & Hagos, 2018)

	ρ (kg m^{-3})	C_v (kJ kg^{-1}. $\dot{k}^{-1}$)	$\dot{V}_f$
Air	1.169	103	17.16 (1-α) $\dot{V}_f$
Diesel	750	214	α $\dot{V}_f$
CNG	0.648	1.736	(1-α) $\dot{V}_f$

$$\dot{U}_2 - \dot{U}_1 = \left[\dot{m}_{air} C_{V\,air} + \dot{m}_C C_{v\,C} + \dot{m}_g C_{v\,g}\right]\Delta T = \left[\rho_{air}\dot{V}_{air} C_{V\,air} + \rho_C \dot{V}_C C_{v\,C} + \rho_g \dot{V}_g C_{v\,g}\right]\Delta T \quad (4)$$

Next, considering the values of Table 2 and the internal energy equation for dual fuel and air:

$$\dot{U}_2 - \dot{U}_1 = \left[577.98\times10^{-3} + 9072.185\times10^{3}\alpha\dot{V}_f\right] \quad (5)$$

$$\dot{Q} = \dot{m}_f LHV \quad (6)$$

In which: $\dot{m}_f$ is mass flow rate of dual fuel and LHV is the low heat value equal to 2 $kJ.kg^{-1}$. Mass flow rate was calculated from Relationship 7 (Sontag *et al.*, 2015):

$$\dot{m}_f = \rho \dot{V}_f \ (\frac{kg}{s}) \quad (7)$$

$$\begin{aligned}\dot{Q} &= \dot{m}_f LHV \\ &= \left[\rho_C \dot{V}_C + \rho_g \dot{V}_g\right] LHV \\ &= \left[0.648\alpha \dot{V}_f + 750(1-\alpha)\dot{V}_f\right] LHV \\ &= \left[0.648\alpha \dot{V}_f + 750(1-\alpha)\dot{V}_f\right]\left[32016.15 + \frac{9461.68}{0.648\alpha + 750(1-\alpha)}\right]\end{aligned}$$

After simplifying the following results:

$$\rightarrow \dot{Q} = \dot{V}_f \left(24021572.9 - 23991366\alpha\right) \quad (8)$$

Now, according to the relationships above, the equations (5) and (8) and their replacement in the thermodynamic equation (3) to achieve the result are followed as follows:

$$\dot{Q} = (\dot{U}_u - \dot{U}_u) + \dot{w}$$

$$\dot{V}_f\,(24021572.9 - 23991366\,\alpha) = \left[577.98 \times 10^{-3} + 9072.185 \times 10^3\,\alpha\,\dot{V}_f\right] + \left(\frac{107424}{4}\right) \quad (9)$$

The importance of this study was that during the test when the engine only operated with diesel fuel, 2.2 cc of diesel fuel was consumed in idle engine speed for 30 seconds. Since one of the goals of the study was to reduce fuel consumption, so in the present study, the dual fuel consumption for 30 seconds considered 2 cc, thus from the previous relationships, the amount of CNG and diesel fuel consumption was calculated. Finally, the ratio of gas to dual fuel (α) was calculated equal to 0.72. This means that CNG makes up 72% and diesel fuel makes up 28% of the dual fuel at idle speed (450 rpm). According to the way of changing the mechanical structure of the governor in this research, with the increase of the rotational speed of the engine, α increased linearly. According to the structure of the engine used in the tests, by changing the mechanical structure of the governor in the injector pump, it was possible to inject a limited amount of diesel fuel as an ignitor in dual fuel mode. In this case, the ignition fuel (diesel) was injected into the compressed CNG in the combustion chamber at the end of the compression stage and combustion took place. In this research, no electronic fuel injection control system was used and fuel injection was completely done mechanically. The innovation and simplicity of the proposed method has been in not changing the structure of the fuel supply system and reducing the cost. Performance tests and pollutants were conducted at the Tabriz Motorsazan Research and Development Center. Figure 1 shows schematic of the components of the performance and the pollution tests of the engine.

The AVL 415S polluting machine was used to measure the contaminants from the combustion of the tested engine. This device is a product of AVL Ditest, manufactured by Germany and is capable of measuring the combustion products of spark ignition and compression ignition vehicles. This device can measure NO_X, HC, CO, O_2 and CO_2 digitally. The exhaust gases from the engine exhaust were transferred to the device by a pipe and the amount of each pollutant was measured separately by the device.

All performance and emissions tests were performed after 10 minutes of working in an idle engine speed mode and tests at five rotational speeds of 1200, 1400, 1600, 1800 and 2000 rpm and in two modes of diesel fuel and dual mode. The performance test was done in such a way that first the engine was started with diesel fuel and then the tests were performed in three repetitions to check the reproducibility of the tests. After completing the engine test in diesel mode, the tests were performed for the dual fuel mode in three repetitions. In order to analyze the data obtained from the performance and emission tests, the data were drawn as graphs by Excel software. In this research, data analysis was done by direct comparison method.

Results and Discussion

Effect on torque

The torque analysis for both diesel and dual fuel (diesel as igniter and compact natural gas as main fuel) modes at various engine speeds was shown in Figure 2.

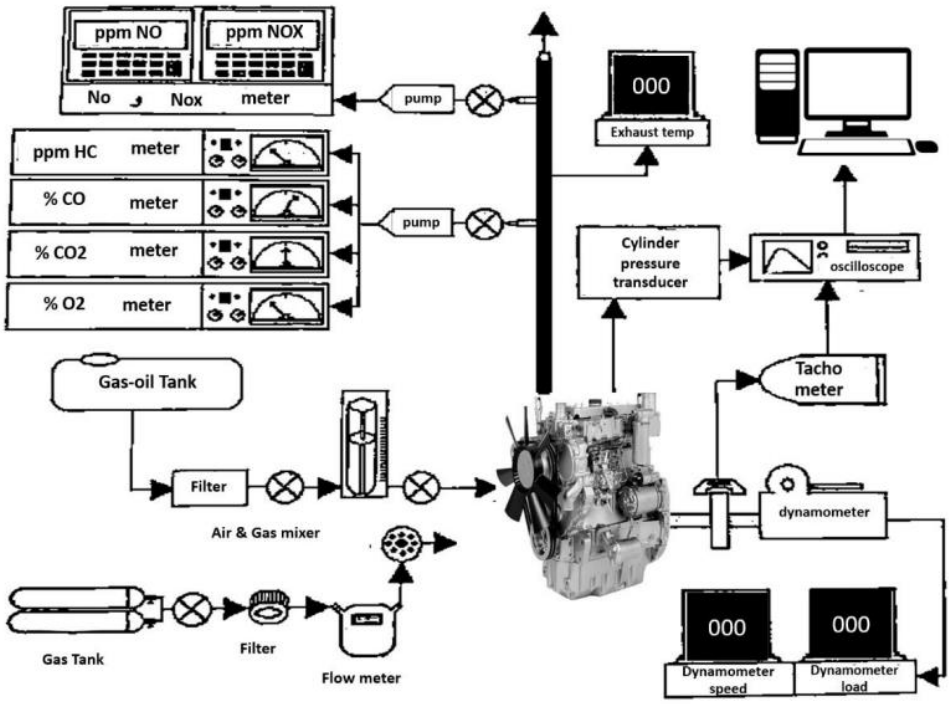

Fig. 1. Scheme of components of performance tests and engine pollution

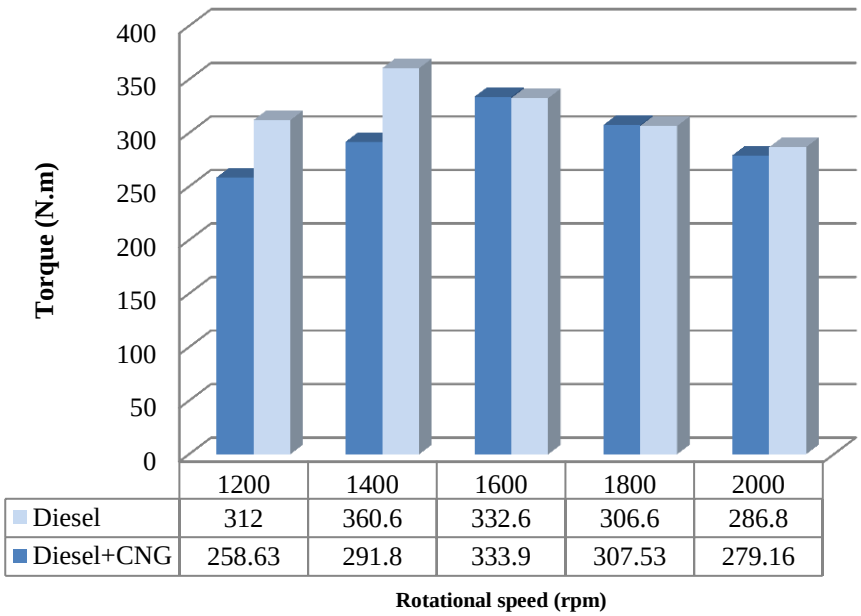

Fig. 2. Variation of torque for two modes at different engine speeds

According to the Figure 2, at diesel mode the maximum torque was 360.6 N m at 1400 rpm. While at dual fuel mode, corresponding maximum torque was 334 N m at 1600 rpm. It can be observed that maximum torque take place at higher speed than diesel mode and this shows the effect of diesel fuel injection system (as igniter) in low speeds (the amount of injected fuel and diesel injection timing on combustion timing can be noticeable).

The average value of torque achieved was 312 and 258.63 N m by diesel fuel and the dual fuel at 1200 rpm, respectively. Also, the average value of torque achieved by diesel fuel and dual fuel was 360.6 and 291.8 N m at 1400 rpm, respectively. From the analysis of torque, there is an average reduction of 54 N m and 68.2 N m in torque for the dual fuel at 1200 and 1400 rpm, respectively. On the other hand, for engine speeds above 1400 rpm (from 1600 to 2000 rpm), there is no remarkable difference in the torque of dual fuel mode and diesel.

The maximum torque in both modes was achieved at different engine speeds. Therefore, brake power was calculated from torque data at the indicated speed of engine (2000 rpm). The BP of engine is 80.47 and 78.33 hp for diesel mode and dual fuel mode, respectively. According to the obtained results, the BP with diesel fuel was 6.15 hp (7.6%) more than the dual fuel at 2000 rpm.

As mentioned the maximum torque in both modes was achieved at different engine speeds. Therefore, brake power was calculated from torque data at the indicated speed of engine (2000 rpm). The BP of engine is 80.47 and 78.33 hp for diesel mode and dual fuel mode, respectively. According to the obtained results, the BP with diesel fuel was 6.15 hp (7.6%) more than the dual fuel at 2000 rpm. it is clear that BP of dual fuel mod is close to that of the diesel mode. It seems in dual fuel mode the more amount diesel fuel and advance injection time aid the combustion process, which prevents BP reduction. By decreasing the engine speed, BP reduces, which is mostly due to the impossibility of advance fuel injection and this is due to the mechanical nature of fuel injection, which is unable to provide a linear process throughout its working range.

This result is consistent with the research results of Yousefi *et al*, (2017) in which the thermal efficiency of a compression ignition engine with the use of dual fuel and in different ignition fuel injection timings was investigated.

Diesel fuel consumption in dual fuel mode and diesel mode

Figure 3 shows the amount of diesel fuel consumption in the dual fuel and diesel mods, at various engine speeds.

According to Figure 3, the amount of diesel fuel consumption in the dual fuel mode at engine speeds lower than 1600 rpm was relatively low. In comparison with diesel fuel consumption in the diesel mode, about 75.7% (1200 rpm), 77.5% (1400 rpm) and 72.08 % (1600 rpm) reduction was observed.

For all engine rotational speed conditions, an average of about 65% reduction in diesel fuel consumption was achieved. The reason for this reduction in diesel fuel consumption was the use of natural gas fuel as the main fuel and the use of diesel fuel as ignition fuel.

The result shows enhancement of diesel fuel consumption of both modes by increasing engine speed, which are almost the same for both modes. From the engine speed 1200 rpm to 2000 rpm, the diesel fuel consumption achieved by dual fuel mode was 4.78 kg h^{-1} and the diesel mode was 4.8 kg h^{-1}.

Based on the results of diesel fuel consumption analysis, the enhancement in the diesel fuel consumption by increasing engine speed was observed in the dual fuel mode that confirm the significant effect of amount and timing diesel fuel injection as igniter on the torque of engine. It should be noted that power improvement in the dual fuel mode is related to sufficient availability of diesel fuel as igniter in combustion by increasing engine speed (according to the engine speed and load, the amount of diesel fuel as igniter was adjusted using mechanical changes in the governor). Therefore, the mechanism used

regulate diesel fuel injection aids the combustion process, which is in line with the research results of Yusefi *et al*, (2017).

CNG fuel consumption

The amount of CNG fuel consumption in the mode of using dual fuel was also measured in five different rotational speeds as in other tests, and the result is shown in Figure 4.

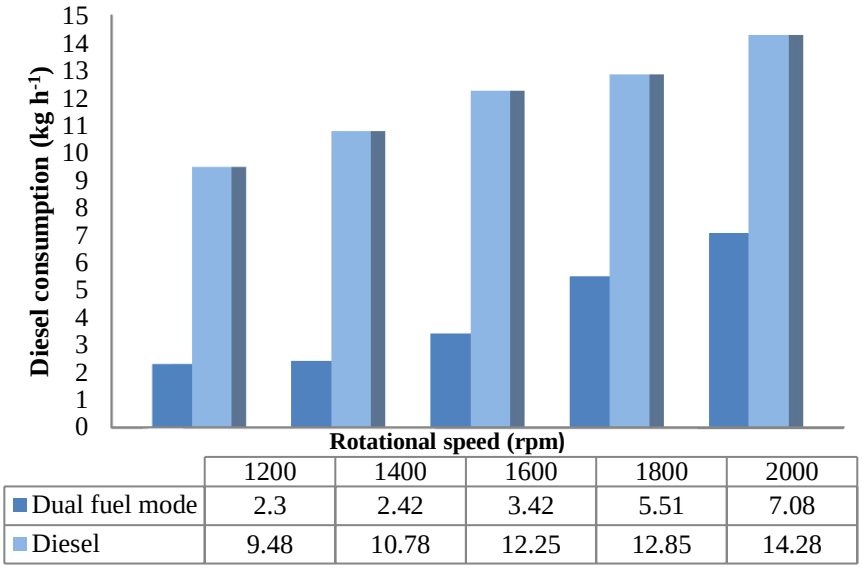

	1200	1400	1600	1800	2000
Dual fuel mode	2.3	2.42	3.42	5.51	7.08
Diesel	9.48	10.78	12.25	12.85	14.28

Fig. 3. Diesel consumption in dual fuel and diesel modes vs. engine speed

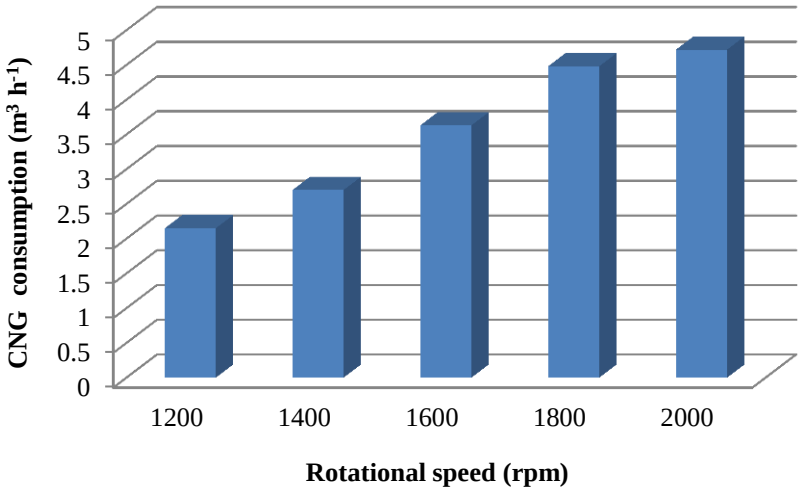

Fig. 4. CNG consumption for dual fuel mode vs. engine speed

CNG fuel was the main fuel in the dual fuel mode. As shown in Figure 4, for the engine speed ranging from 1400 to 1800 rpm, CNG fuel consumption increases. Increasing of the engine speed causes more CNG induction into the engine cylinder through inlet manifold. According to Fig. 2, the maximum torque for dual fuel mode is in 1600 rpm and from 1600 to 2000 rpm, torque reduce slightly. Higher injected CNG fuel quantity would result in enhancement of torque. Consequently, at higher engine speeds torque starts to decrease

when CNG fuel induction into the engine cylinder through inlet manifold decreases.

Specific consumption of diesel fuel in diesel mode

In figure 5, the specific fuel consumption of diesel is displayed, which is presented for five rotational speeds of the engine.

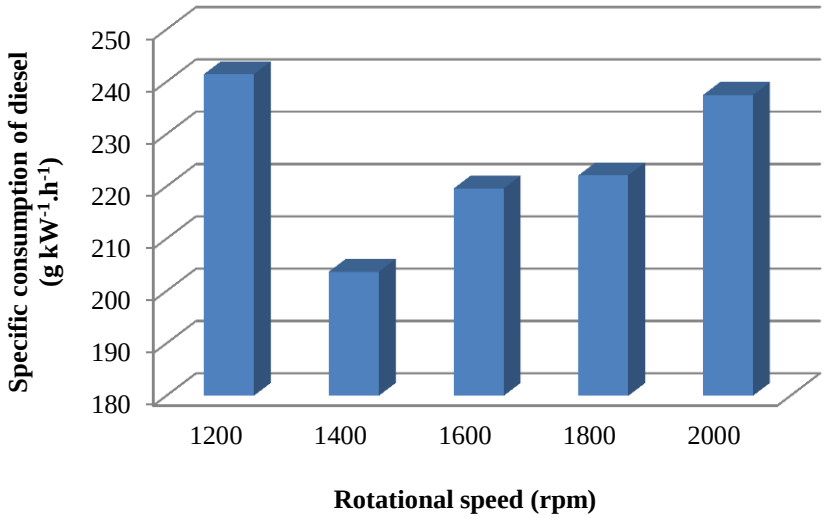

Fig. 5. Specific consumption of diesel fuel in diesel mode vs. engine speed

In Figure 5, the specific fuel consumption of diesel is displayed at different engine speeds. The specific fuel consumption was obtained by dividing the fuel consumption rate by the production power. According to Figure 5, the specific consumption of diesel fuel at 1400 rpm, where the maximum torque produced (Figure 2), was 203.71 g $kW^{-1}.h^{-1}$ (the lowest value the diesel specific consumption and highest torque of engine was observed at 1400 rpm).

The reason that the specific fuel consumption is low at the point of the maximum production torque is that the specific fuel consumption has an inverse relationship with the torque or in other words power.

That is, the higher the production capacity, the lower the specific fuel consumption. Also As shown in Figure 2, with the increase in rotational speed from 1400 to 2000 rpm, the engine torque has decreased in diesel fuel mode. Since specific fuel consumption has an inverse relationship with power (or, in other words, torque), therefore, with an increase in the rotational speed of the engine, the specific fuel consumption has increased. Although some observations (including fuel consumption at a rotational speed of 1200 rpm) cannot be justified.

The specific consumption rate of diesel fuel and CNG in dual fuel mode

Figure 6 shows the specific consumption of CNG fuel and diesel fuel in the dual fuel mode, separately. The minimum the specific consumption of CNG fuel and diesel fuel was obtained at 1400 rpm (under dual fuel mode the maximum increment in torque at 1400 rpm condition was observed).

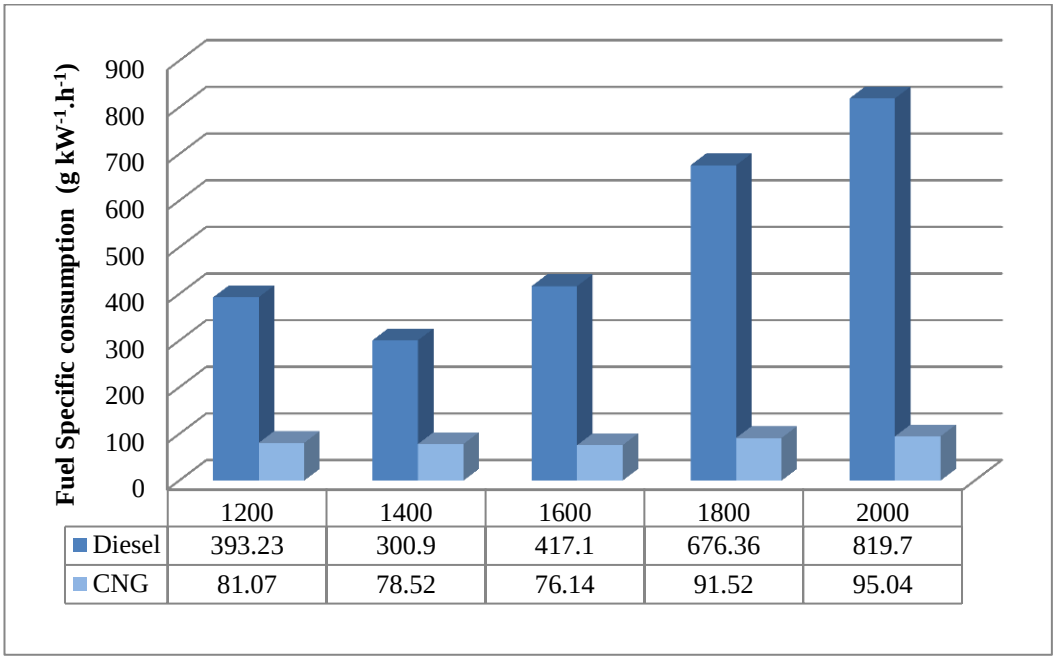

Fig. 6. Specific consumption of dual fuel (diesel + CNG) vs. engine speed

As previously mentioned, in the dual fuel mode, CNG is the main fuel and diesel fuel as an igniter. In Figure 6, with increasing engine speed from 1600 to 2000 rpm the specific consumption of CNG and diesel fuel increased. The lack of proper combustion natural gas-air mixture at high speeds is likely the primary factor influencing proper fuel thermal energy conversion, leading to a reduction in BP. Therefore, it is necessary to modify the mechanical structure of the engine both in the air supply system and in the fuel supply system in order to control this process.

Effect of dual fuel mode on emissions

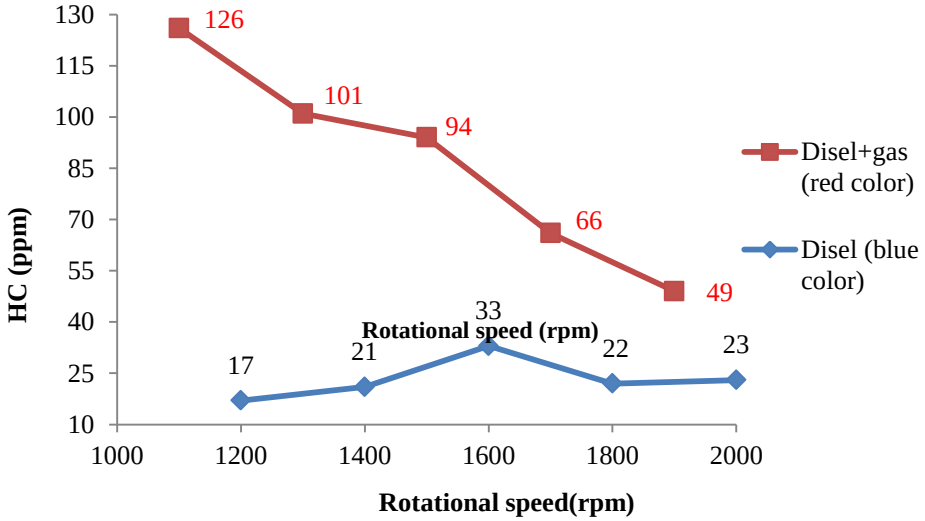

Fig. 7. HC emissions vs. engine speed for diesel and dual-fuel modes

Figure 7 shows the amount of HC emissions of the engine for both diesel fuel and dual fuel modes. According to Figure 7, the amount of HC emissions in dual fuel mode is higher than that of diesel fuel mode. However, the amount of this pollution decreased with the increase of engine speed, which is consistent with the research results of Piroozpanah & Abbas Alizadeh (1998). Rich fuel mixture and incomplete combustion contribute to the formation of unburned hydrocarbon emissions. The amount of unburned hydrocarbon in the case of using dual fuel is due to the richness of the fuel and the incomplete combustion of methane.

Engines that work with CNG fuel (the main part of CNG is methane) produce more HC emissions in partial loads, and the amount of this emissions decreases with the increase of engine load and speed (Yuvenda *et al.*, 2020). It is worth mentioning that the load applied by the dynamometer was proportional to the rotational speed of the engine. By increasing the rotational speed of the engine, the ratio of CNG fuel to diesel fuel (α) increased in the dual system, and as a result, more oxygen entered the combustion chamber, which resulted in proper combustion and a reduction in HC pollutant. In a constant rotational speed, HC emissions increased in dual fuel mode than diese mode. The reduced amount of pure air entering a cylinder caused by the existence of CNG fuel in the cylinder, causing a decrease in volumetric efficiency on dual fuel engine, which has a negative effect on combustion performances and emissions especially carbon monoxide and hydrocarbon which is consistent with the results of Yuvenda *et al,* (2020)'s research.

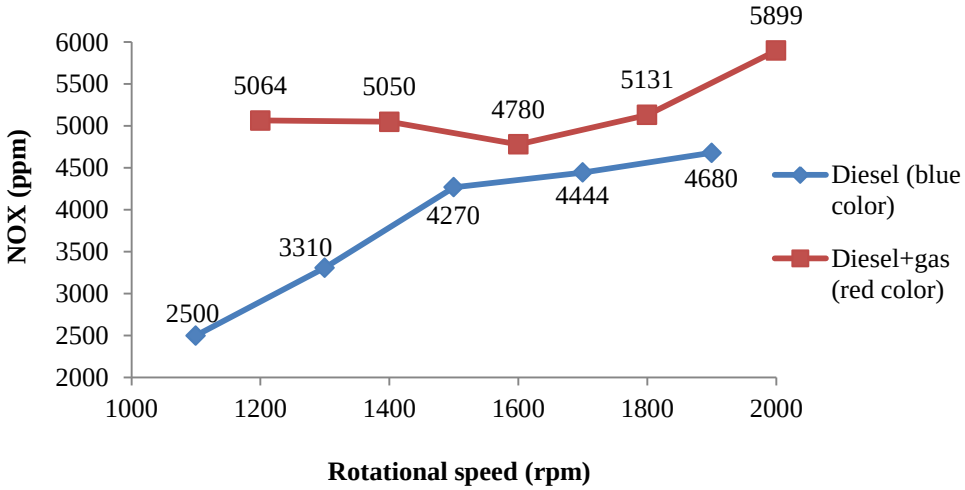

Fig. 8. NO_X emissions vs. engine speed for diesel and dual-fuel modes

Figure 8 shows the amount of NO_X emissions with both diesel fuel and dual fuel modes. According to the diagram in Figure 8, the amount of NO_X produced by the engine was lower in the diesel mode than in the dual mode. Factors such as lean fuel mixture, rich mixture, increased ignition delay time and high combustion temperature contribute to the formation of particulate emissions (Yuvenda *et al.*, 2020). In the dual fuel mode, due to the richness of the fuel and the increase in ignition delay compared to the diesel mode, NO_X production was higher, which is consistent with the research results of Piroozpanah & Abbas Alizadeh (1998) and Yuvenda *et al,* (2020).

The ratio of specific heat capacity of CNG is higher than that of air. Adding CNG

increases the overall heat capacity of the mixture inside the cylinder, accordingly, the average temperature at the end of the compression stroke and during the overall combustion process decreases. Low combustion temperature reduces NO_X formation. CNG injection reduces the amount of air and oxygen concentration in the cylinder charge, and as a result, the possibility of access to oxygen for the formation of NO_X is reduced (Yuvenda *et al.*, 2020). But the release of more heat in the power cycle increases the maximum combustion temperature and this causes an increase in NO_X emissions. Also, since in the dual system, the value of α increased with the increase in the rotational speed of the engine, or in other words, the amount of CNG consumption increased, so the amount of NO_X also increased, which is in line with the results of Karagoz *et al*, (2016) matches.

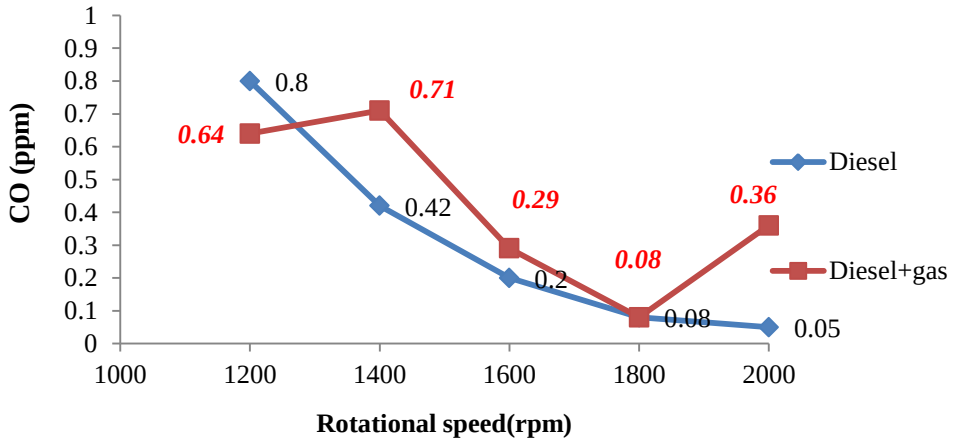

Fig. 9. CO emissions vs. engine speed for diesel and dual-fuel modes

Figure 9 shows the amount of CO emissions for both diesel fuel and dual fuel modes at different speeds. It is clear that increasing the engine speed decreased CO emissions for both modes. It can also be seen that at 1200 rpm, CO emissions showed the lower amount compared to diesel mode. However, compared the diesel mode, the CO emissions increased when the engine speed increased. CO emissions are caused by incomplete combustion of fuel. The most important reason for CO emissions is the use of rich fuel due to lack of oxygen. The reduced amount of pure air entering a cylinder caused by the existence of CNG fuel in the cylinder, causing a decrease in volumetric efficiency on dual fuel engine, which has a negative effect on carbon monoxide. This result has also been confirmed by Yuvenda *et al*, (2020). However, if the combustion temperature is lower than 1450 K, CO can also be produced in a lean fuel mixture (Shadidi *et al.*, 2020). This result is in agreement with the research result of Karagoz *et al.*, 2016; Cheenkachorn, Poompipatpong, & Ho, 2013 is fully compliant.

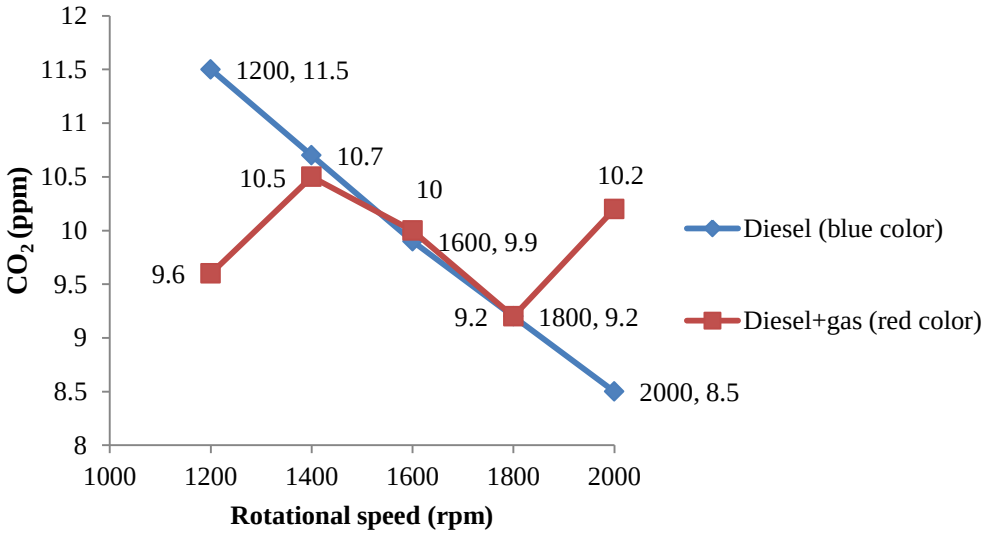

Fig. 10. CO_2 emissions vs. engine speed for diesel and dual-fuel modes

Figure 10 shows the amount of carbon dioxide (CO_2) produced by the engine for the diesel mode and the dual fuel mode. According to the obtained results, the amount of carbon dioxide produced by the engine is almost the same in both modes except in low and high engine speeds, and in lower rotational speeds, the carbon dioxide produced by the dual fuel is less than diesel fuel. Assuming the validity of the test data, the authors did not find convincing reasons for the higher and lower amount of carbon dioxide produced in diesel mode and dual fuel mode at 1200 and 2000 rpm, respectively.

Figure 11 shows the amount of O_2 produced by the engine at different rotational speeds for diesel fuel and dual fuel.

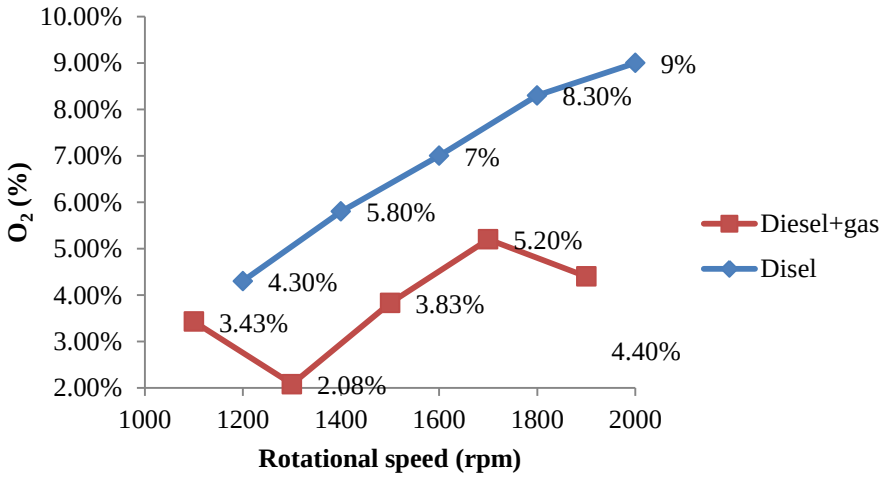

Fig. 11. O_2 emissions vs. engine speed for diesel and dual-fuel modes

According to Figure 11, the amount of O_2 produced by the engine in the mode of using dual fuel is on average 50% lower than the mode of using diesel fuel.

Figure 12 shows the amount of soot produced (output from the exhaust) of the engine for the diesel and dual fuel system. As it can be seen, with the increase in the rotational speed of the engine, the amount of soot emission has decreased in the dual mode which is consistent with the results of Bayat & Ghazikhani (2020)'s research. It seems at higher speeds, the increment in the amount of CNG is one of the main reasons contributing to the decrease in soot emissions. This is in good agreement with the results of Karagoz *et al*, (2016). Also as the CNG substitution ratio is increased, soot emissions get drastically reduced. The reason is the equivalence ratio distribution of air-fuel becomes more homogenous and the local fuel-rich region shrinks with increasing of CNG substitution ratios (Zhouab, Li, & Lee, 2019).

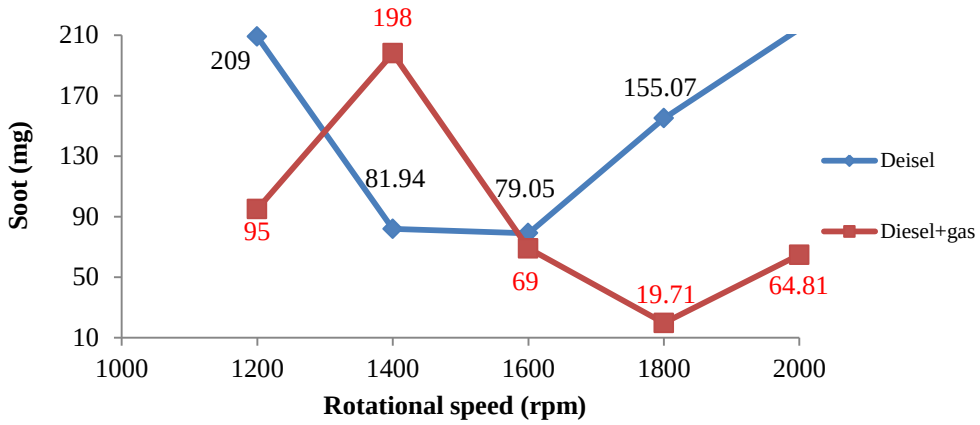

Fig. 12. Soot emissions vs. engine speed for diesel and dual-fuel modes

Conclusion

The effect of a wide range of diesel engine speeds, varying from 1200 to 2000 rpm, on the performance and emissions of a dual-fuel compression ignition engine has been studied, experimentally. Compressed natural gas as the main fuel and diesel fuel as the igniter were used. In this study, a limited amount of diesel fuel as an igniter by a changing the mechanical structure of the governor in the injector pump, to inject in dual fuel mode.

Based on the performance analysis (considering torque and power), no significant difference was observed between the engine performance in dual fuel mode and diesel fuel mode. The maximum torque was 360.6 N m at 1400 rpm. While at dual fuel mode, corresponding maximum torque was 334 N m at 1600 rpm. Results showed only a 26 N m torque reduction in the dual fuel mode. At low speeds (1200 and 1400 rpm), the difference in torque produced by the engine in diesel and dual fuel modes were 53.4 and 68.8 N m, respectively. This difference is due to the fact that at low engine speeds, the amount of diesel fuel injected into the cylinders in diesel mode is close to the stoichiometric state compared to the amount of gas that enters in the form of natural suction in dual fuel mode. On the other hand, it is concluded that diesel fuel injection system (as igniter) in low speeds could be responsible for the reduction of torque. Considering high speeds, there is no remarkable difference in the torque of dual fuel mode and diesel mode.

Regarding the effect of different modes on exhaust emissions, results indicated an increment in the combustion emission including NO_X, HC and CO with a reduction of O_2 and soot emissions for dual fuel mode in comparison with diesel mode. However, effect of both modes on CO_2 emissions had the same trend.

Regarding mechanical injection system to inject igniter in dual fuel mode, there is a critical need for investigation of timing and quantity of fuel injection for better control of emissions. Also, CNG injection system could be considered for further research.

References

1. Ahmadipour, S., Aghkhani, M. H., & Zareei, J. (2021). The Effect of Compression Ratio and Alternative Fuels on the Performance of Turbocharged Diesel Engine by GT-POWER Software. *Journal of Agricultural Machinery, 11*(2), 199-212. https://doi.org/10.22067/jam.v11i2.71613.
2. Assasi, A., Mirzaei, M., & Khoshbakhti Saray, R. (2017). Nonlinear Control of Air path in a Turbocharged Diesel Engine Using Optimization, *Modares Mechanical Engineering, 17*(6), 168-178. (in Persian).
3. Azizi, S. E., Mahdaloui, M., & Hassani, F. (2013). *Investigation of new technologies and reduction of pollutants from motor vehicles*. 1st national conference on air pollution, monitoring, effects and control measures in Iran. Islamic Azad University. (in Persian).
4. Bayat, Y., & Ghazikhani, M. (2020). Experimental investigation of compressed natural gas using in an indirect injection diesel engine at different conditions. *Journal of Cleaner Production, 271*. 20 October. https://doi.org/10.1016/j.jclepro.2020.122450
5. Chala, G. T., Aziz, A. A. R., & Hagos, F. Y. (2018). Natural Gas Engine Technologies: Challenges and Energy Sustainability Issue. *Energies, 11*(11), 2934. https://doi.org/10.3390/en11112934
6. Cheenkachorn, K., Poompipatpong, C., & Ho, C. G. (2013) Performance and emissions of a heavy-duty diesel engine fuelled with diesel and LNG (liquid natural gas). *Energy, 53*, 52-57. https://doi.org/10.1016/j.energy.2013.02.027
7. Karagoz, Y., Sandalc, T., Koylu, O., Dalkilicx, A. S., & Wongwises, S. (2016). Effect of the use of natural gas–diesel fuel mixture on performance, emissions, and combustion characteristics of a compression ignition engine. *Advances in Mechanical Engineering, 8*(4), 1-13. https://doi.org/10.1177/1687814016643228
8. Kurczynski, D., Lagowski, P., & Pukalskas, S. (2019). Nitrogen oxides concentrations and heat release characteristics of the Perkins 1104D-E44TA dual-fuel engine running with natural gas and diesel. *The Archives of Automotive Engineering–Archiwum Motoryzacji*, 84, 2. https://doi.org/10.14669/AM.VOL84.ART9
9. Mirfattah, S. M. (2010). Development policies of gas transportation in other countries. *Journal of Economic Issues and Policies*, (11&12), 43-60. (in Persian).
10. Mohammadi Koosha, A., Piroozpanah, V., Khoshbakht Sarai, R., & Salsbili, M. (2008). Experimental study of the effect of EGR temperature on combustion process, performance and pollution of dual combustion engines at partial loads. *Journal of Technical College, 35*(2).
11. Piroozpanah, V., & Abbas Alizadeh, M. (1998). *Reduction of OM-355 diesel engine pollutants*, Master Thesis, Faculty of Engineering, University of Tabriz.
12. Sabahi, B., Bahrami, H., Sheikhdavoodi, M. J., Safieddin Ardebili, S. M., & Houshyar, E. (2022). Effect of Gaseous Fuels and Coolant Temperature on Performance and Combustion Characteristics of a Low-Speed Single Cylinder Diesel Engine. Journal of Agricultural Machinery, 12(3), 351-366. https://doi.org/10.22067/jam.2021.68089.1007
13. Sajedian, S. Y., Mohammadzamani, D., & Ranjbar, I. (2014). *Design and construction of injection mechanism in injection pump for CNG fuel system on diesel engine*. Master Thesis. Islamic Azad University of Takestan. (in Persian).
14. Saravanan, P., Kumar, N. M., Ettappan, M., Dhanagopal, R., & Vishnupriyan, J. (2020). Effect of exhaust gas re-circulation on performance, emission and combustion characteristics of

ethanol-fueled diesel engine. *Case Studies in Thermal Engineering, 20*, 1006-1016. https://doi.org/10.1016/j.csite.2020.100643

15. Shadidi, B., Haji Agha Alizade, H., Najafi, G., Moosavian, A., & Khazaee, M. (2020). Investigation of performance and exhaust emission of diesel engine in different ratios of lambda coefficient using diesel-ethanol fuel blends. *Journal of Engine Research, 60*(3), 19-28 (in Persian).
16. Sontag, R. E., Borgnakke, C., & Van Wylen, G. J. (2015). *Fundamentals of Thermodynamics*. 5th edition.
17. Yousefi, A., Birouk, & Guo, M. (2017). An experimental and numerical study of the effect of diesel injection timing on natural gas/diesel dual-fuel combustion at low load. *Fuel, 203*, 642-657. https://doi.org/10.1016/j.fuel.2017.05.009
18. Yuvenda, D., Sudarmanta, B., Wahjudi, A., & Muraza, O. (2020). Improved combustion performances and lowered emissions of CNG-diesel dual fuel engine under low load by optimizing CNG injection parameters. *Fuel, 269*. https://doi.org/10.1016/j.fuel.2020.117202
19. Zhouab, H., Li, X., & Lee, C. F. (2019). Investigation on soot emissions from diesel-CNG dual-fuel. *International Journal of Hydrogen Energy, 44*(18), 9438-9449. https://doi.org/10.1016/j.ijhydene.2019.02.012

نشریه ماشین‌های کشاورزی
https://jame.um.ac.ir

مقاله پژوهشی
جلد ۱۳، شماره ۱، بهار ۱۴۰۲، ص ۸۳-۶۷

بررسی تجربی عملکرد موتور و انتشار آلاینده‌ها در یک موتور احتراق تراکمی با به‌کارگیری ترکیب سوخت گاز طبیعی فشرده و دیزل

یاسر نیکنام[۱]، داود محمدزمانی[۲*]، محمد غلامی پرشکوهی[۳]

تاریخ دریافت: ۱۴۰۱/۰۷/۲۴
تاریخ پذیرش: ۱۴۰۱/۱۰/۱۷

چکیده

این مطالعه اثرات سوخت گاز طبیعی فشرده را بر روی یک موتور احتراق تراکمی چهار سیلندر ارائه می‌کند. گاز طبیعی فشرده به‌عنوان سوخت اصلی و سوخت دیزل به‌عنوان آتش‌زنه برای بررسی عملکرد موتور و انتشار گازهای گلخانه‌ای در یک موتور دوگانه‌سوز به‌کار گرفته شد. با توجه به سرعت دورانی و بار موتور، مقدار سوخت دیزل به‌عنوان آتش‌زنه با استفاده از تغییرات مکانیکی در ناظم تنظیم شد، در حالی‌که از هیچ سامانه جرقه‌زنی الکترونیکی استفاده نشد. آزمون‌های تجربی موتور در سرعت‌های دورانی ۱۲۰۰، ۱۴۰۰، ۱۶۰۰، ۱۸۰۰ و ۲۰۰۰ دور در دقیقه با استفاده از سوخت دیزل و دوگانه‌سوز انجام شد. این داده‌ها در مرکز تحقیقات موتور شرکت موتورسازان تبریز جمع‌آوری و آزمون‌ها در سه بار تکرار انجام شد. بیشینه گشتاور موتور در حالت دیزل ۳۶۰ نیوتن‌متر در سرعت دورانی ۱۴۰۰ دور در دقیقه بود. در مقایسه با حالت دیزل، حالت دوگانه‌سوز بیشینه گشتاور را به میزان ۳۳۴ نیوتن‌متر در ۱۶۰۰ دور در دقیقه نشان داد که حدود ۲۶ نیوتن‌متر کمتر از گشتاور به‌دست آمده از حالت دیزل بود. با در نظر گرفتن آنالیز آلاینده‌ها در سرعت مشخصه ۲۰۰۰ دور در دقیقه، مشاهده شد که میزان انتشار NO_X، HC، CO_2 و CO در حالت دوگانه‌سوز به‌ترتیب ۲۰، ۵۳، ۱۶ و ۸۶ درصد بیش از سوخت دیزل بوده است. با این حال، O_2 و دوده بیشترین کاهش را در ۲۰۰۰ دور در دقیقه برای حالت دوگانه‌سوز به‌ترتیب ۵۱ و ۶۹ درصد نشان دادند. این مطالعه نشان داد که هنگامی که تزریق سوخت دیزل به‌عنوان آتش‌زنه به‌صورت مکانیکی انجام می‌شود، افزایش قابل‌توجهی در انتشار گازهای خروجی وجود دارد. در این راستا، کنترل مقدار و زمان تزریق احتمالا می‌تواند به کنترل بهتر انتشار گازهای گلخانه‌ای کمک کند. بنابراین، پژوهش‌های بیشتر در مورد اصلاح سامانه تزریق دیزل به‌عنوان آتش‌زن یا سامانه تزریق CNG به‌منظور کاهش انتشار گازهای گلخانه‌ای مورد نیاز است.

واژه‌های کلیدی: آلاینده‌ها، توان، سوخت دیزل، گاز طبیعی فشرده، موتور احتراق تراکمی

۱- دانشجوی دکتری، گروه مهندسی بیوسیستم، دانشگاه آزاد اسلامی واحد تاکستان، تاکستان، ایران
۲- استادیار، گروه مهندسی بیوسیستم، دانشگاه آزاد اسلامی واحد تاکستان، تاکستان، ایران
۳- دانشیار، گروه مهندسی بیوسیستم، دانشگاه آزاد اسلامی واحد تاکستان، تاکستان، ایران
(*- نویسنده مسئول: Email: dr.dmzamani@gmail.com)

https://doi.org/10.22067/jam.2023.79199.1127

Journal of Agricultural Machinery

Homepage: https://jame.um.ac.ir

Research Article
Vol. 13, No. 1, 2023, p. 85-99

Development and Field Evaluation of a Variable-Depth Tillage Tool Based on a Horizontal Pneumatic Sensor Measurement

M. Tahmasebi[1*], M. Gohari[2], A. Sharifi Malvajerdi[3], A. Hedayatipoor[1]

1- Agricultural Engineering Research Department, Markazi Agricultural and Natural Resources Research and Education Center, Agricultural Research, Education and Extension Organization (AREEO), Arak, Iran
2- Faculty of Mechanical Engineering, Arak University of Technology, Arak, Iran
3- Agricultural Engineering Research Institute, Agricultural Research, Education and Extension Organization (AREEO), Karaj, Iran
(*- Corresponding Author Email: tahmasebi.mona@gmail.com)
https://doi.org/10.22067/jam.2023.79231.1128

Received: 18 October 2022
Revised: 09 January 2023
Accepted: 25 January 2023
Available Online: 25 January 2023

How to cite this article:
Tahmasebi, M., Gohari, M., Sharifi Malvajerdi, A., & Hedayatipour, A. (2023). Development and Field Evaluation of a Variable-Depth Tillage Tool Based on a Horizontal Pneumatic Sensor Measurement. *Journal of Agricultural Machinery*, *13*(1): 85-99. https://doi.org/10.22067/jam.2023.79231.1128

Abstract

Soil compaction can be naturally occurred or can be machinery-induced. Subsoiling is often applied to loosen soil compaction and decrease soil strength to levels that allow for root development and growth. Variable-depth subsoiling which modifies the physical properties of soil only where the tillage is required for crop growth has the potential to reduce labor, costs and fuel, and energy requirements. Since this study aimed to perform subsoiling operations with variable depth, the variable-depth tillage (VDT) tool was developed. A pneumatic multi-nozzles sensor has been used to simultaneously predict the depth of a soil layer in three depths (15, 30, and 45 cm), and send a signal to control the depth of the VDT tool. Evaluation of the VDT tool system was performed by two methods namely static and dynamic tests. In static evaluation, the system response time was measured to reach 95% of the proposed depths. The dynamic evaluation of the tool was accomplished in two steps in the field. The amount of fuel consumption and the travel distance of the tool tine to reach the desired operation depth were measured and compared with the common subsoiler (when the depth control was OFF). The average fuel consumption by using the variable-depth tillage tool decreased by 17.36% compared to the constant depth. Furthermore, the pneumatic sensor tine penetrated into the soil perfectly and sent the control signal to the control unit of the VDT tool in real-time, and the VDT tool loosened the soil at the exact depths sent by the sensor.

Keywords: Compacted soil layer, Fuel consumption reduction, Pneumatic sensor, Precision tillage, Variable-Depth Tillage (VDT) tool

Introduction

Soil compaction affects root growth rate and restricts access to water and nutrients for plants, and hence crop yield. A penetrometer with a conical tip as the standard method has been identified to determine a soil strength index in situ (ASAE, 2002) which is time-consuming and highly variable. In recent decades, several researchers have attempted "on-the-go" measurement of soil strength with horizontal soil resistance tools at multiple depths (Alihamsyah, Humphries, & Bowers, 1990; Adamchuk, Skotnikov, Speichinger, & Kocher, 2003; Chung, Sudduth, Plouffe, & Kitchen, 2004; Koostra & Stombaugh, 2003; Sharifi & Mohsenimanesh, 2012; Khalilian *et al*., 2014; Vernekar, 2015; Meselhy, 2020, Tahmasebi, Hedayatipoor, Gohari, & Sharifi malverjerdi, 2021).

The negative impacts of soil compaction on crop yields can often be removed by subsoiling. Though, this subsoiling operation is often conducted at unnecessarily deep depths wasting energy and excessively

loosening surface residue essential for erosion control and alleviating soil quality (Raper, Reeves, Shaw, van Santen, & Mask, 2007). Different soil tillage operations are implemented to decrease soil compaction. In conventional methods, subsoiling requires a high-energy input to loosen the hardpan layer which causes to lack of farmers' interest to do it. A number of the researchers reported that a reduction in tillage depth could save producers significantly if soil compaction was still eliminated (Raper, 1999; Fulton, Wells, Shearer, & Barnhisel, 1996).

Advances in precision agriculture prepare capabilities to vary soil treatment across an agricultural field (Adamchuk, Skotnikov, Speichinger, & Kocher, 2004). Site-specific tillage can modify soil physical properties where the tillage is required for plant growth. Therefore, it attains significant savings in fuel consumption and drawbar power requirements. Site-specific tillage can be accomplished with (1) a real-time sensor or (2) a pre-tillage map technology (Raper *et al*., 2005; Gohari, Hemmat, & Afzal, 2010). Raper (1999) approximated that the energy cost of subsoiling could be reduced by as much as 34% using variable-depth tillage against uniform depth tillage.

In a study, a device was developed which calculated the proper position of tillage tools relative to the land surface at each point, and the hydraulic operator set its optimum position. The optimum position of tillage tools is calculated by depth control software established for this device, and its input data were depth for root development. Precision deficiency for laboratory tests was 3.3% and 3.83% for depth increasing and decreasing depth, respectively (Fallahi, Aghkhani, & Bayati, 2015).

In another study, it is stated that consumption of fuel could be decreased by 50% via site-specific tillage in comparison to subsoiling the field (Fulton *et al*., 1996). Also, Raper *et al*. (2007) reported a 35 and 59% major reduction in draft force, and a 27 and 43% reduction in fuel consumption for site-specific subsoiling in medium (35 cm) and shallow (25 cm) depth hardpan plots in comparison to uniform deep (45 cm) subsoiling in the same plots. The concept of variable-depth tillage was investigated by several researchers (Raper, 1999; Gorucu, Khalilian, Han, Dodd, & Smith, 2006; Gohari *et al*., 2010; Gohari, 2006). Khalilian *et al*. (2002) demonstrated that variable-depth tillage results in a fuel-saving of 28% and an energy savings of 43% as compared to uniform-depth tillage. In another research, GPS-based variable-depth tillage equipment has been developed and validated in the laboratory and the field (Gohari *et al*., 2006).

Fox *et al*. (2018) developed an "intelligent Plow" which was a system that mount directly on the tractor and continuously measure the depth to the hardpan and adjust the tillage depth. The system not only measured soil compaction data and calculate the depth and thickness of the hardpan layer but also adjust tillage depth on-the-go in real-time. The finding demonstrated that variable-depth tillage operations, reduced fuel consumption by 45% compared to conventional constant-depth tillage.

An experiment was performed in a field to evaluate a technology to determine the tillage depth based on soil penetration resistance at soil different depths. The field experiment area was divided into five plots including no-tillage; uniform-depth tillage at 25, 35, and 45 cm tillage depth; variable-depth tillage. The results presented that the variable-depth tillage system caused a reduction in the fuel consumption rate, power requirements, and operating costs by about 35%, 35%, and 23%, respectively, in comparison to the uniform-depth tillage system, while the actual field capacity for variable-depth tillage system increased about 21% compared to uniform-depth tillage system (Meselhy, 2021).

As mentioned before, uniform-depth tillage applied by the farmers needs fuel costs and higher energy. Variable-depth tillage could be useful in improving production costs. The primary aim of this research was to know if the variable depth tillage is feasible. Besides, the specific objectives of this research were:

- To develop a two-tine tool equipped with variable-depth tillage instruments
- To evaluate variable-depth control of the proposed tool using an on-the-go pneumatic sensor
- To investigate the performance of variable-depth tillage compared to conventional uniform depth tillage
- To determine the effects of variable-depth tillage on fuel and energy consumption.

Materials and Methods

Since the aim of this project was to develop a system that will mount directly on the tractor and continuously measure the depth to the compacted layer and adjust the subsoiling depth. The proposed system should be able to measure soil compaction data, calculate the depth, and adjust subsoiling depth on-the-go for real-time, variable-depth, tillage operations for crop production. This was accomplished by combining two systems "horizontal pneumatic sensor" and "Variable-Depth tillage" described below.

System design

In the first step, the mathematical calculation to design a tine for variable-depth tillage (VDT) was done. Based on the main tine design of the horizontal pneumatic sensor mentioned (Tahmasebi *et al*., 2021), the tine dimensions of the VDT tool were considered the same as the pneumatic sensor. The shape of the tines was considered vertical and the dimensions were 60*10*2 cm. Then, the tine was modeled in ANSYS software and the stresses and strains are displayed in Fig. 1. The tine was fully fixed at the end edge as a boundary condition, and soil pressure was exposed on the tine by triangle distribution. A 3D triangle mesh with 6 nodes was used for meshing the object via a meshing tool, and the problem was solved by software. As can be seen, the maximum stress was 617Mpa at the end of the tine, the connection point to the chassis which was less than the steel yield stress (Fig. 1a). Since the desired steel was SPK, and by considering a safety coefficient of 1.5, the Von Mises stress was less than the yield stress of the selected steel (1000Mpa). Also, the strain of the tine is presented in Fig. 1b and the degree of deflection of the tine in the face of the soil force was apparent. This finite element method (FEM) results confirmed that the designed structure can work in considered conditions without the probability of failure in the main parts.

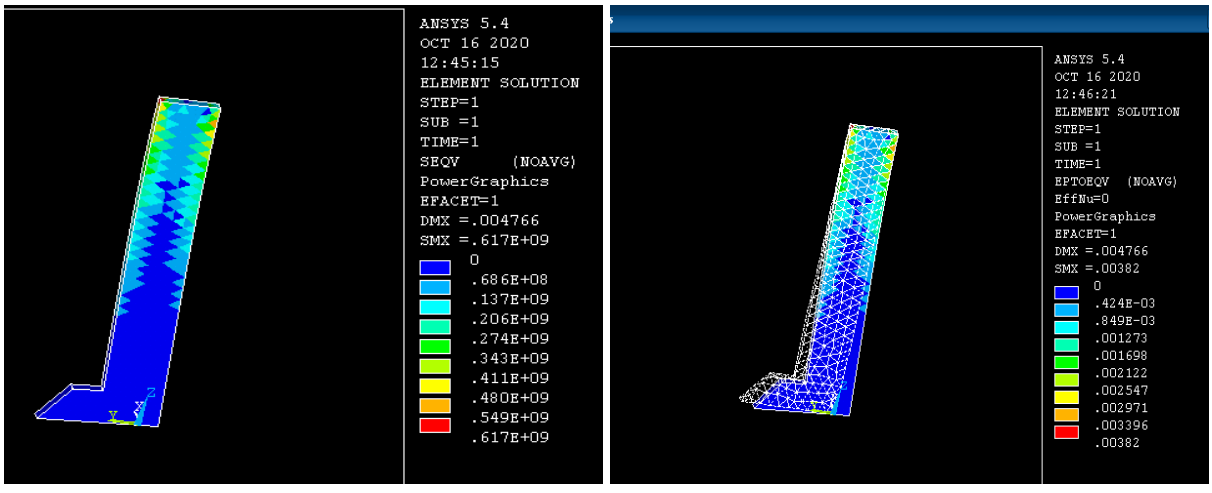

a b

Fig. 1. a) The stresses and b) strains of the VDT tool tine in the ANSYS software

Secondly, an instrumentation system for VDT has been developed and tested (Fig. 1). The main components of the instrumented system consist of 1) main chassis and three-point hitch, 2) tine, 3) wheels and wheel axles, 4) double-sided cylinder, 5) 4/3 Directional

control valve, 6) Electric motor pushing hydraulic valve lever, and 7) Shaft encoder (Fig. 2). A horizontal pneumatic sensor was used to measure the mechanical strength of soil at different soil depths (Tahmasebi *et al*., 2021). The pneumatic sensor equipped with three nozzles with a diameter of 10 mm at three depths of 15, 30, and 45 cm was installed on a tine in front of the tractor to inject air flow into the soil, and the resistance to air permeability into the soil was measured simultaneously.

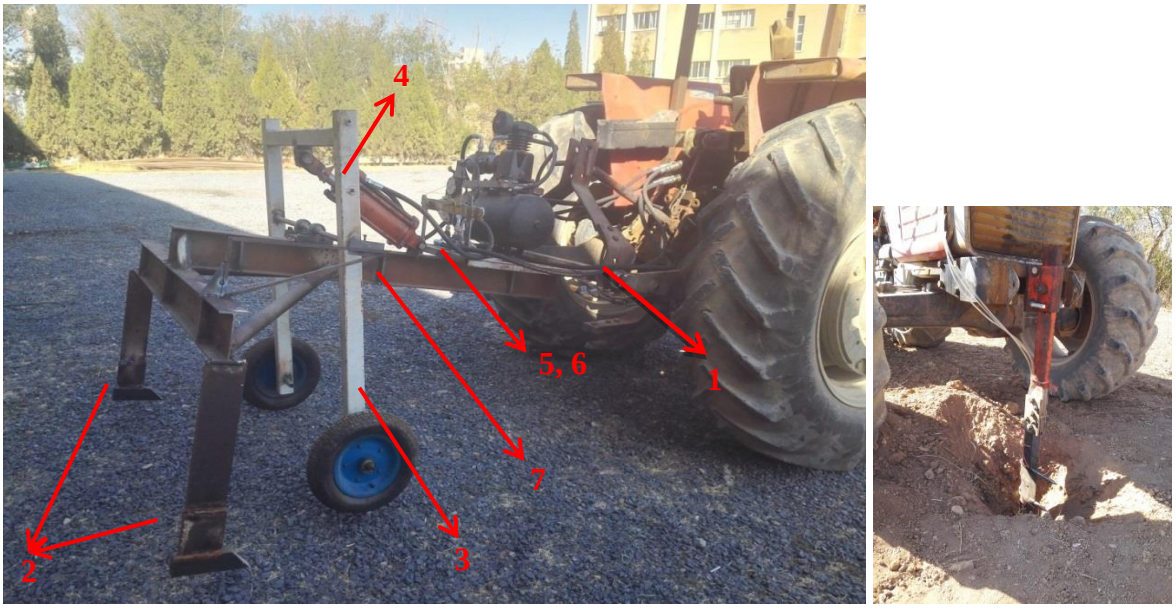

a b

Fig. 2. a) View of VDT tool; 1) main chassis and three-point hitch, 2) tine, 3) wheels and wheel axles, 4) double-sided cylinder, 5) 4/3 Directional control valve; 6) Electric motor pushing hydraulic valve lever, and 7) Shaft encoder; b) the pneumatic sensor

In addition, the structure of the VDT tool was modeled in CATIA software which is shown in Fig. 3. It is assumed that the front edge of the tine is perpendicular to the soil surface during operation. The tine was designed with a height of 60 cm while the depth was 45 cm. Since the pneumatic sensor was installed in the front and middle of the tractor, two tines with a distance of 1.5 meters from each other were used for the proposed VDT tool.

System fabrication

After the system design, the proposed VDT tool has been fabricated. Two gauge wheels connected to the hydraulic cylinder were used to adjust the depth of the tools. The VDT tool was connected to the three-point hitch of the tractor (ITM 399).

The maximum depth of the tines was about 45 cm and operation depth ranged from 0 to 45 cm. In order to automatically control the depth of the VDT tool, the opening of two wheels' axle has been controlled by a double-sided hydraulic cylinder with a stroke of 25 cm and a control circuit. The extending speed of the hydraulic cylinder was equal to 0.01 ms^{-1}, and this is due to the existence of multiple orifices and cross-sectional changes in the inlet and outlet of the valve, cylinder, and coupling couplings. The pneumatic sensor including three nozzles installed at three depths of 15, 30, and 45 cm on the sensor tine was used to predict the depth of a soil layer simultaneously (Tahmasebi *et al*., 2021).

Variable-depth tillage tool pneumatic circuit

The pneumatic circuit diagram for sending the depth control command to the VDT tool system is schematically shown in Fig. 4. All three nozzles injected air into the soil until each of their contact with the hard layer and

the pressure inside the pipe connected to it raised above 1.2 bar (threshold).

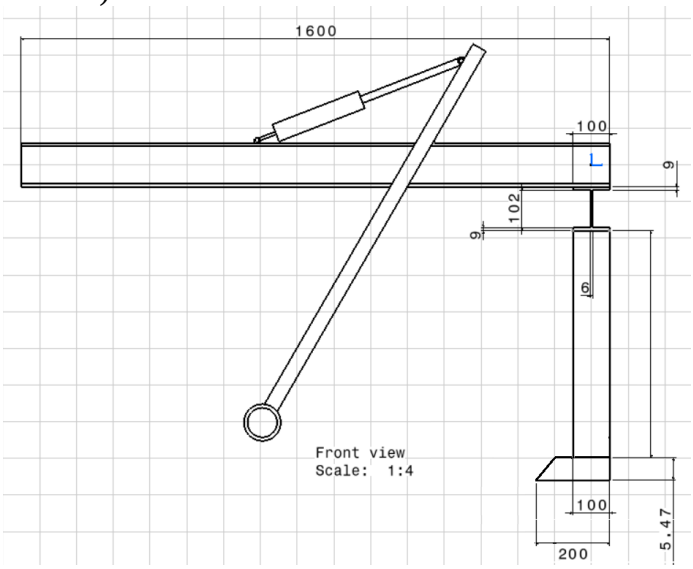

Fig. 3. The initial design of variable-depth tillage tools (units in mm)

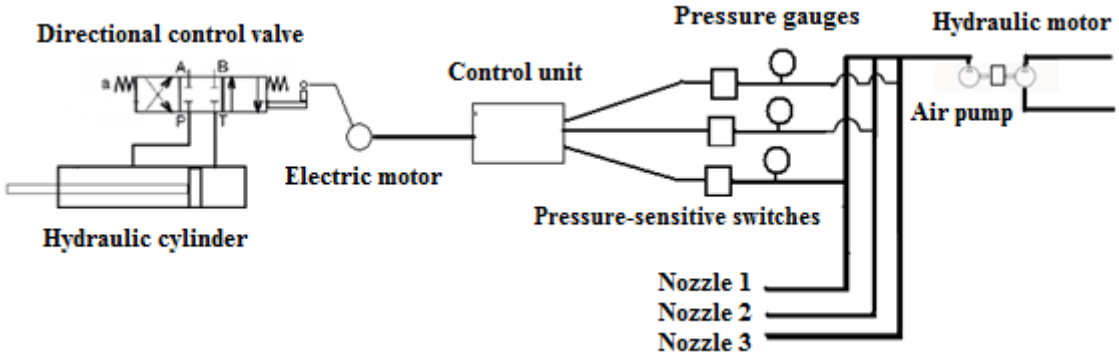

Fig. 4. The pneumatic circuit to send the depth control signal to the VDT tool, including hydraulic motor; Air pump; Pressure gauge; Pressure-sensitive switches; Control unit; Electric motor; Directional control valve, Nozzles, and hydraulic cylinder

At this time, the pressure-sensitive switch that its connection pressure was adjusted to 1.2 bar, was activated and sent the electric current to the electric motor control system that moves the 4/3 Directional control valve. The instrumentation system included three pressure-sensitive switches (RMP-8, one-way with a pressure range of 40-175 psi) as presented in Fig. 5. The lever of the directional control valve was also moved by the control unit, which was closing the hydraulic cylinder connected to the depth control wheel, hence increasing the working depth (Fig. 6). According to the results of Taylor and Gardner (1963) and Alimardani, Abbaspour-Gilandeh, Khalilian, Keyhani, & Sadati, (2007) researches, the threshold of soil compaction based on the cone index is 2 MPa. Therefore, this value according to the research of Clement (2000) and Koostra & Stambuc (2003) was transformed to a threshold air pressure of 1.2 bar for pressure-sensitive switches.

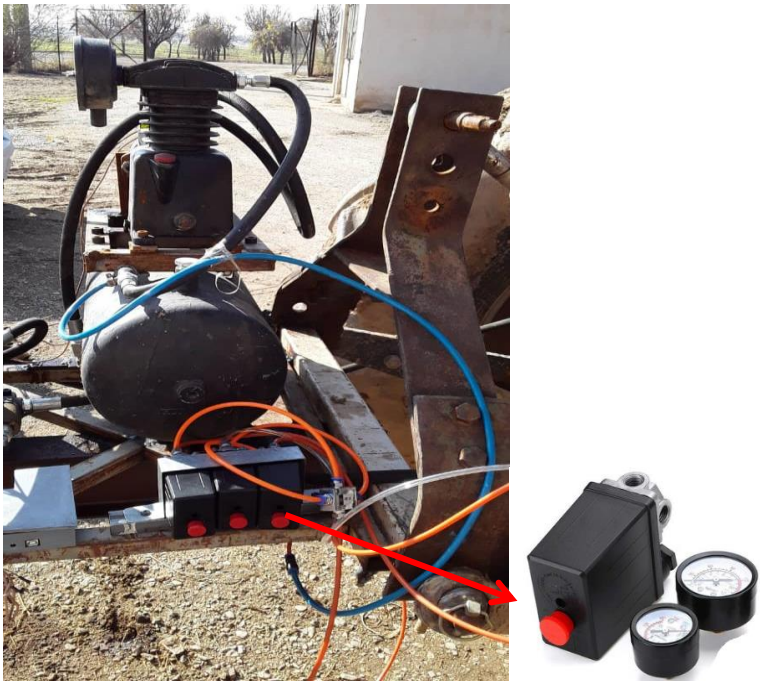

Fig. 5. The pressure-sensitive switches

a b

Fig. 6. a) Electric motor system moving the directional control valve lever; b) 4/3 Directional control valve

Variable-depth tillage tool control unit

As mentioned before, in order to actively control the extending and closing of the cylinder to the desired value, an electronic control unit was developed. In fact, the controller works by settled values, and the type of controller was a lookup table. The operating principles of this circuit are based on the

closed-loop and the feedback signal sent from the displacement of the gauge wheel arm, which is shown in the block diagram in Fig. 7. The proposed control circuit consisted of an Arduino (Uno) control board which was programmed. A drive circuit and a voltage regulator were also used to bring the output of the pressure-sensitive switches output to the readable voltage level in the Arduino (Fig. 8). To monitor the depth control and send a feedback signal to the control unit, a 30-pulse rotary shaft encoder (KY-040) was employed to send the instantaneous depth of work by the depth wheel to the control system. Fig. 9 shows the encoder module and installation location on the chassis. A 12-volt electric motor was applied to open and close the 4/3 directional control valve which received the control signal from the control circuit.

Evaluation

Initial testing of the instrumentation system for variable-depth tillage was performed in two phases namely static and field evaluations which will be explained in later sections.

Static evaluation

In the first phase, the static test was accomplished at three depths of 15, 30, and 45 cm, and the control signal was sent to the system and each test was repeated three times. Delay time, rise time, and response time to reach the depth of 95% of the desired depth were obtained by the gyroscope sensor. Angle data of the depth control wheel were acquired after noise filtering by Wavelet Transformation.

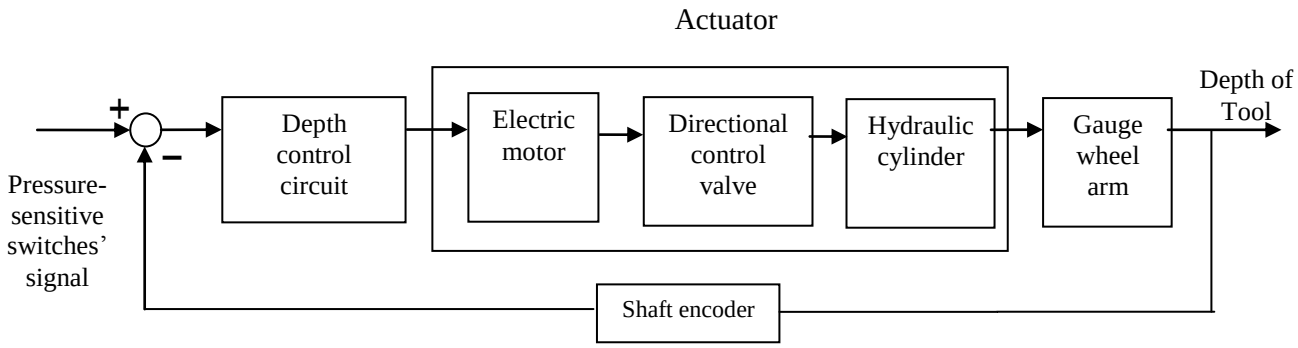

Fig. 7. Block diagram of the control system

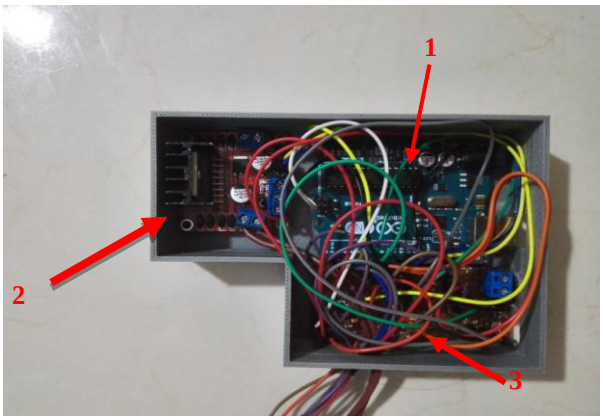

Fig. 8. Electronic control circuit system: 1) Arduino board, 2) Drive circuit, 3) Voltage regulator of pressure-sensitive switches of the pneumatic sensor

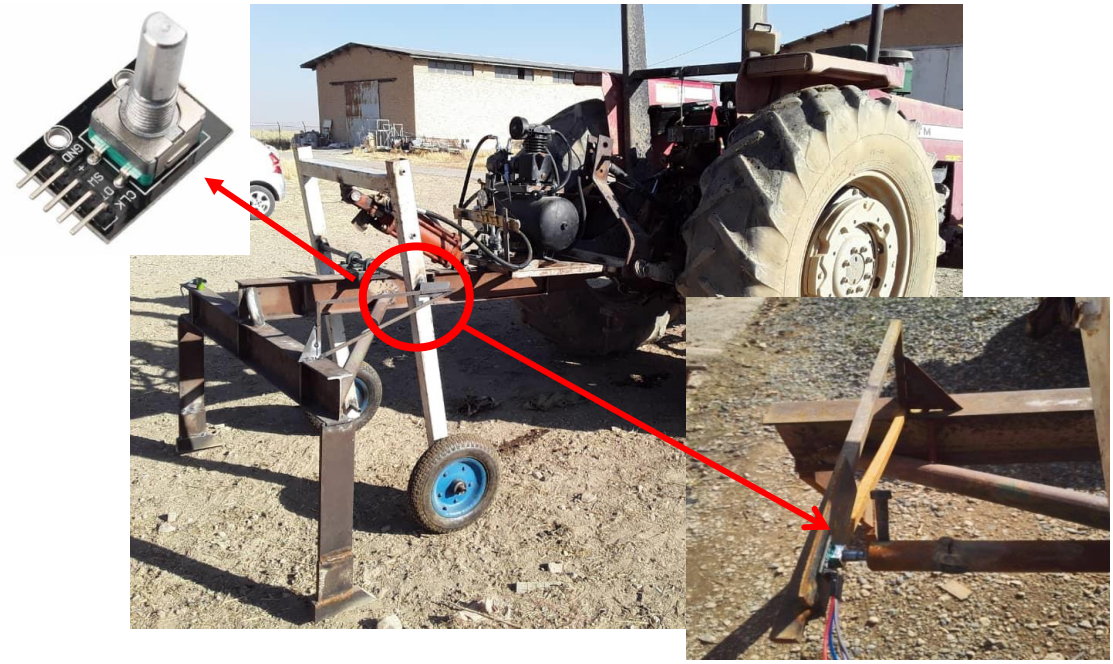

Fig. 9. Shaft encoder and its installation position

Field evaluation

In the second phase, a dynamic test has also been performed in two steps on a no-till field (Markazi Agricultural and Natural Resources Research and Education Center, Iran). A length of 90 m was selected for the main plot which was divided into three subplots of 30 m in length which every 30m was considered a repetition. The soil texture of the field was clay loam and the soil moisture content and bulk density were measured at the three proposed depths in 3 repetitions and the mean values are reported in Table 1 (Tahmasebi *et al*., 2021). A pneumatic sensor was installed in front of the ITM399 tractor for the determination of soil compaction, and a VDT tool was installed behind the tractor.

As stated in (Tahmasebi *et al*., 2021), a vertical standard penetrometer of the Hand penetrometer Eijkelkamp model (using cone No.1 with a diameter of 1 cm and cone angle of 60 degrees) was applied to measure soil compaction. Vertical penetration resistance was measured up to a depth of 45 cm at 9 points (3 points at a distance of 10m) near the movement path of the system.

Table 1- Some soil characteristics such as moisture content and bulk density

Depth (cm)	0-15	15-30	30-45
Moisture content (%)	5.42	6.68	2.75
Bulk density (g cm^{-3})	1.55	1.63	1.59

The first test was the evaluation of the variable-depth system when the pneumatic sensor did not send a signal. In the conducted experiment, the depth control system sends a command to the tool to reach into identified depths (three depths of 15, 30, and 45 cm). For the experiments, three plots with a width of 3m and a length of 30m for three proposed depths according to Fig. 10 were selected as 3 repetitions. In this case, the amount of fuel consumption and the travel distance to reach the desired depth of the VDT tool was measured in three repetitions. The fuel consumption was determined in each treatment by measuring the volume of tractor fuel consumed. Firstly, the fuel tank of the tractor

was filled full, and the subsoiling operation was performed. Then, the fuel tank was refilled, and the consumed fuel was measured via a graduated cylinder.

The VDT tool's performance when the depth control was OFF (as a common subsoiler) was compared with the VDT tool in terms of energy consumption in a plot with a width of 3m and a length of 90 m (Fig. 10). For this purpose, the VDT tool was worked with a constant depth of 45 cm (maximum). The T-test at the statistical level of 1% was utilized to compare the values of the fuel consumption in two subsoiling methods with variable and uniform depths.

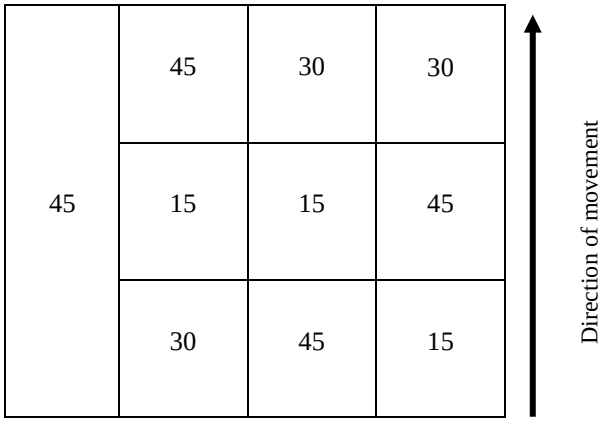

Fig. 10. Evaluation map of VDT tool in the field

The second test was the performance of the variable-depth system while the pneumatic sensor determined the soil compaction, and sends a signal to control depth. The accuracy of operations with variable depth and commanding from the pneumatic sensor and the simultaneous validation of the operation were evaluated. Along the 90m path every 1m interval, the depth of penetration was measured and the profile of the path subsoiling was drawn. For validation of the profile, every 5 m (near the penetrometer point) all over the path the soil was dug up, and the tillage depth was measured by a ruler. Moreover, the fuel consumption along the path was measured by the full fuel tank method.

Results and Discussion

Static evaluation

Fig. 11 illustrates an example of determining the response time of the hydraulic circuit to the open-closed signal applied to the directional control valve. This curve demonstrates the variation in the angle of the depth control wheel from 90 to 60 degrees (30 degrees of rotation), which indicates the change in depth from zero to 30 cm. The horizontal axis of the diagram shows the number of samples per time, and according to the test response time, delay time and rise time were calculated. The values of response time, delay time, and rise time for different depth changes were achieved, and are listed in Table 2. The system accuracy or standard error percentage was computed from Equation (1) and the results are displayed in Table 1.

$$E\% = \frac{D_{\max imum} - D_{s\tan dard}}{D_{s\tan dard}} \times 100 \qquad (1)$$

Where $D_{\max imum}$ and $D_{s\tan dard}$ are the maximum depth measured in each repetition and desired depth, respectively.

It can be seen in Table 1 that the delay time is less through the opening of the hydraulic cylinder compared to closing because of the larger cross-section of the cylinder when is extending. When the setting depth is 0 to 15 cm, the response time is 18.22s.

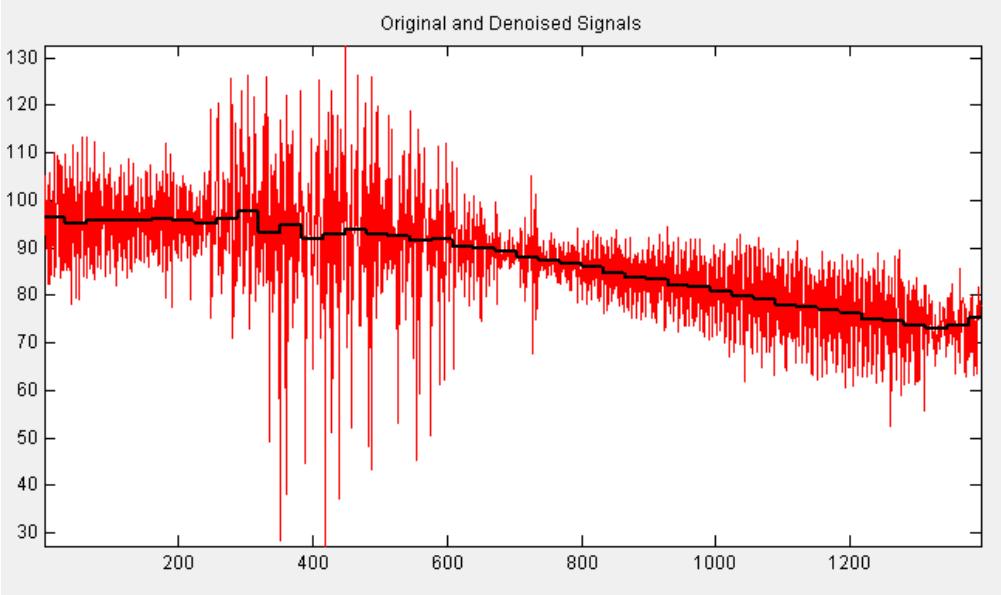

a b

Fig. 11. Diagram of the response of the hydraulic circuit to the open-closed signal applied to the directional control valve; a) The main recorded signal, b) The signal after the noise filtering by wavelet conversion

Table 2- Results of evaluation of VDT tool using a shaft encoder

Setting depth (cm)	Response time (s)	Delay time (s)	Rise time (s)	Error (%)
0 to 15	18.22	4.05	14.17	6.66
0 to 30	27.86	3.98	23.88	6.25
0 to 45	36.72	8.4	28.32	8.33
15 to 30	16.32	4.5	11.82	2.1
15 to 45	15.33	2.06	13.27	5.55
30 to 45	7.5	1.5	6	1.42
45 to 0	41.76	10.44	31.32	6.33
45 to 30	8	1.5	6.5	6.25
30 to 15	13.18	1.68	11.5	2.8
30 to 0	43.2	8.6	34.6	1.3
15 to 0	26.6	4.1	22.5	3.07

But the response time is 27.86s when the setting depth is 0 to 30cm. It is clear that although the desired depth has been doubled, the response is less than twice. That is because of the pressure behind the cylinder piston and the internal friction at the end of the opening path is reduced. In Table 2, a similar trend saw for the third setting depth (0 to 45 cm) that was although the depth has tripled; the response time is less than three times. In addition, by investigation of two other setting depths (15 to 30 cm and 30 to 45 cm), the response time of 30-45 cm depth was half of the 15-30 cm depth is shown that in extending the depth of 30-45 cm, internal friction and pressure are lower, so the resistance inertia is low. Furthermore, Table 2 proved that due to the higher resistance inertia, the error data of extending is higher than the error of closing the hydraulic cylinder

Field evaluation

The results of the VDT tool evaluation in the first stage, including the traveled distance of the tine to reach the desired depth and the amount of fuel consumption, are given in Table 3, respectively. The average values of the traveled distances to get the desired depths

to indicate that the VDT tool can reach the anticipated depth in an appropriate time. The results of static and field evaluations were consistent with the results of Gohari (2006).

According to the results of static and field evaluations, enhancing the performance of the proposed VDT tool requires a hydraulic cylinder with higher extending and closing speeds to have a lower needed open/close time. Another solution for this issue is using a gearbox for gauge wheel axel to increase the speed of wheel deployment.

Table 3- Results of evaluation of VDT tool in the field through the first step

Repetition	Depth			Fuel consumption (L ha^{-1})
	15 cm	30 cm	45 cm	
	Traveled distance to reach the desired depth (m)			
1	0.9	1.6	2.2	67.71
2	1	1.7	2.15	64.40
3	0.9	1.55	2.1	68.19
Mean	0.93	1.62	2.15	66.76

The amount of fuel consumption in the three repetitions of the experiments was 67.71, 64.4, and 68.19 L ha^{-1}, respectively. When the depth control system was OFF, this value was obtained 80.8 L ha^{-1} at the maximum depth of 45 cm. As it is known, the fuel consumption in the variable-depth operation in comparison to the maximum depth in the three repetitions of the experiments had decreased by 16.2, 20.3, and 15.6%, respectively, and the average was 17.36%.

The results of the t-test analysis related to the fuel consumption values in two methods of subsoiling with variable depth and constant depth (as a control) at the statistical level of 1% are displayed in Table 4. The finding showed that the amount of fuel consumption reduction at the statistical level of 1% is significant. Furthermore, the comparison of the mean value of the two methods is given in Table 5.

Table 4- Results of T-test analysis

	Degrees of freedom	t	<p
Fuel consumption	4	-8.46	0.0005

Table 5- Results of comparing the mean amount of fuel consumption in two subsoiling methods with variable depth and uniform depth

Method	Mean of fuel consumption
Subsoiling methods with variable depth	66.76a
Subsoiling methods with uniform depth	80.80b

In fact, the findings of the research indicated that the amount of fuel consumption reduces when the VDT tool is used, which was consistent with other researchers' reports (Fulton *et al*., 1996; Abbaspour-Gilandeh *et al*., 2005; Alimardani *et al*., 2007; Rapper *et al*., 2007; Fox *et al*., 2018; and Meselhy, 2021). However, the percentage of the reduction was lower than the results of their reports, which can be due to two reasons: 1) the pneumatic sensor (in front of the tractor) worked and pushed at the depth of 45 cm in all tests; 2) the soil of the field was highly compacted based on vertical standard penetrometer data (Tahmasebi *et al*., 2021).

In the second phase, when the tool has been operated with variable-depth mode using pneumatic sensor signals, the pneumatic sensor tine penetrated well into the soil and sent the control command to the hydraulic

cylinder continuously. The subsoiling profile by VDT is plotted and shown in Fig. 12. Based on the amount of field compaction (shown in the diagrams of Fig. 21-23 (Tahmasebi *et al*., 2021)), and adjusting the pressure-sensitive switches on 1.2 bar, the tool was worked in the depth range of 30 to 48 cm through the whole test path. However, as clear in the figure, the compaction and the traveled distance by the tool to stabilize the depth were less in the first 10 m of the path. On the other hand, the actual depth of VDT which measured via ruler is depicted in Fig. 12. Comparison between the actual and working VDT depth was confirm that the VDT has been able to perform the subsoiling operation well.

The fuel consumption was measured along a path equaled to 73.7 L ha^{-1}. The rate of reduction of the fuel consumption compared to the control method (subsoiling at the constant depth of 45 cm) showed a decrease of 8.79 %. Although the fuel consumption was decreased during this test, due to the high soil compaction along the path and the operation of the tool at the high depth (45 cm), the fuel consumption was compared only in the first step of the evaluation with the control treatment.

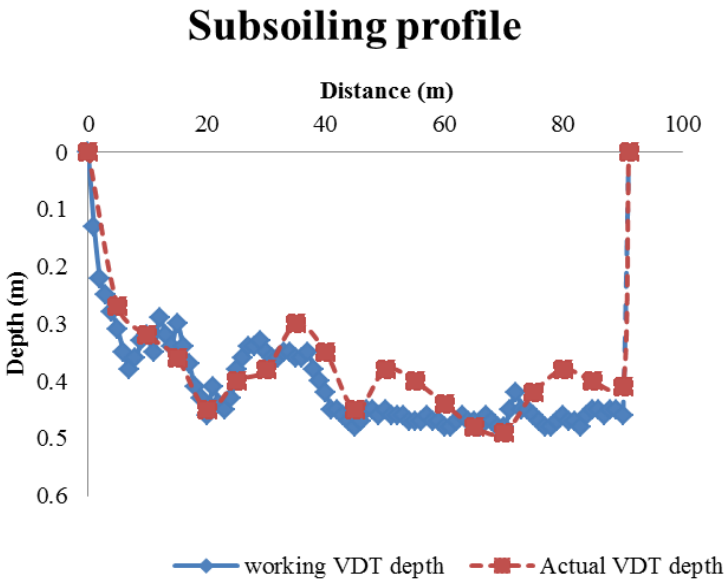

Fig. 12. The subsoiling profile

Conclusion

In this research, a variable-depth tillage (VDT) tool was developed which the working depth was controlled via a signal sent by a pneumatic sensor and evaluated by static and field methods. Through static evaluation, the system response time to reach 95% of the desired depths was measured. Field evaluation of the VDT tool was conducted in two steps. In the first step, the evaluation of the VDT tool was performed when the pneumatic sensor did not send a signal. The amount of fuel consumption and the travel distance to reach the desired depth of the VDT tool tine were measured in three repetitions. To compare the fuel consumption, the VDT tool was worked in the OFF depth control. During the second stage, the VDT tool was evaluated in variable depth using the signals sent by the pneumatic sensor. The mean values of the traveled distances to reach the desired depths indicate that the device can penetrate into the desired depth at a suitable time. The fuel consumption in the variable-depth technique decreased by an average of 17.36% compared to the test maximum depth, and indeed less fuel consumption in the variable-depth subsoiling was perceived. Through the second step of

field evaluation, the sensor tine penetrated the soil perfectly and sent the control signal to the hydraulic cylinder continuously and the VDT tool worked at the depths sent by the sensor.

Acknowledgment

The author also thanks the Markazi Agricultural-Jihad Organization and Markazi Agricultural and Natural Resources Research and Education Center for their assistance.

References

1. Abbaspour-Gilandeh, Y., Khalilian, A., Reza, A., Alireza, K., & Sadati, S. H. (2005). Energy savings with variable-depth tillage. In *Proceedings of the 27th Southern Conservation Tillage Systems Conference, Florence, South Carolina, USA, 27-29 June, 2005* (pp. 84-91). North Carolina Agricultural Research Service, North Carolina State University.
2. Adamchuk, V. I., Skotnikov, A. V., Speichinger, J. D., & Kocher, M. F. (2003). Instrumentation system for variable depth tillage. In *2003 ASAE Annual Meeting* (p. 1). Paper No. 03-1078, American Society of Agricultural and Biological Engineers. https://doi.org/10.13031/2013.13723
3. Adamchuk, V. I., Skotnikov, A. V., Speichinger, J. D., & Kocher, M. F. (2004). Development of an instrumented deep-tillage implement for sensing of soil mechanical resistance. *Transactions of the ASAE*, *47*(6), 1913-1919. https://doi.org/10.13031/2013.17798
4. Alihamsyah, T., Humphries, E. G., & Bowers, C. G. (1990). A technique for horizontal measurement of soil mechanical impedance. *Transactions of the ASAE*, *33*(1), 73-0077. https://doi.org/10.13031/2013.31296
5. Alimardani, R., Abbaspour-Gilandeh, Y., Khalilian, A., Keyhani, A., & Sadati, S. H. (2007). Energy savings with variable-depth tillage a precision farming practice. *American-Eurasian Journal of Agricultural & Environmental Sciences*, *2*(4), 442-447.
6. ASAE Standards, 49th Edition. (2002). S313.2. Soil cone penetrometer. St. Joseph, Michigan: ASAE.
7. Chung, S. O., Sudduth, K. A., Plouffe, C., & Kitchen, N. R. (2004). Evaluation of an on-the-go soil strength profile sensor using soil bin and field data. In *2004 ASAE Annual Meeting* (p. 1). Paper No. 041039, American Society of Agricultural and Biological Engineers. https://doi.org/10.13031/2013.16137
8. Fallahi, I., Aghkhani, M. H., & Bayati, M. R. (2015). Design, construction and evaluation of the automatics position control system of tillage tools. *Iranian Journal of Biosystems Engineering*, 46(2), 117-123 (In Persian). https://doi.org/10.22059/IJBSE.2022.333190.665451
9. Fox, J., Khalilian, A., Han, Y., Williams, P., Mirzakhani Nafchi, A., & Maja, J. M. (2018). Real-time, variable-depth tillage for managing soil compaction in cotton production. In *2018 Beltwide Cotton Conferences*, San Antonio, TX, January 3-5. https://doi.org/10.4236/ojss.2018.86012
10. Fulton, J. P., Wells, L. G., Shearer, S. A., & Barnhisel, R. I. (1996). Spatial variation of soil physical properties: a precursor to precision tillage. *ASAE Paper, 961002*, 1-9. https://doi.org/10.18393/ejss.2016.3.192-200
11. Gohari, M. (2006). *Design, construction and evaluation of a variable depth tillage Subsoiler*. Faculty of Agriculture, Isfahan University of Technology. (In Persian)
12. Gohari, M., Hemmat, A., & Afzal, A. (2010). Design, construction and evaluation of a variable-depth tillage implement equipped with a GPS. *Iranian Journal of Biosystems Engineering*, *41*(1). https://dorl.net/dor/20.1001.1.20084803.1389.41.1.1.0

13. Gorucu, S., Khalilian, A., Han, Y. J., Dodd, R. B., & Smith, B. R. (2006). An algorithm to determine the optimum tillage depth from soil penetrometer data in coastal plain soils. *Applied Engineering in Agriculture*, *22*(5), 625-631. https://doi.org/10.13031/2013.21993
14. Khalilian, A., Han, Y. J., Marshall, M. W., Gorucu, S., Abbaspour-Gilandeh, Y., & Kirk, K. R. (2014). Evaluation of the Clemson instrumented subsoiler shank in coastal plain soils. *Computers and Electronics in Agriculture*, *109*, 46-51. https://doi.org/10.1016/j.compag.2014.09.002
15. Khalilian, A., Han, Y. J., Dodd, R. B., Sullivan, M. J., Gorucu, S., & Keskin, M. (2002). A control system for variable depth tillage. ASAE Paper No. 021209. ASAE, St. Joseph, MI.
16. Koostra, B. K., & Stombaugh, T. S. (2003). Development and evaluation of a sensor to continuously measure air permeability of soil. In *2003 ASAE Annual Meeting* (p. 1). American Society of Agricultural and Biological Engineers, Las Vegas, Nevada, USA. https://doi.org/10.13031/2013.14926
17. Meselhy, A. A. E. (2021). Effect of Variable-Depth Tillage System on Energy Requirements for Tillage Operation and Productivity of Desert Soil. *International Journal of Applied Agricultural Sciences*, *7*(1), 38 https://doi.org/10.11648/j.ijaas.20210701.13
18. Meselhy, A. A. E. (2020). Evaluation of locally made horizontal penetrometer to measure soil compaction under Egyptian conditions. *Bioscience Research, 17*(3): 2331-2357. https://doi.org/10.9734/bpi/nvbs/v7/5028F
19. Raper, R. L. (1999). Site-specific tillage for site-specific compaction: Is there a need. In *Proc. International Conference of Dryland Conservation/Zone Tillage,* Agriculture University, Beijing, China, (pp. 66-68).
20. Raper, R. L. (1999). Site-specific tillage for site-specific compaction: is there a need? In: *Proceedings of the International Conference on Dryland Conservation/Zone Tillage*, China Agriculture University, Beijing, China, pp. 66-68.
21. Raper, R. L., Reeves, D. W., Shaw, J. N., Van Santen, E., & Mask, P. L. (2007). Benefits of site-specific subsoiling for cotton production in Coastal Plain soils. *Soil and Tillage Research*, *96*(1-2), 174-181. https://doi.org/10.1016/j.still.2007.05.004
22. Sharifi, A., & Mohsenimanesh, A. (2012). Soil mechanical resistance measurement by an unique multi-cone tips horizontal sensor. *International Agrophysics*, *26*(1), *61-64*. https://doi.org/10.2478/v10247-012-0009-7
23. Tahmasebi, M., Hedayatipoor, A., Gohari, M., & Sharifi malverjerdi, A. (2021). *Design, Fabrication and Evaluation of Variable Depth Subsoiler Using Pneumatic Sensor*. Agricultural Engineering Research Institute. Report No. 59876. (in Persian).
24. Taylor, H. M., & Gardner, H. R. (1963). Penetration of cotton seedlingn taproots as influenced by bulk density, moisture content, and strength of soil. *Soil Science*, *96*(3), 153-156. https://doi.org/10.1097/00010694-196309000-00001
25. Vernekar, S. R. (2015). *Design and Development of Smart Soil Monitoring System Based on Embedded Technology* (Doctoral dissertation, Goa University). https://doi.org/10.1016/j.procs.2022.10.067

نشریه ماشین‌های کشاورزی
https://jame.um.ac.ir

مقاله پژوهشی
جلد ۱۳، شماره ۱، بهار ۱۴۰۲، ص ۹۹-۸۵

توسعه و ارزیابی مزرعه‌ای یک خاک‌ورز عمق متغیر بر اساس اندازه‌گیری حسگر پنوماتیکی افقی

منا طهماسبی[۱*]، محمد گهری[۲]، احمد شریفی‌مالواجردی[۳]، ابوالفضل هدایتی‌پور[۱]

تاریخ دریافت: ۱۴۰۱/۰۷/۲۶
تاریخ پذیرش: ۱۴۰۱/۱۱/۰۵

چکیده

فشردگی خاک می‌تواند به‌طور طبیعی اتفاق بیفتد یا ناشی از رفت و آمد ماشین‌ها باشد. عملیات زیرشکنی اغلب برای سست کردن لایه تراکم خاک و کاهش مقاومت خاک تا سطوحی که امکان رشد و نمو ریشه را فراهم کند، استفاده می‌شود. عملیات زیرشکنی با عمق متغیر به‌طوری‌که خواص فیزیکی خاک را تنها در مواردی که خاک‌ورزی برای رشد محصول مورد نیاز است اصلاح می‌کند، پتانسیل کاهش نیروی کار، هزینه‌ها، سوخت و انرژی مورد نیاز را دارد. از آنجایی که این مطالعه با هدف انجام عملیات زیرشکنی با عمق متغیر انجام شد، ابزار خاک‌ورزی با عمق متغیر (VDT) طراحی و ساخته شد. یک حسگر پنوماتیکی مجهز به چند نازل برای پیش‌بینی هم‌زمان عمق لایه متراکم خاک در سه عمق (۱۵، ۳۰ و ۴۵ سانتی‌متر) و ارسال سیگنال برای کنترل عمق خاک‌ورز VDT استفاده شده است. ارزیابی سامانه ابزار VDT به دو روش استاتیکی و دینامیکی انجام شد. در ارزیابی استاتیکی، زمان پاسخ سیستم برای رسیدن به ۹۵ درصد عمق‌های موردنظر اندازه‌گیری شد. ارزیابی دینامیکی زیرشکن نیز در دو مرحله انجام شد. میزان مصرف سوخت و مسافت رسیدن تیغه‌های زیرشکن به عمق موردنظر در سه تکرار اندازه‌گیری شد و با دستگاه زیرشکن (در حالت کنترل عمق خاموش) مقایسه گردید. میانگین مصرف سوخت در حالت عمق متغیر نسبت به عمق بیشینه ثابت به میزان ۱۷/۳۶ درصد کاهش پیدا کرد. همچنین سنجنده به‌خوبی وارد خاک شده و فرمان کنترل را به سیلندر هیدرولیکی به‌طور پیوسته ارسال می‌کرد و دستگاه زیرشکن، خاک را در عمق‌های ارسالی از سوی سنجنده زیرشکنی نمود.

واژه‌های کلیدی: خاک‌ورزی دقیق، خاک‌ورز عمق متغیر (VDT)، حسگر پنوماتیکی، کاهش مصرف سوخت، لایه خاک متراکم

۱- بخش تحقیقات فنی و مهندسی کشاورزی، مرکز تحقیقات و آموزش کشاورزی و منابع طبیعی استان مرکزی، سازمان تحقیقات، آموزش و ترویج کشاورزی، اراک، ایران
۲- دانشکده مهندسی مکانیک، دانشگاه صنعتی اراک، اراک، ایران
۳- موسسه تحقیقات فنی و مهندسی کشاورزی، سازمان تحقیقات، آموزش و ترویج کشاورزی، کرج، ایران
(*- نویسنده مسئول: Email: tahmasebi.mona@gmail.com)

https://doi.org/10.22067/jam.2023.79231.1128

مندرجات

مقالات پژوهشی

نشریه ماشین های کشاورزی

با شماره پروانه ۸۹/۱۲۶۳۹ **و درجه علمی – پژوهشی شماره** ۳/۱۱/۳۷۸۱ **از وزارت علوم، تحقیقات و فناوری**

۸۹/۶/۱۳ **۸۹/۳/۱۷**

"بر اساس مصوبه وزارت عتف از سال ۱۳۹۸، کلیه نشریات دارای درجه "علمی-پژوهشی" به نشریه "علمی" تغییر نام یافتند."

جلد ۱۳ شماره ۱ بهار ۱۴۰۲

صاحب امتیاز: دانشگاه فردوسی مشهد

مدیر مسئول: سید محمدرضا مدرس رضوی — استاد- گروه مکانیک دانشکده مهندسی (دانشگاه فردوسی مشهد)

سردبیر: محمدحسین عباسپور فرد — استاد- گروه مهندسی مکانیک بیوسیستم (دانشگاه فردوسی مشهد)

ناشر: دانشگاه فردوسی مشهد

مقالات این نشریه در پایگاه‌های زیر نمایه می‌شود:

AGRIS، CABI، DOAJ، EBSCO، Google scholar، پایگاه استنادی جهان اسلام (ISC)**، سامانه نشریات علمی، پایگاه اطلاعات علمی جهاد دانشگاهی** (SID)**، بانک اطلاعات نشریات کشور** (MAGIRAN)**، مرجع دانش** (CIVILICA)

پست الکترونیک: jame@um.ac.ir

مقالات این شماره در سایت http://jame.um.ac.ir **به‌صورت مقاله کامل نمایه شده است.**

این نشریه به تعداد ۴ شماره در سال و به‌صورت آنلاین منتشر می‌شود.

انجمن مهندسان مکانیک ایران

نشریه علمی
ماشین های کشاورزی

دانشگاه فردوسی مشهد

جلد۱۳ شماره ۱
سال ۱۴۰۲
(شماره پیاپی: ۲۷)

شاپا: ۶۸۲۹-۲۲۲۸

عنوان مقالات